การพัฒนาเทคนิคโฟกัสลำอนุภาคไอออนโดยใช้หลอดคาปิลารีเรียว และการประยุกต์ใช้ในการวิเคราะห์ด้วยไมโครพิกซี

นายศราวุธ ใจเย็น

วิทยานิพนธ์นี้เป็นส่วนหนึ่งของการศึกษาตามหลักสูตรปริญญาวิศวกรรมศาสตรดุษฎีบัณฑิต
สาขาวิชาวิศวกรรมนิวเคลียร์ ภาควิชาวิศวกรรมนิวเคลียร์
คณะวิศวกรรมศาสตร์ จุฬาลงกรณ์มหาวิทยาลัย
ปีการศึกษา 2554

DEVELOPMENT OF ION BEAM FOCUSING TECHNIQUE USING TAPERED CAPILLARY AND ITS APPLICATION TO MICRO-PIXE ANALYSIS

Mr. Sarawut Jaiyen

A Dissertation Submitted in Partial Fulfillment of the Requirements
for the Degree of Doctor of Engineering Program in Nuclear Engineering
Department of Nuclear Engineering
Faculty of Engineering
Chulalongkorn University
Academic Year 2011

Thesis Title	DEVELOPMENT OF ION BEAM FOCUSING TECHNIQUE USING TAPERED CAPILLARY AND ITS APPLICATION TO MICRO-PIXE ANALYSIS
By	Mr. Sarawut Jaiyen
Field of Study	Nuclear Engineering
Thesis Advisor	Associate Professor Nares Chankow
Thesis Co-advisor	Professor Yoshiyuki Oguri, D.Eng.
	Associate Professor Jun Hasegawa, D.Sc.

Accepted by the Faculty of Engineering, Chulalongkorn University in Partial Fulfillment of the Requirements for the Doctoral Degree

……..… Dean of the Faculty of Engineering
(Associate Professor Boonsom Lerdhirunwong, Dr.Ing.)

THESIS COMMITTEE

…….. Chairman
(Associate Professor Supitcha Chanyotha, Ph.D.)

…….……. Thesis Advisor
(Associate Professor Nares Chankow)

…….. Thesis Co-advisor
(Professor Yoshiyuki Oguri, D.Eng.)

…….. Thesis Co-advisor
(Associate Professor Jun Hasegawa, D.Sc.)

…….. Examiner
(Associate Professor Sunchai Nilsuwankosit, Ph.D.)

…….. Examiner
(Phongphaeth Pengvanich, Ph.D.)

…….. External Examiner
(Sirichai Wangchareontrakul, Ph.D.)

ศราวุธ ใจเย็น : การพัฒนาเทคนิคโฟกัสลำอนุภาคไอออนโดยใช้หลอดคาปิลารีเรียวและการประยุกต์ใช้ในการวิเคราะห์ด้วยไมโครพิกซี. (DEVELOPMENT OF ION BEAM FOCUSING TECHNIQUE USING TAPERED CAPILLARY AND ITS APPLICATION TO MICRO-PIXE ANALYSIS) อ. ที่ปรึกษาวิทยานิพนธ์หลัก : รศ. นเรศร์ จันทน์ขาว, อ. ที่ปรึกษาวิทยานิพนธ์ร่วม : ศ. ดร. โยชิยูกิ โอกูริ, รศ. ดร. จุน ฮาเซกาวา, 92 หน้า.

เทคนิคการสร้างหลอดคาปิลารีเรียวให้มีรูปแบบของปลายเรียวที่แตกต่างกันได้ถูกพัฒนาขึ้นและทดสอบความสามารถการโฟกัสลำอนุภาคไอออนพลังงานระดับเมกะอิเล็กตรอนโวลต์ และได้ตรวจสอบความสัมพันธ์ระหว่างวัสดุที่ใช้ทำหลอดคาปิลารีกับความสามารถในการโฟกัสโปรตอน โดยเปรียบเทียบระหว่างหลอดคาปิลารีที่ทำมาจากแก้วโบโรซิลิเกตกับแก้วตะกั่ว จากการวัดสเปกตรัมพลังงานของโปรตอนที่โฟกัสโดยหลอดคาปิลารีเรียวพบว่าค่าอัตราส่วนการโฟกัสของแก้วตะกั่วมีค่ามากกว่าแก้วโบโรซิลิเกตเพียงเล็กน้อยแต่ค่าอัตราส่วนการโฟกัสนี้มีค่าน้อยมากเมื่อเทียบกับค่าที่ได้จากการคาดการจากค่าภาคตัดขวางการกระเจิงของรัตเทอร์ฟอร์ด ได้ทำการหาผลกระทบของรูปแบบปลายเรียวของหลอดคาปิลารีและวัสดุที่ใช้ทำหลอดคาปิลารีต่อความสามารถในการส่งผ่านของลำอนุภาคโดยใช้การจำลองแบบมอนติคาร์โล 3 มิติ พบว่าเมื่อใช้หลอดคาปิลารีที่มีลักษณะมุมเอียงคงที่ ค่าอัตราส่วนการโฟกัสเพิ่มขึ้นเป็นสองเท่าเมื่อเทียบกับหลอดคาปิลารีที่มีลักษณะปลายเรียว ผลการจำลองนี้ชี้ให้เห็นว่าโอกาสที่โปรตอนหลุดออกจากผนังของหลอดคาปิลารีหลังจากการกระเจิงมีอิทธิพลต่อการส่งผ่านของไอออนพลังงานระดับเมกะอิเล็กตรอนโวลต์ ได้ทำการหาผลกระทบของความหยาบของผิวของผนังคาปิลารีต่อการส่งผ่านลำอนุภาคโดยใช้แผ่นแก้วที่มีความหยาบของพื้นผิวที่แตกต่างกัน ได้พัฒนาเทคนิคใหม่สำหรับการสุ่มวัดลำอนุภาคโดยการใช้อุปกรณ์ตัดลำอนุภาคเพื่อใช้ในการปรับค่าของโปรตอนที่วัดได้เทียบกับฟลักซ์ของโปรตอนตอนเริ่มต้น จากสเปกตรัมพลังงานของโปรตอนที่กระเจิงจากแผ่นแก้วที่มีความหยาบแตกต่างกันพบว่าความหยาบของพื้นผิวจะลดโอกาสในการกระเจิงของโปรตอน ได้ทำการหาส่วนประกอบของธาตุในชั้นผิวของชามสังคโลกทั้งชนิดโบราณและที่ผลิตขึ้นมาใหม่โดยวิเคราะห์ด้วยเทคนิคไมโครพิกซีที่ใช้หลอดคาปิลารีในการโฟกัสลำอนุภาค สามารถหาการกระจายตัวของธาตุของชั้นผิวเคลือบและชั้นสีได้อย่างชัดเจนโดยการสแกนภาคตัดขวางของชามสังคโลกด้วยลำอนุภาคขนาด 70 ไมครอน ซึ่งสามารถแยกแยะความแตกต่างของธาตุที่ชั้นผิวระหว่างชามสังคโลกโบราณและชามสังคโลกที่ผลิตขึ้นมาใหม่ ได้แสดงภาพสองมิติของการกระจายตัวของธาตุในภาคตัดขวางของชามสังคโลกโบราณเพื่อพิสูจน์ประสิทธิภาพของเทคนิคไมโครพิกซีโดยการใช้หลอดคาปิลารีเรียวโฟกัสลำอนุภาค

ภาควิชา วิศวกรรมนิวเคลียร์ ลายมือชื่อนิสิต .....

สาขาวิชา วิศวกรรมนิวเคลียร์ ลายมือชื่อ อ. ที่ปรึกษาวิทยานิพนธ์หลัก .....

ปีการศึกษา 2554 ลายมือชื่อ อ. ที่ปรึกษาวิทยานิพนธ์ร่วม .....

ลายมือชื่อ อ. ที่ปรึกษาวิทยานิพนธ์ร่วม .....

5171830721 : MAJOR NUCLEAR ENGINEERING
KEYWORDS : IONBEAM FOCUSING / GLASS CAPILLARY OPTIC / MONTE CARLO SIMULATION / PROTON SCATTERING / SURFACE ROUGHNESS / MICRO-PIXE / ARCHAEOLOGICAL OBJECTS

SARAWUT JAIYEN: DEVELOPMENT OF ION BEAM FOCUSING TECHNUQUE USING TAPERED CAPILLARY AND ITS APPLICATION TO MICRO-PIXE ANALYSIS. ADVISOR : ASSOC. PROF. NARES CHANKOW, CO-ADVISOR : PROF. YOSHIYUKI OGURI, D.Eng., ASSOC. PROF. JUN HASEGAWA, D.Sc., 92 pp.

A technique to fabricate tapered glass capillary optics with various taper shapes has been developed and MeV ion focusing was tested with this novel focusing optics. The dependence of the MeV ion focusing ability of the tapered capillary optics on the capillary wall material was investigated by comparing tapered capillaries made of borosilicate glass and lead glass. The energy spectrum from the capillary-focused proton beams showed that the beam focusing ratio for the lead glass capillary was slightly higher than that for the borosilicate glass capillary, but the enhancement was much smaller than expected from the target atomic number dependence of the Rutherford scattering cross section. Three-dimensional Monte Carlo simulations were performed to examine the effect of the capillary wall shape as well as that of the wall material on the beam transmission. When a constant taper angle capillary was used, the beam-focusing ratio was improved by a factor of 2 compared to when the conventional tapered capillary having a convex inner wall was used. These results indicated that the probability of the scattered ion escaping from the capillary wall plays a predominant role in the MeV ion transmission in the tapered capillary optics. The effect of inner wall surface roughness on the beam transmission was also investigated by examining the energy spectra of protons forward scattered by flat glass targets having different surface roughness. A novel beam-sampling system using a rotating beam chopper has been developed and used to normalize the measured count of the scattered proton with respect to the incident proton flux. The energy spectrum of the scattered protons showed that the surface roughness might reduce the probability of proton scattering by the glass target. Finally, the elemental compositions in the surface layer of old and modern Sangkhalok potteries were investigated by the glass-capillary-based micro-PIXE analysis. By scanning the cross section of the piece of the pottery with a ϕ70-μm microbeam, the elemental distributions in the glaze and the paint layers were separately determined and clearly showed the differences in the surface layer between the old and the modern potteries. The two-dimensional mapping of elements was successfully demonstrated for the old Sangkhalok sample and its effectiveness was proved.

Department : Nuclear Engineering Student's Signature .....
Field of Study : Nuclear Engineering Advisor's Signature .....
Academic Year : 2011 Co-advisor's Signature .....
Co-advisor's Signature .....

Acknowledgements

The author would like to express his deepest gratitude to Associate Professor Nares Chankow, for his kind academic guidance, support and warm encouragement throughout the entire period of doctoral dissertation studies.

Earnest gratefulness is also attributed to co-advisors Associate Professor Dr. Jun Hasegawa and Professor Dr. Yoshiyuki Oguri of Tokyo Institute of Technology, for their understanding, expert suggestions and sincere support throughout the study period.

The author also would like to extend his appreciation to Mr. Hitoshi Fukuda and Mr. Masatoshi Shikida for providing assistance in the preparation of the experimental apparatus. Sincere thanks are also due to Dr. Sirichai Wangchareontrakul for his guidance of archaeological sciences and providing Sangkhalok sample.

The author would like to convey his appreciation to Prof. Dr. Toyohiko Yano for giving permission to use the facility in his laboratory. Sincere thanks are also offered to Mr. Noppasint Jiraborvornpongsa and Mr. Atsawin Salee for his technical support in taking SEM photographs.

I am thankful to the Office of the Higher Education Commission for their grant support under the program CHE Ph.D. Scholarships and the Japanese Government (MEXT) Scholarship program for which I could visit Japan to pursue my higher studies. My special thanks are also offered to the Nuclear Safety Research Association (NSRA) for their support.

Many thanks are distributed to members of OGRI Laboratory (former and current students), Dr. Tsutomu Tada, Dr. Sureerat Thomyasirigul, Dr. Sarinrat Wonglee, Mr. Yukihiro Aoyama, Mr. Takao Moriyama, Mr. Hu Yuchao and Ms. Kamoltip Ploykrachang, for their support and friendly attitude throughout the study.

A special thanks goes to Ms. Noppawan Thipcharoensuk for her great encouragement and support.

Finally, I would like to say that without the invaluable moral support, patient understanding, encouragement and continuous co-operations from my father, Mr. Sukam Jaiyen, my mother Mrs. Kumaree Jaiyen, my elder sister Mrs. Supaporn Tachaiwong, and all close relatives, this piece of research work would never have been completed.

Contents

Page

Abstract (Thai)..... iv

Abstract (English)..... v

Acknowledgements..... vi

Contents..... vii

List of tables..... xi

List of figures..... xii

Chapter

I INTRODUCTION……..……..…… 1

1.1 Background and problems of interest……..…..…… 1

1.2 Objectives……..……...……...… 3

1.3 Scope and limitation of the study…… 3

1.4 Benefits…… 3

1.5 Research methodology…… 4

II THEORY AND LITERATURE REVIEW……...… 5

2.1 Ion beam focusing using a capillary…… 5

2.2 Kinematic factor…….. 7

2.3 Scattering cross section……... 9

2.4 Existing application of the microbeam using a capillary…… 11

2.5 Monte-Carlo Simulation……..… 13

2.6 PIXE analysis……..… 16

2.6.1 Introduction to PIXE……. 16

2.6.2 PIXE analysis of archaeological samples…….…… 18

2.7 Sangkhalok pottery……..… 19

III EXPERIMENTAL…… 20

3.1 Tandem accelerator system and beam-line components……. 20

3.1.1 Tandem electrostatic accelerator……... 20

3.1.2 Ion sources…… 21

3.1.3 Beam-line components…….. 22

Chapter Page

3.2 Detector and measurement system…….. 25
3.2.1 X-ray detector…… 25
3.2.2 Charged-particle detector…….. 25
3.2.3 Preamplifier and Amplifier……... 25
3.2.4 Multichannel Analyzer…….. 26
3.3 Tapered glass capillary…… 26
3.3.1 Fabrication of tapered glass capillaries……. 26
3.3.2 Determination of axial profiles and checking of the axial symmetry of the capillary……. 27
3.4 Investigation the transport mechanism of MeV protons……. 29
3.4.1 Beam-experiment configuration and alignment method of the capillary…….. 29
3.4.2 Measurement of energy spectra of focused protons beams.. 30
3.4.3 Numerical simulations using a Monte Carlo code…… 30
3.5 Glancing-angle-scattering experiments using flat glass targets …. 31
3.5.1 Flat glass targets…… 31
3.5.2 Experimental apparatus……. 33
3.5.3 Normalization of the incident protons……... 34
3.6 Micro-PIXE experiments using a capillary-focused microbeam ... 36
3.6.1 Investigation of the performance of micro-PIXE system…. 36
3.6.2 Archaeological sample……. 37
3.6.3 Preliminary investigation of elemental composition and X-ray from glass tube…… 39
3.6.4 Experimental setup for archaeological sample using tapered glass capillary…….. 41

Chapter Page

IV RESULTS AND DISCUSSION…… 43

4.1 Shape and axial symmetry of the tapered glass capillary…… 43

4.2 Transport mechanism of MeV proton……. 46

4.2.1 Beam spot patterns recorded on imaging plates…… 46

4.2.2 Energy spectra of focused proton beams…….. 47

4.2.3 Intensity distributions of focused proton beams……... 49

4.2.4 The MC simulation results of protons focused by tapered capillary and conical capillary…….…. 50

4.2.5 The dependences of the focusing ratio on the atomic number of capillary wall……..…….. 52

4.3 Glancing-angle-scattering of MeV protons by flat glass having different surface roughnesses …… 54

4.3.1 Normalization of scattered proton count…….…….. 54

4.3.2 Effect of surface roughness on the beam transport……..….. 58

4.4 micro-PIXE analysis of archaeological sample ……..…… 64

4.4.1 Performance of the micro-PIXE system……..….. 64

4.4.2 Elemental composition of the archaeological sample measured using a 500-μm-diameter beam……..…….. 65

4.4.3 PIXE analysis of glass tubes……..…… 68

4.4.4 micro-PIXE spectrum of the old Sangkhalok…….…….. 70

4.4.5 Depth profile of the elemental distribution on cross section of the old Sangkhalok…….…….. 71

4.4.6 Two-dimensional element distribution of the old Sangkhalok…… 74

4.4.7 Comparison between the old and present pottery..... 78

4.4.8 X-ray spectra of the potteries irradiated by proton and electron beam..... 80

Chapter Page

V SUMMARY AND CONCLUSIONS..... 83

5.1 Conclusions..... 83

5.2 Suggestion and future studies..... 87

5.3 List of publications..... 87

5.4 List of presentations..... 88

References..... 89

Biography..... 92

List of Tables

		Page
Table 3.1	Specifications of glass tubes used in this study.....	27
Table 3.2	Specifications of flat glass targets.....	31
Table 4.1	Effective atomic number and beam-focusing ratio of the capillary glass.....	48
Table 4.2	MC simulation result of beam-focusing ratio.....	51

List of Figures

		Page
Figure 2.1	Beam guiding by self-organized charge up of insulator wall.....	6
Figure 2.2	Schematic representation of an elastic collision between a projectile and a target…….	8
Figure 2.3	Characteristic X-ray productions in PIXE (case of K_α emissions).....	16
Figure 3.1	Schematic of the tandem accelerator and the beam lines.....	21
Figure 3.2	Quadrupole magnet with magnetic field lines and the directions of force on the beam.....	24
Figure 3.3	(a) puller (PE-21, Narishige Co., Ltd.), (b) micro-forge device (MF-900, Narishige Co., Ltd.). (c) A straight glass tube clamped on the puller.....	27
Figure 3.4	(a) Long-working-distance optical microscope connected to a CCD camera. (b) Schematic view and (c) a picture of the device for capillary wall profile measurement.....	28
Figure 3.5	Schematic of the experimental setup.....	29
Figure 3.6	Flat glass plates used in this study, which have different levels of surface roughness.....	31
Figure 3.7	Holder for flat glass targets and a polycrystalline ruby plate.....	32
Figure 3.8	Experimental setup for the glancing-angle-scattering experiment.....	33
Figure 3.9	Schematic of the gold rotational-plate system.....	34
Figure 3.10	(a) A piece of broken old Sangkhalok and (b) an image on cross section taken by optical microscope.....	37
Figure 3.11	(a) A modern Sangkhalok and (b) an image on cross section taken by optical microscope.....	38
Figure 3.12	Holder of old Sangkhalok sample.....	39
Figure 3.13	Experimental setup for micro-PIXE analysis using two apertures.....	39
Figure 3.14	Tapered glass capillary used in micro-PIXE analysis for archaeological sample.....	40
Figure 3.15	The experimental setup for micro-PIXE analysis using tapered glass capillary.....	41
Figure 4.1	A complete view of tapered glass capillaries made of borosilicate glass (upper) and lead glass (lower).....	43
Figure 4.2	SEM images of the capillary outlet of (a) borosilicate-glass and (b) lead-glass capillaries.....	44
Figure 4.3	Photograph of whole tapered (a) borosilicate-glass and (b) lead-glass capillary.....	44

Figure 4.4 Axial profiles of the inner diameter for borosilicate-glass and lead-glass capillaries..... 45
Page
Figure 4.5 Comparisons of axial profiles of the inner diameter observed at 0° and 90° for (a) borosilicate-glass and (b) lead-glass capillaries..... 45
Figure 4.6 Beam spot patterns recorded on imaging plates when the tapered capillary (lead glass) was (a) misaligned and (b) well aligned with respect to the incident beam axis. Imaging plates were located 65 cm downstream from the capillary tip..... 46
Figure 4.7 Energy spectra of protons focused by (a) borosilicate-glass capillary and (b) lead-glass capillary. The gray solid and dashed lines in Fig. a show the core component and the proton incident energy, respectively..... 47
Figure 4.8 Intensity distributions of the proton beams focused by borosilicate-glass and lead-glass capillaries. Beam intensities were evaluated along the dashed line in the beam spot image..... 49
Figure 4.9 Trajectories of protons focused by (a) a tapered capillary and (b) a conical capillary, and two-dimensional angular distribution of the protons on the detector of (c) a tapered capillary and (d) a conical capillary..... 50
Figure 4.10 Dependences of the focusing ratio on the atomic number of capillary wall materials calculated for a tapered and a conical capillary..... 52
Figure 4.11 Schematic of the escape distance for the tapered capillary (*a*) and the conical capillary (*b*)..... 53
Figure 4.12 X-ray spectrum of flat glass target..... 54
Figure 4.13 Dependence of potassium K X-ray intensities from of flat glass targets on target angle..... 55
Figure 4.14 Spectra of scattered proton from a rotating beam chopper at (a) 4% and (b) 25% of the incident beam was chopped..... 56
Figure 4.15 Comparison of energy spectra of forward-scattered protons measured with and without beam chopping..... 57
Figure 4.16 Schematic shows the definition of the angle..... 58
Figure 4.17 Energy spectra of protons scattered by flat glass #1 with target angles of (a) 1º, (b) 2º, and (c) 3º..... 60
Figure 4.18 Energy spectra of protons scattered by flat glass #2 with target angles of (a) 1º, (b) 2º, and (c) 3º..... 61
Figure 4.19 Comparison of energy spectra between protons scattered by flat glass target #1 and those by flat glass target #2. Target angles are (a) 1º, (b) 2º, and (d) 3º. Takeoff angle is fixed to be 0.5º..... 62

Page

Figure 4.20	Comparison the energy spectra of protons scattered by target #1 and those by target #2 with scattering angles of (a) 1.5º, (b) 2º, and (c) 3º. Target angle is fixed to be 1º.....	63
Figure 4.21	A typical X-ray spectrum measured for a copper plate target.....	64
Figure 4.22	A Cu-K X-ray intensity profile measured at the edge of the copper plate.....	64
Figure 4.23	A magnified photograph of copper fine mesh and a copper distribution reconstructed from the Cu-K X-ray intensities.....	65
Figure 4.24	PIXE spectrum of the stainless steel sample for calibration.....	66
Figure 4.25	PIXE spectrum of (a) the surface and (b) the substrate of the old Sangkhalok irradiated by 500-μm-diameter beam.....	67
Figure 4.26	PIXE spectra of (a) borosilicate glass (Narishige Co., Ltd.), (b) borosilicate glass (7056 Patch glass), and (c) lead glass (8161 Patch glass).....	66
Figure 4.27	PIXE spectra from the cross section of the old Sangkhalok at glaze, brown paint, and substrate.....	70
Figure 4.28	Beam positions on the cross section of the old Sangkhalok. Circles indicate the beam sizes.....	70
Figure 4.29	The scanning direction on the cross section of the old Sangkhalok.....	71
Figure 4.30	PIXE spectra of the old Sangkhalok at (a) the brown part and (b) the transparent part.....	72
Figure 4.31	Intensity distributions of elements as a function of depth on the cross section of (a) the brown part and (b) the transparent part of the old Sangkhalok.....	73
Figure 4.32	Two-dimensional element distributions of (a) Ca, (b) Fe, (c) K, (d) Mn, (e) Ti, and (f) Si on the cross section of the old Sangkhalok.....	75
Figure 4.33	Cross sectional photograph of the modern Sangkhalok with position where PIXE spectra were measured.....	78
Figure 4.34	PIXE spectra on the cross section of the modern Sangkhalok.....	78
Figure 4.35	The intensity distribution of Cr as a function of depth on the cross section of the modern Sangkhalok.....	79
Figure 4.36	X-ray spectra on the cross section of the modern Sangkhalok measured with (a) 2 MeV proton and (b) 15 keV electron microprobe.....	80
Figure 4.37	Minor elements found on the cross section of the modern Sangkhalok.....	81

Chapter I
INTRODUCTION

1.1 Background and problems of interest

Recently tapered glass capillaries have been attracting much attention as a tool to guide and focus energetic ions with MeV energies. This novel beam focusing optics uses the elastic scattering of incident ions by atomic nuclei, which is one of the major interaction processes between energetic ions and solid surfaces. A projectile ion approaching a nucleus in the wall of the glass capillary undergoes conventional Coulomb or Rutherford scattering. Then, the projectile loses its kinetic energy and changes the direction of motion. In most scattering events, however, the scattering angle and the corresponding energy loss are very small because the scattering cross section is inversely proportional to the fourth power of one-half the scattering angle. Based on the idea that such glancing-angle scattering may be useful for ion beam focusing, Nebiki *et al.* [1] demonstrated for the first time the focusing of 2 MeV helium ions with tapered glass capillaries having outlet diameter of less than 1 μm. They successfully observed a beam focusing effect of the tapered glass capillaries and applied this new technique to in-air-PIXE analysis [2]. Because the microbeam irradiation device based on this technique is compact and inexpensive compared to the conventional devices using a combination of a collimator and quadrupole magnets, this technique has been used for various applications such as nuclear reaction analysis [3], high-contrast X-ray imaging [4], cell surgery [5], micro-PIXE analysis [2, 6], in-air RBS [7], and in-air STIM [8].

An index of the ion focusing ability of the tapered capillary optics is the beam-focusing ratio, which is defined as the ratio of the averaged beam current density measured at the capillary outlet to that measured at the inlet. Because the beam heat load on the capillary glass wall limits the allowable incident beam current, the improvement of the beam-focusing ratio has been one of the crucial issues to be considered while developing application of the tapered capillary optics. The strong dependence of the Rutherford scattering cross section on the target atomic number ($\sim Z^2$) indicates that the beam-focusing ratio might be improved by using capillaries made of material with higher atomic number. In addition, because the scattering cross

section is very sensitive to the scattering angle, the focusing ratio might be improved also by optimizing the shape of the capillary inner wall [9]. Moreover, the surface roughness of capillary inner wall might affect the transport efficiency of the scattered ions. Thus, it is crucial to examine the effects of the capillary wall properties, such as material, shape, and surface roughness, on the beam-focusing ability of the tapered capillary optics.

The particle-induced X-ray emission (PIXE) is a well known technique for material analysis using a few MeV ion beam [10]. Its sensitivity is quite high and multiple elements in a sample can be analyzed simultaneously. Furthermore, only several tens of microgram is enough to analyze elements in a sample. The interest in PIXE technique has been recently growing because it can be applied to studies in a wide range of fields such as biology [11, 12], art and archeology [13, 14, 15].

The purpose of this study is to elucidate the effects of the capillary wall material and shape on the beam-focusing ability of the tapered capillary and the effects of the surface roughness of the capillary inner wall on the transport efficiency of the scattered ions. Moreover, this research aims to reveal the elemental compositions of the glaze and the paint layers of typical Sangkhalok potteries by micro-PIXE analysis based on a glass-capillary-focused proton microprobe.

The old Thai pottery called “Sangkhalok” was produced during the 13^{th} to 16^{th} centuries at the ancient capital of the first Thai kingdom and exported far and wide to various countries. The feature of Sangkhalok is painting patterns with brown color on white foundation and transparent surface coating. Some of old Sangkhalok have damages on the glaze and paint layer because of aging degradation. To repair the glaze and paint layer of the damaged potteries, we need to use the glaze and paint material having the same elemental composition as those used for the old potteries. PIXE can be a powerful tool of elemental analysis of valuable cultural heritages including old Sangkhalok potteries because of its non-destructive, high-sensitivity features. Because the thicknesses of the glaze and the paint layers are only several hundreds of micrometer, the size of the ion beam for the PIXE analysis must be as small as some 100 μm to separately examine the elemental distributions of those layers in detail.

1.2 Objectives

The goals of this research are:

1.2.1 To investigate the transport mechanism of MeV ions through tapered glass capillaries under various beam parameters and capillary wall materials.

1.2.2 To demonstrate the feasibility of the tapered glass capillary used as a compact beam-focusing device for micro-PIXE analysis of archeological samples.

1.3 Scope and limitation of the study

1.3.1 Establish the fabrication technique of tapered glass capillaries with different wall materials, evaluate the profile of the inner diameter versus the axial position, and check the axial symmetry of capillary shape.

1.3.2 Examine the properties of micro-beams from the tapered capillary by measuring beam intensity profiles and energy spectra of focused ions.

1.3.3 Reveal the dependencies of the micro-beam properties on the capillary parameters such as wall material and the surface roughness of the inner wall.

1.3.4 Investigate in detail the beam transport mechanism in the tapered capillary by Monte-Carlo simulations under various beam parameters and capillary conditions.

1.3.5 Demonstrate micro-PIXE analysis for non-destructive elemental analysis and mapping of archaeological samples.

1.4 Benefits

1.4.1 Understand the physical phenomena related to the beam focusing and physical parameters that can be used to increase the focusing factor of tapered capillary optics.

1.4.2 The new technique of micro-PIXE can be used for non-destructive analysis of precious cultural assets in Thailand.

1.5 Research methodology

1.5.1 Develop the technique to fabricate the tapered glass capillaries with various materials and shapes.

1.5.2 Design and construct the device that can check the axial symmetry of capillary shape.

1.5.3 Measure the profile of the inner diameter versus the axial position and check the axial symmetry of capillary shape.

1.5.4 Perform beam experiments using tapered glass capillaries with different wall material for measuring the beam intensity profile and energy spectra of focused ions.

1.5.5 Develop the experimental apparatus to perform glancing-angle-scattering experiments using flat glass targets.

1.5.6 Examine the effect of wall surface roughness on beam transport by using flat glass targets having various surface roughnesses.

1.5.7 Demonstrate elemental mapping of an archaeological sample using a capillary-focused microbeam.

Chapter II
THEORY AND LITERATURE REVIEW

Chapter II describes theory and literature review related to ion beam focusing using an insulator capillary, kinematic factor, scattering cross section, application studies of the capillary-focused microbeams, Monte Carlo simulation of ion scattering process in the capillary, PIXE analysis. A brief introduction of the Sangkhalok pottery is also given.

2.1 Ion beam focusing using a capillary

In conventional ion microbeam system, an ion beam from the accelerator is collimated by small slits and then focused on the target by quadrupole magnetic lenses to achieve a beam spot size of several micrometers or less [16]. From the viewpoint of beam optics, this scheme is based on the reduced projection of the image of the collimator on the target plane, where the reduction factor is typically around 10. Since the required length of the beam focusing section is determined by the focal length of the quadrupole magnets and the reduction factor, the total length of the conventional microbeam system is usually several meters or more.

Recently, the ion beam guiding effect of insulator capillaries have been reported by many scientists. Hellhammer *et al*. [17] demonstrated the guiding of 1-10 keV Ne^{7+} by 100-nm-diameter capillaries formed on a film of polyethylene terephthalate (PET). Ikeda *et al*. [18] applied a tapered glass capillary to the guiding of slow highly charged ions, such as 8-keV Ar^{8+}. They reported a beam transmission of 1% through a capillary of 5 cm long and 800/24 μm inlet/outlet diameter. Since the transmitted beam had the same size as the capillary outlet, the tapered glass capillary was found to work as a beam-focusing optics with a typical beam focusing ratios of approximately 10. Surprisingly, the incident beam was guided through a capillary tilted by as large as ±100 mrad and it still kept the incident charge even after the extraction from the capillary. Nebiki *et al*. [1] presented an evidence of the focusing effect of the tapered glass capillary optics for MeV He ion beams. Although the majority of incident ions were lost in the capillary, a part of them, actually about 1% more or less, was found to exit through the outlet without significant energy loss. This

novel focusing method using a tapered capillary has the potential to drastically reduce the size and cost of the microbeam irradiation system compared with the conventional ones.

The beam guiding and focusing effects of the insulator capillaries have been considered to be achieved by different physical mechanisms depending on the incident beam energies. In keV energy range, the self-organized charge-up of the insulator inner wall surface provides the beam-guiding effect as shown in Fig. 2.1 [18]. An ion beam enters a tapered glass capillary from the left side and exits from the right side. When the surface of the capillary inner wall is uncharged, the ions arriving at point x on the wall will be stopped there and deposited their charge on it. The wall surface at this point is gradually charged up (Fig. 2.1a). When the electric field induced by the accumulated charge becomes large enough to prevent the following incident ions from reaching the inner wall, the ions slightly change their directions and travel more or less parallel to the wall (Fig. 2.1b). The reflection of the ions on the inner wall does not always require an exact angle between the beam axis and the surface. This means that transmission can take place even if the beam axis has an angle with respect to the capillary axis.

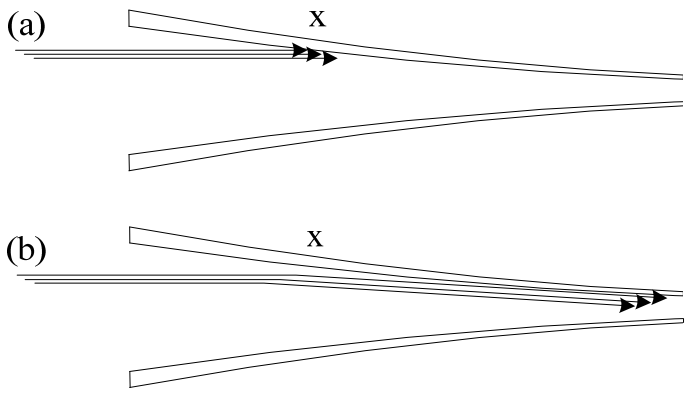

Fig. 2.1 Beam guiding by self-organized charge up of insulator wall

On the other hand, the guiding due to the self-organized charge-up becomes less effective in the MeV range because it is considered difficult to maintain an electrostatic field that is strong enough to bend trajectories of MeV ion without breakdown. Nebiki *et al*. [9] reported that when a 6.4 MeV $^{15}N^{2+}$ ions beam was

focused by a tapered glass capillary optics, the transmitted beam included ions that suffered slight energy losses. They also showed that the focusing ratios were independent on the incident beam current and the transmitted beam current decreased with increasing capillary taper angle. These results suggest that the nuclear forward scattering was more significant in the focusing of MeV ions. Gong *et al*. [19] presented experiment results on the focusing of 2-MeV He^+ beam. Ion beams were focused by tapered glass capillaries with various outlet inner diameters from several micrometers to hundred micrometers. They found that a great part of the transmitted ions experienced obvious energy loss, which implied that the deflection of the ions occurred not on the surface of the capillary inner wall but in the body of the capillary. To clarify the transport mechanism of MeV ions through the tapered capillary, more analyses particularly based on numerical simulations are needed.

In a previous paper, the beam focusing ratios were evaluated from the beam currents measured at the inlet and the outlet of the capillary by using the following formula:

$$\eta \equiv \frac{I_{\text{out}} / I_{\text{in}}}{\left(r_{\text{out}} / r_{\text{in}}\right)^2} = \frac{\bar{J}_{\text{out}}}{\bar{J}_{\text{in}}}. \tag{2.1}$$

Here, r is the capillary radius, I is the beam particle current, and J is the particle current density averaged over the beam cross section. The suffixes “in” and “out” denote values at the capillary inlet and outlet, respectively. Note that Eq. (2.1) fairly reflects the beam focusing ability of the tapered glass capillary only when the incident beam is parallel and uniform.

2.2 Kinematic factor

When a particle of mass M_1, moving with constant velocity, collides elastically with a stationary particle of mass M_2, energy will be transferred from the moving to the stationary particle. Mass M_1 is the projectile atom and mass M_2 is an atom in the target. The assumption that the interaction between the two atoms is properly described by a simple elastic collision of two isolated particles rests on two conditions. First, the projectile energy E_0 must be much larger than the binding energy of the atoms in the target. Chemical bonds are of the order of 10 eV, so that E_0 should

be very much larger than that. Second, nuclear reactions and resonances must be absent. This imposed an upper limit to the projectile energy. Nuclear processes depend on the specific choice of projectile and target atoms, so that the upper limit of E_0 varies with circumstances.

The simple elastic collision of two masses M_1 and M_2 can be solved fully by applying the principles of conservation of energy and momentum. Let v_0 and $E_0 = (1/2)M_1v_0^2$ be the velocity and the energy of a projectile atom of mass M_1 before the collision, while the target atom of mass M_2 is at rest. After the collision, let v_1 and v_2 be the velocities and $E_1 = (1/2)M_1v_1^2$ and $E_2 = (1/2)\mathrm{M_2v_2^2}$ be the energies of projectile and target atoms, respectively. The geometry of this scattering are given in Fig. 2.2, where the scattering angle θ and the recoil angle ϕ are defined as positive number with the arrows as shown. All quantities refer to a laboratory system of coordinates.

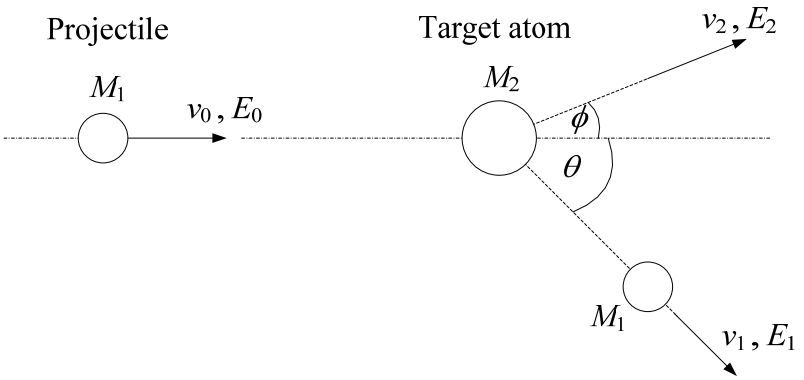

Fig. 2.2 Schematic representation of an elastic collision between a projectile and a target

Conservation of energy and conservation of momentum parallel and perpendicular to the direction of incidence and expressed by the equations

$$\frac{1}{2}M_1v_0^2 = \frac{1}{2}M_1v_1^2 + \frac{1}{2}M_2v_2^2, \tag{2.2}$$

$$M_1v_0 = M_1v_1\cos\theta + M_2v_2\cos\phi, \tag{2.3}$$

$$0 = M_1v_1\sin\theta - M_2v_2\sin\phi. \tag{2.4}$$

Eliminating ϕ first and then v_2, one finds

$$\frac{v_1}{v_0} = \frac{\pm\left(M_2^2 - M_1^2 \sin^2\theta\right)^{1/2} + M_1 \cos\theta}{M_2 + M_1}. \tag{2.5}$$

For $M_1 \leq M_2$ the plus sign holds. We now define the ratio of the projectile energy after the elastic collision to that before the collision as the *kinematic factor K*,

$$K \equiv \frac{E_1}{E_0}. \tag{2.6}$$

From Eq. (2.5) one obtains

$$K = \left[\frac{\left(M_2{}^2 - M_1{}^2 \sin^2\theta\right)^{1/2} + M_1 \cos\theta}{M_2 + M_1}\right]^2. \tag{2.7}$$

The kinematic factor depends only on the ratio of the projectile to the target masses and on the scattering angle θ [21].

2.3 Scattering cross section

The preceding section established the connection between the energy E_0 of the incident particle of mass M_1 and the energy KE_0 that this particle possesses at any angle θ after and elastic collision with an initially stationary mass M_2. How frequently such a collision actually occurs and ultimately results in a scattering event at a certain angle θ remains open. The differential scattering cross section $d\sigma/d\Omega$ is the concept introduced to answer this. Its definition is derived from a simple conceptual experiment. A narrow beam of fast particles impinges on a thin uniform target that is wider than the beam. At an angle θ from the direction of incidence, let an ideal detector count each particle scattered in the differential solid angle $d\Omega$. If Q is the total number of particles that have hit the target and dQ is the number of particles recorded by the detector, then the differential scattering cross section $d\sigma/d\Omega$ is defined as

$$d\sigma/d\Omega = (1/Nt)[(dQ/\, d\Omega)/Q)], \tag{2.8}$$

where N is the volume density of atoms in the target and t is its thickness. Thus Nt is the number of target atom per unit area (areal density). The definition implies that the solid angle $d\Omega$ is so small that the scattering angle θ is well defined. The definition also assumes that the thickness t is minimal and that, therefore, the energy loss of the particles is the target is so small that the energy of the particles is virtually the same at any depth in the target. Finally, the total number of incident particles Q must be so large that the ratio dQ/Q has a well-determined value.

To calculate the differential cross section for an elastic collision, the principles of conservation of energy and momentum must be complemented by a specific model for the force that acts during the collision between the projectile and the target masses. In most cases, this force is very well described by Coulomb repulsion of the two nuclei as long as the distance of closest approach is large compared with nuclear dimensions, but small compared with the Bohr radius $a_0 = \hbar/m_e e = 0.53$ Å. When these assumptions are made, the differential scattering cross section is given by Rutherfords's formula [21]:

$$\left(\frac{d\sigma}{d\Omega}\right)_c = \left[\frac{Z_1 Z_2 e^2}{4E_c \sin^2\left(\theta_c/2\right)}\right]^2, \tag{2.9}$$

where the subscript c indicates that the values are given with respect to the center-of-mass coordinates. Here Z_1 is the atomic number of the projectile atom with mass M_1, Z_2 is the atomic number of the target atom with mass M_2, e is the electronic charge and E is the energy of the projectile immediately before scattering. This formula is valid also for values in the laboratory frame of reference, but only when $M_1 \ll M_2$.

2.4 Existing application of the microbeam using a capillary

The microbeam irradiation device using the tapered glass capillary has been applied to various applications such as high-contrast X-ray imaging, cell surgery, nuclear reaction analysis, in-air RBS, in-air STEM, surface modification of polymer, and micro-PIXE analysis.

Hasegawa, *et al*. [4] constructed a compact micro-beam system using a tapered glass capillary with a tip diameter in the order of 10 μm to examine the applicability of capillary-generated micro-beams to high-contrast radiography based on proton-induced quasi-monochromatic X-rays. The transport efficiency of swift (2–3 MeV) protons through the capillary was examined as a function of the capillary tilt angle and the capillary tip diameter. The obtained transport efficiencies were approximately three times larger than would be expected from the geometrical shape of the capillary. This enhancement indicates that a focusing effect occurred in the capillary. A metallic thin foil was irradiated with the micro-beam and quasi-monochromatic X-rays were produced. By calculating the X-ray yields induced by proton bombardment in the foil and comparing them with the X-ray counts observed at the detector, the throughput efficiency of the X-ray imaging system was evaluated. They demonstrated magnification radiography of a small object to show that a spatial resolution on the order of 10 μm was achievable in their system.

Iwai, *et al*. [5] presented a cell surgery scheme involving selective inactivation or disruption of cellular structures. Energetic ions were injected into a cell through a tapered glass capillary like a microinjection method. A slight but essential difference from microinjection was that a thin window was prepared at the outlet so that no liquid material could flow in or back through the outlet while still allowing energetic ions to penetrate into the cell. An a few MeV He ion beam from such a capillary having 10 μm outlet diameter inactivated a selected volume (~μm^3) of fluorescent molecules located in a HeLa cell nucleus.

Sekiba, *et al*. [3] developed a micro-beam nuclear reaction analysis (NRA) system by means of a resonant nuclear reaction $^{1}H(^{15}N, \alpha\gamma)^{12}C$ for the purpose of the 3D mapping of the hydrogen distribution in solids. To obtain the tens μm size of the beam spot, the combination of the newly proposed tapered glass capillary and a conventional quadrupole magnetic lens was employed. An yttrium-patterned film including hydrogen on a substrate was prepared as a sample of application of the

developed system. A 6 MeV ^{15}N beam focused by a tapered glass capillary down to 50 μm successfully showed the hydrogen distribution. The in-plane NRA profile implied that the beam emitted from the glass capillary outlet was parallel, although the original beam had a considerable divergence. The NRA measurements in the 10^3 Pa N_2 atmosphere based on the low gas conductance of the glass capillary was also demonstrated.

Ishii, *et al*. [7] developed a simple Rutherford backscattering spectroscopic (RBS) method to analyze sample depth profiles in air. To avoid excessive energy loss of 3 MeV proton projectile ions in air, they used a metal capillary instead of a thin vacuum window. Using this capillary, they were able to extract a sufficiently large proton beam current to perform in-air RBS and in-air PIXE without requiring any window, such as a thin film, between the vacuum chamber and air. They have validated their technique by measuring of RBS spectra of Au foils of various thicknesses, 0.25, 0.75, and 2.5 μm. A comparison of the experimental results with a simple theoretical calculation indicated that this technique is useful for analyzing any specimen in air.

Simon, *et al*. [8] developed a nuclear microprobe based on a tapered glass micro-capillary. A MeV ion beam was collimated to a diameter of approximately 1 μm without ion optical lenses. Due to the small gas leakage through the capillary opening, the beam could be taken into air without any membrane or special differential pumping device. Samples were raster-scanned by means of a piezo-driven XY stage. For Scanning Transmission Ion Microscopy (STIM), the energy of the transmitted particles was measured by a miniaturized high resolution gas ionization detector.

Kobayashi, *et al*. [20] developed an ion irradiation system in liquid using a tapered glass capillary with a thin window at the tip. In this study, polyethylene and polytetrafluoroethylene were irradiated with H^+ ions in an aqueous solution containing acrylic acid monomers. The irradiated surfaces that were originally hydrophobic became hydrophilic due to the surface layer formed by the acrylic acid polymer.

Nebiki, *et al*. [2] applied the beam focusing using a tapered glass capillary to in-air PIXE measurements. By using capillaries having 10-20 μm outlet diameters, they obtained several hundreds pA of 4 MeV He^{2+} ion beams and applied it to PIXE

analysis of the seabed sludge without any sample treatments. A comparison of spectra between wet and dry sludge sample suggested the usefulness of this new technique.

Fujita, *et al.* [6] developed a two-dimensional mapping technique with in-air-PIXE (2D-PIXE) using a metal capillary as a guide to extract ion beam to air. The metal capillary was a conventional syringe needle with a 200 μm inner diameter. For a target composed from copper wires on an aluminum basement, 2D-PIXE measurements were performed by irradiating it with a 3 MeV proton beam. They successfully reproduced the structure of the copper wire on the target and discussed the signal-to-noise ratio and the spatial resolution of the developed two dimensional mapping technique.

2.5 Monte-Carlo Simulation

To achieve higher beam transport efficiency, the ion transport mechanism in the tapered glass capillary needs to be investigated in more detail by using numerical calculations. Kojima, *et al*. [22] demonstrated that the beam density of 54MeV/c muons could be increased almost by a factor of two when a tapered glass tube was inserted coaxially along the muon beam. They used a Monte Carlo (MC) simulation and explained the beam density enhancement observed in their experiment.

Schiessl, *et al*. [23] presented the simulation of guiding of multiply charged projectiles through insulating capillaries. They developed a classical trajectory transport theory that relates the microscopic charge-up with macroscopic material properties. Transmission coefficients, angular spread of transmitted particles, and discharge characteristics of the target were investigated.

To investigate the stochastic scattering process of MeV ions in the tapered glass capillary, Hasegawa, *et al*. [24] have developed a three-dimensional MC code. The MC simulation can be used to properly treat ion scatterings in the capillary glass body, which is probably essential to explain the ion energy distribution observed in the experiments. In the present study, we used this MC code to investigate the ion transport mechanism through the capillary under various conditions.

Because most of the scatterings closely related to beam focusing in the capillary occur in a MeV energy range, the code considers only elastic collisions between incident protons and atoms composing the capillary wall. Moreover, the Coulomb potential between two bare nuclei is used for scattering orbit calculation,

because even for the smallest scattering angle treated in the code (1 mrad) corresponding impact parameters for MeV protons are relatively smaller than the typical radii of the inner-shell electron orbits of the target atoms. This simplification in the interatomic potential model can reduce the calculation time drastically. Considering the above assumptions, the differential scattering cross section is expressed by the following well-known Rutherford formula:

$$\frac{d\sigma}{d\Omega} = \frac{b^2}{16\sin^4\left(\frac{\theta}{2}\right)}, \tag{2.10}$$

$$b = \frac{Z_1 Z_2 e^2}{4\pi\varepsilon_0 E_c}. \tag{2.11}$$

Here, b is the collision diameter, which corresponds to the distance of the closest approach in a head-on collision between the projectile and the target atom, and θ is the scattering angle in the center-of-mass system. Z_1 and Z_2 are, respectively, the atomic number of the projectile and the target atom, e is the charge of an electron, and ε_0 is the electric permittivity of vacuum. E_c is the collision energy available in the center-of-mass system given by

$$E_c = \frac{M_2 E}{M_1 + M_2}, \tag{2.12}$$

where M_1 and M_2 are, respectively, the masses of the projectile and the target atom, and E is the projectile kinetic energy in the lab system.

The mean free path, λ, of the projectile in the target is calculated from the total scattering cross section as follows:

$$\lambda = \frac{1}{N\sigma_T}, \tag{2.13}$$

where N is the target atomic number density. It is well known that the total scattering cross section, σ_T, for the Coulomb potential becomes infinity if all possible scattering angles from 0 to π are considered. To avoid this divergence, the minimum cutoff angle, θ_{min}, is introduced in the calculation of σ_T as follows:

$$\sigma_T = \int_{\theta_{min}}^{\pi} \frac{d\sigma}{d\Omega} 2\pi \sin\theta d\theta . \tag{2.14}$$

The use of the minimum cutoff angle corresponds to neglecting collisions with scattering angles smaller than θ_{min}. For the Rutherford differential scattering cross section, Eq. (2.14) is analytically integrated and results in

$$\sigma_T = \frac{\pi b^2}{2}\left(\frac{1}{1-\cos\theta_{min}} - \frac{1}{2}\right). \tag{2.15}$$

To trace a projectile ion in the target, distance to a first collision point, l , a kind of target atom encountered, s, and a scattering angle of the projectile after the collision, θ, must be determined in each scattering event according to their respective probability distribution function, $P_1(l)$, $P_2(s)$, and $P_3(\theta)$. The probability that the projectile has a first collision between l and $l+dl$ is written by

$$p(l) = N\sigma_T \exp(-N\sigma_T l) dl . \tag{2.16}$$

By integrating Eq. (2.16) and substituting Eq. (2.13), $P_1(l)$ is derived as follows:

$$P_1(l) = \int_0^l p(l) dl = 1 - \exp(-l/\lambda) . \tag{2.17}$$

$P_2(s)$ is given by the fraction of each element in the target, f_s, s = 1, 2,…, n, as follows:

$$P_2(s) = \int_0^s p(\xi) d\xi , \tag{2.18}$$

where $p(\xi) = f_s$ for $s - 1 \le \xi < s$.

Finally, $P_3(\theta)$ is written by the differential scattering cross section and the total scattering cross section given in Eqs. (2.10) and (2.14),

$$P_3(\theta) = \frac{1}{\sigma_T}\int_{\theta\min}^{\theta} \frac{d\sigma}{d\Omega} 2\pi \sin\theta d\theta$$

$$= \frac{\left(1-\cos\theta_{\min}\right)^{-1} - \left(1-\cos\theta\right)^{-1}}{\left(1-\cos\theta_{\min}\right)^{-1} - 1/2}. \qquad (2.19)$$

By generating random number, r_1, r_2, and r_3, which are uniformly distributed on the interval $0 \le r < 1$, and solving equations $r_n = P_n(x)$, n = 1, 2, and 3 for $x = l$, s, and θ, respectively, these physical values are calculated.

2.6 PIXE analysis

2.6.1 Introduction to PIXE

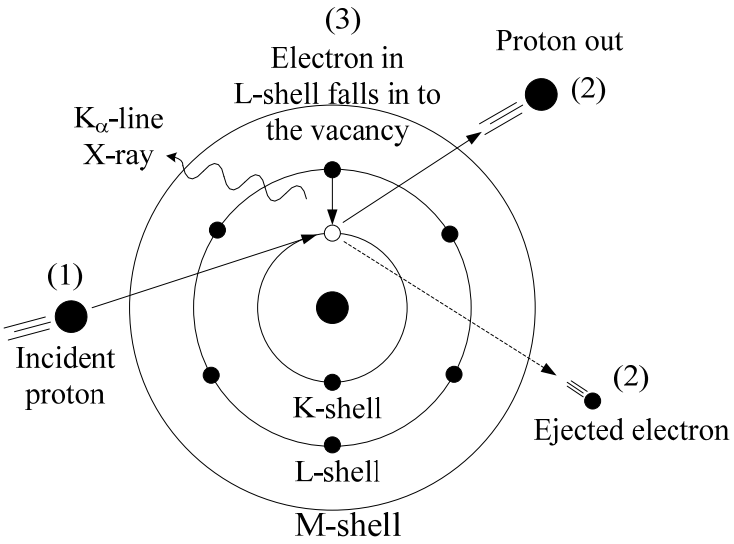

Fig. 2.3 Characteristic X-ray productions in PIXE (case of K_α emissions)

The particle induced X-ray emission (PIXE) is a well-known technique as a trace element analysis method using a few MeV ion beam. This technique can be applied to various fields such as biology, medicine, environment, earth sciences, art

and archaeology [10]. Figure 2.3 shows a schematic to explain the principle of PIXE. A common projectile source for PIXE analysis is a tandem accelerator with a terminal voltage of 1.5 MV that provides protons with an energy of 3 MeV [10]. A high energy proton from an accelerator interacts with the inner electron shell of an atom, resulting in knocking out of an electron from K-shell. To restore equilibrium of energy of the atom, an electron from an outer shell having higher energy level falls to refill this K-shell vacancy. Since the inner shell has lower energy level, the excess energy is emitted in the form of an X-ray. The released X-ray has a characteristic wavelength and energy due to the specific arrangement of electrons in each atomic species. So we can analyze the elemental composition in the sample by detecting this characteristic X-ray. Furthermore, the amount or concentration of elements in the sample can be determined from the characteristic X-ray intensities.

An important advantage of PIXE is that its sensitivity is high and multiple elements in a sample can be analyzed simultaneously. Furthermore only several tens of μg is enough to analyze the elements in a sample. The PIXE has the capability to measure many elements, in principle, from sodium to uranium in one measurement with little variation in sensitivity. It is also suitable for determining elements in a light-element matrix. Such a multielemental character of the spectrum analysis is based on the good separation of the X-ray peaks obtained by the X-ray detector. Also, in general, PIXE is a nondestructive technique because the irradiated solid sample is not seriously damaged by the proton beam at the required current densities.

Compared with other physical methods using the X-ray fluorescence technique with different exciting source, PIXE has somewhat better sensitivity and detection limit than X-ray excited XRF analysis where much more amount of sample is needed than PIXE. Furthermore, XRF cannot be combined with nuclear methods to provide light-element data [10]. In comparison to energy dispersive X-ray measurement with electron probe micro analysis (EPMA), an advantage of PIXE is its lower bremsstrahlung background and large X-ray cross section due to bombardment with proton, compared with electrons. Consequently, this fact leads to higher peak-to-background ratio on X-ray spectra. Thus, it has higher sensitivity enhanced by about a factor of 100 and has lower detection limits [10].

2.6.2 PIXE analysis of archaeological samples

Scientific studies of objects in art and archaeology often include analysis with a great variety of analytical techniques [10]. The method of examination and analysis should be nondestructive, that is, without the need to extract samples and without altering the composition or appearance of valuable and irreplaceable objects. Even if the samples must be taken, they should be of minimal size. A complicating factor is that many objects are heterogeneous. Furthermore, the technique should be fast, so that large numbers of objects from archaeological excavations and museum collection can be analyzed. Also the analytical method must be comparatively universal (i.e., applicable to many material and objects of any dimension), versatile (i.e., able to give both highly localized analyses of microscopic areas and average bulk analysis of heterogeneous materials), sensitive, and multielemental to give a maximum of information.

The interaction between light ions of MeV energy and matter is relatively nondestructive. The moderate and often negligible effects upon the irradiated material make analytical techniques based on MeV ions potential tools for characterizing objects of art and archaeological artifacts. Application of high-energy ion beams in both of these fields is mainly based on the PIXE technique, sometimes in combination with other simultaneous nuclear analytical techniques.

The information obtained from elemental analysis in art and archaeology is most often of interest in connection with problems of provenance and authenticity. For the scientist it often appears amazing how precisely the expert in artistic style can point to the place of creation of an artifact. However, the experts are not very good at describing the provenance of the material used, that is, the source of the raw material. If the elemental composition of an artifact is determined and compared with the composition of different raw material sources, it might be possible to draw some conclusions concerning the place of fabrication. A typical example is pottery, whose composition is determined mainly by the clay used in the manufactures.

2.7 Sangkhalok pottery

Sangkhalok pottery was produced during the 13th to 16th centuries at the ancient capital of the first Thai kingdom. Evidence from archaeological sites indicated that Sangkhalok in Thailand were exported to other countries from the 14th to the 16th centuries. The peak of exportation was reached in the 15th and early 16th centuries when there was a shortage of Chinese ceramics traded in the markets. Sangkhalok potteries have been discovered in the Lam Dong site in Vietnam, the Riau Archipelago in the Philippines, several sites in Indonesia, and even in Japan. The potteries were most probably exported from the trading capital of Ayutthaya near the Chao Phraya River in Thailand [25].

Sangkhalok pottery was produced in the form of tableware, ornaments or religious icons. The feature of Sangkhalok is painting patterns on white foundation and transparent surface coating. Sangkhalok potteries were warmly received in ancient export markets for their best quality and unique designs. They also came in different color. The two-color Sangkhalok had black patterns on a white background. There was also brown Sangkhalok and celadon Sangkhalok which has a wide range of green shades, including yellowish green, smoky green and olive green.

Chapter III
EXPERIMENTAL

Chapter III describes the experimental, materials and methods of this research including the tandem accelerator system, its beam-line components, and the detector and measurement system. The fabrication procedure of tapered glass capillary, the profile evaluation of capillary inner diameter as a function of axial position, and the investigation of axial symmetry of the capillary wall shape are explained. The chapter presents also the methods of beam experiments using capillaries with various wall materials and wall shape and the comparison between the experimental results and Monte Carlo simulations. Finally, the experimental apparatus to perform glancing-angle-scattering experiments using flat glass targets having different surface roughnesses and the experimental apparatus to demonstrate micro-PIXE analysis of archaeological samples are described.

3.1 Tandem accelerator system and beam-line components

3.1.1 Tandem electrostatic accelerator

This research was performed at the tandem electrostatic accelerator facility of Research Laboratory for Nuclear Reactors (RLNR), Tokyo Institute of Technology (Tokyo Tech.). A schematic of the accelerator system and its beam line is shown in Fig. 3.1. The maximum terminal voltage of the tandem accelerator (Model 5SDH-HC2, National Electrostatic Corporation) is 1.6 MV. A positive high voltage of the terminal is generated by transporting the electric charges to the terminal using a pair of chains and pulleys. This voltage is maintained by continuously transferring positive electric charges from the grounded end to the terminal. The amount of acceleration can be varied by changing the terminal voltage. Breeder resistors between acceleration gaps and gradient rings connected to the acceleration electrodes are used to homogenize the voltage gradient or the voltage per unit length along the column of accelerator. To prevent electric breakdowns between the terminal and the vessel of the accelerator, sulfur hexafluoride (SF_6) gas is filled in the vessel with a pressure of around 4 atm to achieve electric insulation.

In this study, negatively charged hydrogen ions (H^-) were produced by a Penning Ionization Gauge (PIG) type source or a cesium sputtering ion source and injected from ground potential into the accelerator. These ions were attracted and accelerated by the positively charged terminal. The ions were focused by a pair of Einzel lenses before the injection to the accelerator so that they could reach the terminal efficiently. Inside the terminal, a small amount of nitrogen gas was continuously injected in a narrow channel. When the H^- ions passed through the nitrogen gas, the collisions between the nitrogen molecules and the H^- ions induced the stripping of electrons from the H^- ions, resulting in the production of H^+ ions in the terminal. These positively charged ions were repelled by the terminal and accelerated again to the ground potential.

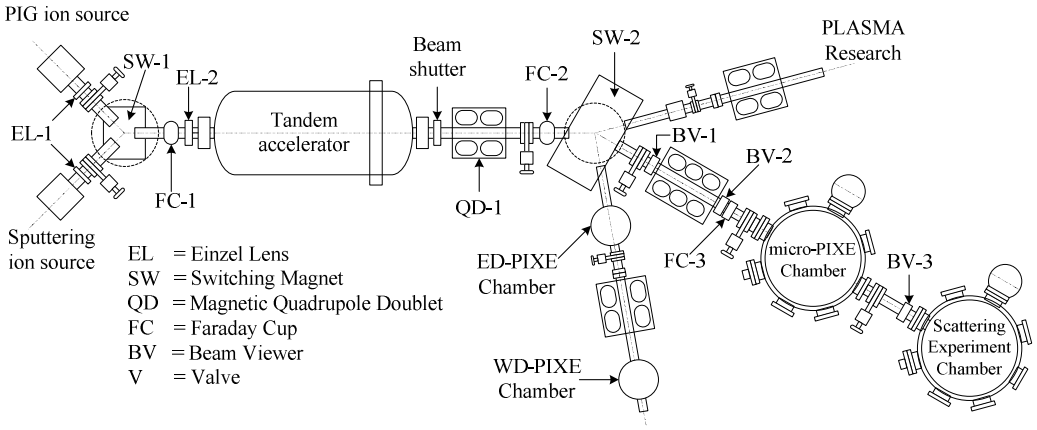

Fig. 3.1 Schematic of the tandem accelerator and the beam lines

3.1.2 Ion sources

In this research, two types of ion sources were used. These ion sources were connected to the accelerator through the switching magnet (SW-1) as shown in Fig. 3.1.

3.1.2.1 Penning Ionization Gauge (PIG) source

In this type of ion source, negative ions are produced from gaseous material. To produce negative hydrogen ions, the hydrogen gas is injected into the ion source chamber. The source consists of a cylindrical anode located between a pair of planar cathodes and a permanent magnet. An axial magnetic field from the permanent magnet is applied to the cylindrical anode. By applying a high voltage to the anode, a

low-temperature discharge plasma is produced in the anode cylinder. The resultant plasma consists not only of positive ions and electrons but also neutral atoms and even negative ions produced by dissociative electron attachment to the neutral molecules. The negative ions in the anode cylinder diffuse through a hole in the cylinder to the high vacuum side of the source where they are the extracted and formed into a beam by an extraction electrode.

3.1.2.2 Cesium sputtering ion source

The other type of ion source used in this research was a cesium sputtering ion source (Model SNICS II, National Electrostatic Corporation). In this source, negative ions are produced from solid materials. Cesium vapor comes from a cesium oven into an enclosed area between a cooled cathode and a heated ionizing surface. Some of the cesium condenses on the front surface of the cathode, forming a thin cesium layer. Some of the cesium is ionized by the hot surface of the ionizer. The cesium ions are accelerated towards the cathode and sputter the cathode surface under the condensed cesium layer. While the sputtered atoms pass through the cesium layer, they pick up electrons, resulting in negative ions. In this research, negative hydrogen ions were produced by using TiH_2 (Titanium hydride) as cathode material.

3.1.3 Beam-line components

3.1.3.1 Einzel lens

The Einzel lens (EL) is a device that focuses charged-particle beams without changing the beam energy. It consists of a cylindrical central electrode biased at positive high voltage and a pair of cylindrical electrodes at ground potential located on both sides of the central electrode. Positively charged particles entering the lens follow the field lines in the first gap, receiving an impulse toward the optical axis and a boost in velocity. When the ions pass the second gap, they are pulled outward, but since they are now closer to the axis and have more momentum, the change in direction is less than that in the first gap. In passing the second field, the beam is once again focused, but this time the ions are decelerated by the positive field to their original velocity. After exiting the lens, the charged particle beam continues to narrow toward its focal point downstream in the beam line. The Einzel lens is usually used for low velocity ions between the ion source and the main accelerator because the

focusing impulse is proportional to the transit time. The Einzel was used to focus the ion source before the accelerator.

3.1.3.2 Dipole magnet

The ion beam can be deflected by a dipole magnet that produces the magnetic field perpendicular to the ion beam axis. The orbit radius r of the ion beam in a magnetic field B is given by

$$r = \frac{Mv}{qB},$$

where M, v, and q are mass, velocity, and electric charge of ion, respectively. Therefore, ions with different velocities, masses, and charges can be separated using a dipolar magnetic field. In this research, a couple of dipole magnets were used to select ions having specific energy and charge state. The dipole magnet was used as the switching magnet (SW-1) to select the type of ion source. The switching magnet (SW-2) was used for bending the ion beam to the beam line.

3.1.3.3 Quadrupole magnet

The quadrupole magnet is used to focus charge particle beams. Figure 3.2 shows a schematic of quadrupole magnet and its magnetic field lines. The magnetic fields are canceled each other at the center of the quadrupole so the beam felt no force when it passes through the center of the magnet. Since the magnetic field strength is proportional to the displacement from the axis, the charged particle beam can be focused. However, while the beam is focused in the vertical direction, it is simultaneously defocused in the horizontal direction. To achieve the beam focusing in vertical and horizontal directions, a pair of quadrupole magnets, called quadrupole doublet (QD), are used, where the second quadrupole is rotated by 90 degrees with respect to the first one. The quadrupole doublet is often used for high-energy beams because the Lorenz force was proportional to the projectile velocity. In this study, the quadrupole magnet (QD-1) was used to focus the ion beam before injected to the beam line.

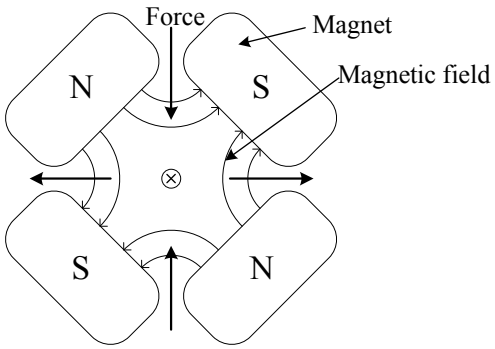

Fig. 3.2 Quadrupole magnet with magnetic field lines and the directions of force on the beam

3.1.3.4 Faraday cup

A Faraday cup is a tool for measuring the current of a charged-particle beam. This device consists of a conducting metallic cup that intercepts the beam. An electrical lead is attached to the cup to conduct the current from a cup to an ammeter. Thus, we can measure the beam current, which is proportional to the number of ions that strike on the Faraday cup. To prevent the escape of secondary electrons emitted from the bottom of the cup, this device is designed to be a cup-shape. In this research, remote-controlled Faraday cups (FC-1, FC-2, and FC-3 in Fig. 3.1) were used to monitor the beam current and optimize the magnet values.

3.1.3.5 Beam viewer

Several beam viewers were used to check the position, the shape, and the intensity of the ion beam. The viewer consists of a fluorescent plate mounted on an aluminum housing. When the ion beam hit the fluorescent plate, visible light was emitted and observed by a TV camera. The intensity of visible light is roughly proportional to the ion beam current density. In this research, two types of fluorescent materials were used depending on the beam intensity. The first one was fused silica (SiO_2), which emits the blue-white light from high-intensity beam and resists the radiation damage form high-intensity beam. The other one was polycrystalline ruby, which emits the red light. Since the fluorescent efficiency of the polycrystalline ruby is very high, so this type of beam viewers was used to observe the low-intensity beam.

These beam viewers were inserted into the beam line by remote control at the positions where observation of the beam was necessary.

3.2 Detector and measurement system

3.2.1 X-ray detector

To measure the X-ray from the target sample at the micro-PIXE chamber and scattering experiment chamber (Fig. 3.1), a Si-PIN detector (XR-100CR, AMPTEK) was inserted into these chambers. The detector has a 25-μm-thick Beryllium window to keep the vacuum, an effective area of 13 mm^2, a thickness of 300 μm, and an energy resolution of 214 eV (FWHM) for 5.9 keV photons. For the ED-PIXE Chamber, the X-ray was measured by a liquid-nitrogen cooled Si(Li) detector (Raytech 160-30-3SL). This detector has an 8-μm-thick Beryllium window, an effective area of 30 mm^2, a thickness of 3.2 mm, and an energy resolution of 142 eV (FWHM) for 5.9 keV photons.

3.2.2 Charged-particle detector

To measure the proton energy spectrum, an ion implanted silicon charged particle detector (ORTEC) was installed at the vacuum chamber. The detector has an effective area of 25 mm^2, and an energy resolution of 12 keV (FWHM) for 5.5 MeV alpha particles. The electric charge signal was sent to a preamplifier and then to a linear amplifier.

3.2.3 Preamplifier and Amplifier

The electric charges produced by the X-ray and proton in the detector were fed into a preamplifier, which was physically located close to the detector to minimize electronic noise. The preamplifier converted the charges to a voltage signal. The resulting signal was sent to a linear amplifier (427 Spectroscopy amplifier, ORTEC) which then produced an output pulse having approximately Gaussian shape. The height of pulse was proportional to the incident X-ray energy.

3.2.4 Multichannel Analyzer

A multichannel analyzer or MCA (ASPec-927, ORTEC) was used to analyze the height of the pulses from the linear amplifier in the range of 0 to 10 V. This MCA contained an analog-to-digital converter (ADC) in order to convert the pulse height into a digital signal. In this study, the MCA was set up at 2048-channel memory. The X-ray energy was calibrated by irradiating a stainless steel plate attached to the target holder. The K X-ray of Cr and Fe emitted from this plate were used as energy standards. The X-ray energy spectrum were displayed and analyzed on the personal computer connected to the MCA system.

3.3 Tapered glass capillary

3.3.1 Fabrication of tapered glass capillaries

The tapered glass capillary is fabricated from a straight glass tube. As a glass material for the tapered capillary, borosilicate glass is chosen most frequently because of its low softening temperature (~700 ºC). In this study, we used several types of straight glass tubes having various sizes and compositions. The specifications of the glass tubes are summarized in Table 3.1.

To extend a straight glass tube and form a gradually tapered capillary, a commercially available puller (PE-21, Narishige Co., Ltd.) was used (Fig. 3.3a), which consisted of a platinum heater and two types of electromagnets. Both ends of a straight tube were clamped tightly as shown in Fig. 3.3c, and then pulled while the middle part of the tube was heated up to a temperature beyond its softening point. By controlling the amount of heat and the pulling force, the tapered glass capillaries having various tapered angles were fabricated. After the pulling process, the tapered capillary typically had an outlet diameter less than 1 μm. To obtain a desired outlet diameter, a micro-forge device (MF-900, Narishige Co., Ltd.) shown in Fig. 3.3b was used to cut the tip of the capillary.

Table 3.1 Specifications of glass tubes used in this study.

Capillary #	Glass type	Elemental composition	Softening temperature(°C)	Outer/inner diameter (mm)
1	Borosilicate glass (Narishige Co., Ltd.)	60% O, 26% Si, 9% B, 3% Na, 1% Al	~700	2.00/0.80
2	Borosilicate glass (Premium corning 7056 Patch glass)	62.1% O, 21.5% Si, 9.8% B, 3.6% K, 1.1% Al, 1.3% Li, 0.6% Na	~718	1.65/1.20
3	Lead glass (Premium corning 8161 Patch glass)	62.7% O, 8.9% Pb, 25.4% Si, 2.5% K, 0.5% Ba	~600	1.65/1.20

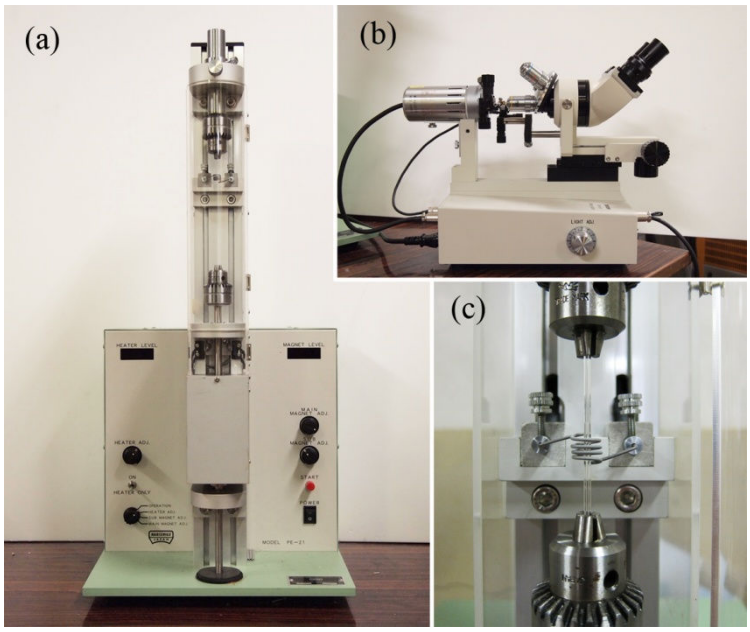

Fig. 3.3 (a) puller (PE-21, Narishige Co., Ltd.), (b) micro-forge device (MF-900, Narishige Co., Ltd.). (c) A straight glass tube clamped on the puller

3.3.2 Determination of axial profiles and checking of the axial symmetry of the capillary

For the precise measurement of the tapered shape obtained by the previous method, a dedicated device was developed. Figure 3.4 shows the device that consists of a long-working-distance optical microscope (VH-Z50L, KEYENCE Corp.) connected to a CCD camera (PL-B776U, PixeLINK), a drill chuck, a rotational stage, and a slide stage. A fabricated tapered capillary was fixed on the drill chuck and

rotated arbitrarily by the rotational stage with respect to the capillary axis. The drill chuck and the rotational stage were fixed on the slide stage. To digitize the inner wall shape of the tapered capillary, the magnified images of the capillary were taken using a CCD camera connected to an optical microscope with changing the axial position of the capillary. The absolute dimensions of the capillary were determined by image processing software (PixeLINK μScope, PixeLINK) based on the images of a micro ruler (Cross Stage Micrometer, Edmund Optics Inc.) taken together with the capillary. The inner diameter of the capillary was precisely measured from these images every 0.2 mm along the center axis of the capillary.

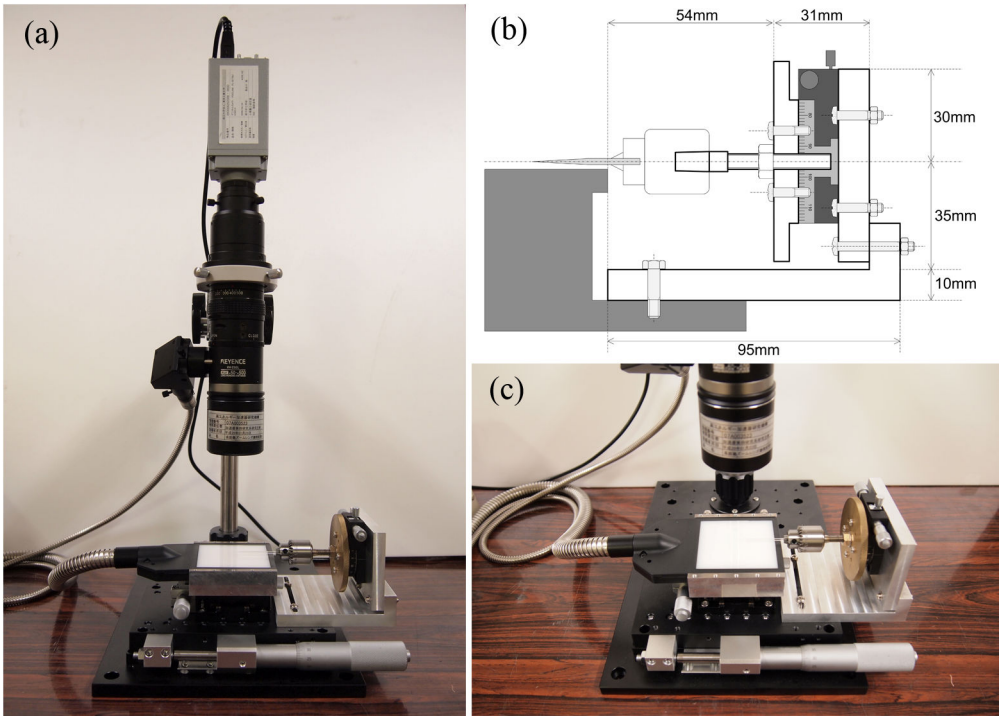

Fig. 3.4 (a) Long-working-distance optical microscope connected to a CCD camera. (b) Schematic view and (c) a picture of the device for capillary wall profile measurement

3.4 Investigation the transport mechanism of MeV protons

3.4.1 Beam-experiment configuration and alignment method of the capillary

To investigate the mechanism of transportation and focusing of MeV protons through the tapered glass capillaries, the beam-focusing experiments were performed in a vacuum chamber at a pressure of approximately 10^{-4} Pa. The configuration of the experimental apparatus in the chamber is schematically shown in Fig. 3.5. The tapered glass capillary was mounted on a stainless steel holder and its tilt angles were adjusted with respect to the beam axis using remote-controlled actuators. The incident proton beam from the accelerator was collimated by a 2-mm rectangular slit 2.2 m upstream of the capillary inlet and a 1.2 mm diameter aperture just in front of the capillary inlet. The beam energy was fixed at 2 MeV throughout this experiment.

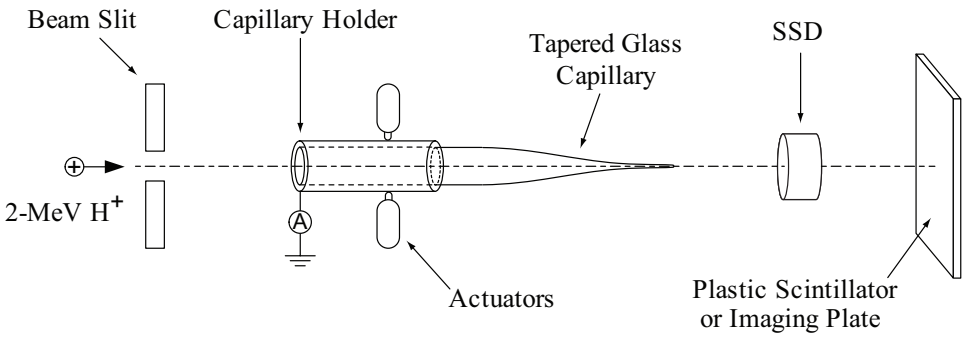

Fig 3.5 Schematic of the experimental setup

The capillary was precisely aligned with respect to the beam axis as follows. First, the capillary tilt angles were roughly adjusted by maximizing the brightness of a beam spot on a plastic scintillator 65 cm downstream from the capillary outlet. Then, the plastic scintillator was changed to an imaging plate (BAS-TR2025, Fujifilm Corp.) to record the intensity distribution of the proton beam. After beam irradiation for a few seconds, the beam-intensity distribution on the imaging plate was read out using a scanner as an image of photostimulated luminescence (PSL) intensity. The capillary tilt angles were finely adjusted until an image with a good axial symmetry was obtained.

3.4.2 Measurement of energy spectra of focused protons beams

The energy spectra of the protons focused by the tapered capillary were measured by using a silicon semiconductor detector (SSD) in two different experiment setups. First, the SSD was set right behind the capillary outlet and at 5 mm away. Because the detector solid angle was larger than the divergence angle of the proton beam, all protons exiting from the capillary were detected in this setup. In the other setup, the SSD was set 15 cm downstream from the capillary outlet. A 50-μm thick tantalum plate with a 100-μm diameter aperture was placed just in front of the SSD to decrease the detector solid angle. The SSD was mounted on the motorized stage, and the position of the SSD was changed every 0.125 mm perpendicular to the beam axis. The proton energy spectra were measured at various radial detector positions, and the beam intensities were evaluated from the total proton counts. To avoid unwanted effect of the incident-beam current fluctuation, the beam intensity was normalized by the total proton charge deposited on the capillary holder.

3.4.3 Numerical simulations using a Monte Carlo code

Transmission of 2 MeV protons in the tapered capillary was numerically simulated by using an originally developed MC code. In this code, the classical Rutherford scattering formula was used for the calculation of the scattering cross section. The stopping power of the wall material for the protons was imported from the SRIM database [26]. We examined not only the ion transmission in the borosilicate-glass and the lead-glass capillaries but also that in capillaries made of single elements such as Be, C, Al, Fe, Ag and Au to obtain a more general view of the effect of the wall atomic number. In addition, the ion transmission in a tapered capillary having a constant taper angle was calculated to examine the effect of the capillary wall shape. In this research, this capillary was called “conical capillary” to distinguish it from the tapered capillary actually used in the experiment. In the MC simulation, the conical capillary was defined as having the same outlet/inlet diameters and taper length as the tapered capillary.

3.5 Glancing-angle-scattering experiments using flat glass targets

3.5.1 Flat glass targets

To examine the effect of wall surface roughness on the beam transport through the tapered capillary, a beam scattering experiment was conducted with the flat glass targets having different surface roughnesses. In this experiment, we used flat glass plates (Sigma Koki, 20 mm × 30 mm, 5 mm thick) commercially available as base plates for optical components. The glass material is BK7 that has the composition as follows: 69.13% SiO_2, 10.75% B_2O_3, 3.07% BaO, 10.40% Na_2O, 6.29% K_2O and 0.36% As_2O_3. The accuracies for surface roughness of the base plates were λ and λ/20, here λ = 632.8 nm. Thus, the λ/20 flat glass have a maximum peak to valley deviation of around 30 nm. Figure 3.6 shows the flat glass plates used in this experiment. The specifications of the glass plates are summarized in Table 3.2.

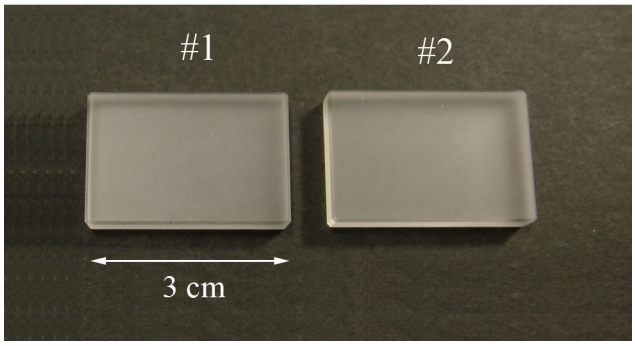

Fig. 3.6 Flat glass plates used in this study, which have different levels of surface roughness

Table 3.2 Specifications of flat glass targets.

Flat glass #	Surface roughness	Maximum peak to valley deviation (μm)
1	λ	0.6
2	λ/20	0.03

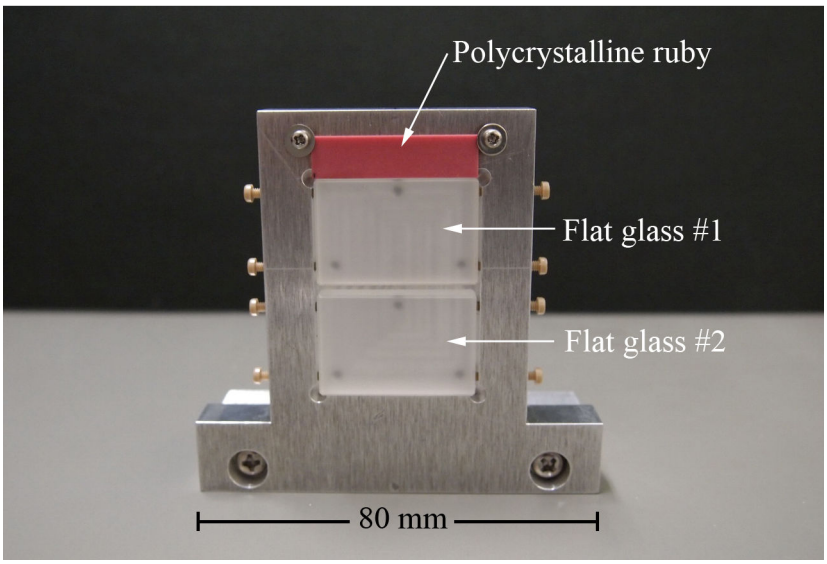

Fig. 3.7 Holder for flat glass targets and a polycrystalline ruby plate

To hold the flat glass plates on the beam axis, an aluminum target holder was designed and fabricated as shown in Fig. 3.7. The glass plates were set on the pit structure of the holder and fixed by plastic screws on the side walls. To observe the beam spot and check the beam position during the experiment, a polycrystalline ruby plate was also mounted on the holder so that the surface of the ruby plates share the same plane with the flat glass surfaces.

3.5.2 Experimental apparatus

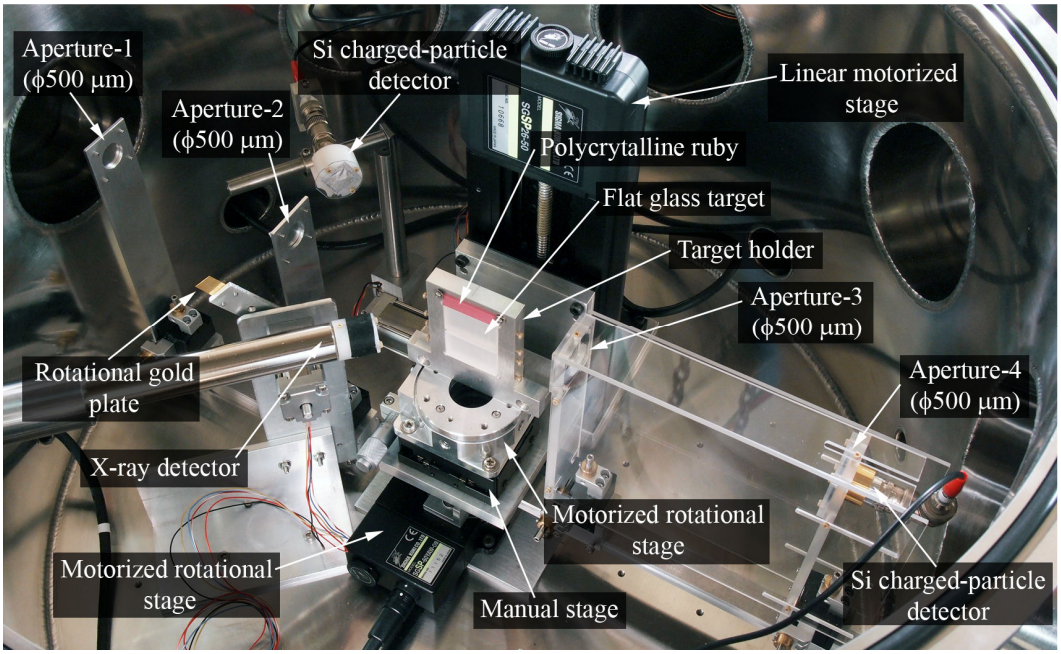

Fig. 3.8 Experimental setup for the glancing-angle-scattering experiment

Figure 3.8 shows the experimental setup for the glancing-angle-scattering experiment. This experiment was performed in a large vacuum chamber, which was evacuated by a turbo molecular pump to less than 10^{-3} Pa. A 2-MeV proton beam from the tandem accelerator was injected into this chamber. To observe the beam spot, a SiO_2 beam viewer was installed in the beam line just before the chamber. At the center of the chamber, the target holder was mounted on motorized rotational stage (SGSP-60Y AW-OB, Sigma Koki Co., Ltd.) so that the target holder could be rotated by this stage. To adjust the target holder and the rotational stage, these two devices were put fixed on a linear motion stage, which was used to align the target surface on the beam axis before the experiment. These two stages were supported by a linear motorized stage (SPSG26-55, Sigma Koki Co., Ltd.), which was used to change the position of the target in the vertical direction. Another rotational stage (SGSP-60YAW-OB, Sigma Koki Co., Ltd.) put on the bottom of the chamber was used to rotate the detector arm. To limit the range of proton incident angle, two apertures (Aperture-1 and Aperture-2) were placed at 225 mm and 105 mm from the target center, respectively. Two additional apertures (Aperture-3 and Aperture-4) were set in front of the detector to limit the target area seen by the detector. The radial positions of

these apertures were 5.5 cm and 19 mm, respectively. The diameter of these four apertures is 0.5 mm. The apertures were made on 50-μm-thick aluminum plates. As shown in the figure, the two apertures downstream of the target and the detector were surrounded by the 2-mm-thick acrylic plates to prevent protons scattered by the chamber wall and the components except the target from entering the detector. Each aperture holder was mounted on a two-axis stage, which enables us to align the aperture precisely on the beam axis. To detect protons scattered from the flat glass target, a Si charge particle detector was mounted just behind the fourth aperture. In addition to this, a Si-PIN detector (XR-100CR, AMPTEX) was installed at –135° to measure X-rays emitted by the target. A Mylar film of 50 μm thick was placed in front of the X-ray detector to stop backscattered protons.

3.5.3 Normalization of the incident protons

To normalize the measured count of protons scattered from the flat glass target, we measured physical quantities that were closely related to the incident proton dose. One of them used for normalization was the beam current measured just before the target. A Faraday cup of 5 mm in diameter and 50 mm long was inserted to the beam line by a linear motorized stage (TSDM40-15X, Sigma Koki Co., Ltd.). The Faraday cup was connected to the current integrator (439 Digital Current Integrator, ORTEC) to accumulate charges delivered to the cup.

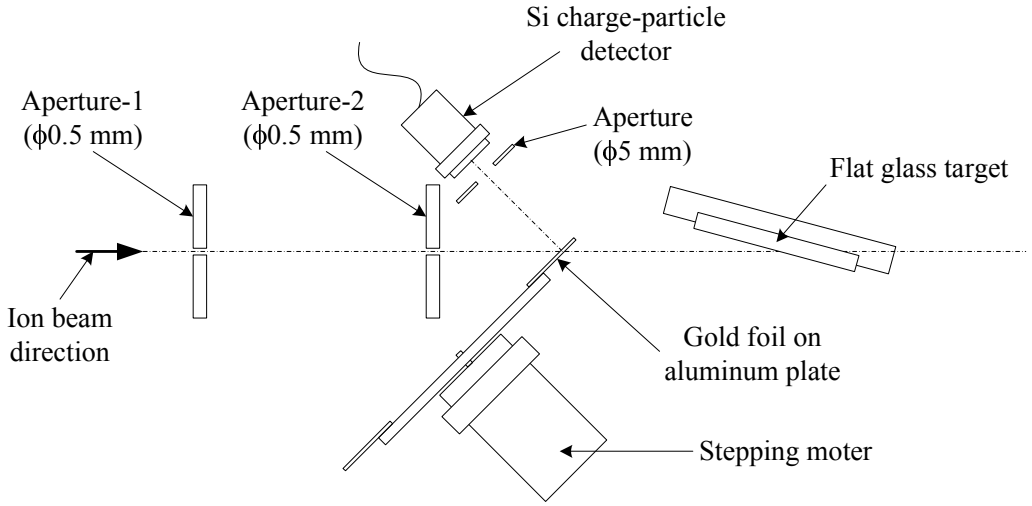

Fig. 3.9 Schematic of the gold rotational-plate system

To measure the incident proton dose during the measurement, a novel beam-sampling system using a rotating beam chopper was developed and installed as shown in Fig. 3.9. In this setup, the incident proton beam was chopped by aluminum plates fixed at both ends of the rotating fan driven by a stepping motor (TS3664N5, Sigma Koki Co., Ltd.). The aluminum plate was 100 μm thick and 2-μm-thick gold foil was attached on the surface of the plate by vacuum grease. The rotational speed of the fan was typically 1 rad/s and controlled by a remote computer. The size of the chopper plate was designed so that 4% of the incident beam could be chopped.

Protons backscattered from the gold foils were measured by a Si charged-particle detector, which was installed 5 cm away from the gold foil surface. To observe the backscattered protons only from the gold foils, a 100-μm aluminum plate with an aperture of 5 mm in diameter was put at 10 mm in front of the detector. Clearly, the count rate of the backscattered protons can be regarded to be proportional to the incident proton beam current if the rotation frequency is higher than the typical beam fluctuation frequency. Thus, we used this chopper system for the normalization of the incident beam current under a fan rotation speed satisfying the above condition.

3.6 Micro-PIXE experiments using a capillary-focused microbeam

3.6.1 Investigation of the performance of micro-PIXE system

To investigate the performance of the micro-PIXE system using tapered glass capillary, a tapered glass capillary and its control device were installed in the micro-PIXE chamber. The outlet and inlet of tapered glass capillary are 10 μm and 0.8 mm, respectively. The tapered glass capillary was mounted on the stainless steel holder. We used two remote-controlled actuators to adjust the tilt angle of the capillary holder in horizontal and vertical direction. To roughly align the capillary on the beam axis, a plastic scintillator plate was placed 65 cm downstream from the capillary outlet. The capillary tilt angles were adjusted by maximizing the brightness of the fluorescence. Then, the plastic scintillator was changed by the imaging plate. The tilt angles of the capillary holder were precisely adjusted until the beam-intensity distribution with a good axial symmetry was obtained.

A 2-MeV proton beam was injected into the capillary and a micro beam was extracted from the capillary outlet. A target for micro-PIXE analysis was placed at 1 mm downstream from the capillary outlet. The target was moved by two-axis motorized stages in horizontal and vertical directions normal to the beam axis. The minimum step size of the motorized stages is 1 μm. The X-ray detector was installed at –135˚ to measure X-rays emitted from the target. To normalize the X-ray yield, a Si charged particle detector was installed at +135˚ to measure backscattered protons.

To investigate the performance of the micro-PIXE system, a copper thin plate was scanned by a 2-MeV proton micro beam that was extracted from a tapered glass capillary with an outlet diameter of 10 μm. The copper plate was mounted on an aluminum holder and moved by the two-axis motorized stages. A copper fine mesh (ϕ8-μm wire, 1000 mesh/inch) was also scanned in two dimensions to demonstrate the elemental mapping. The two-dimensional distribution of copper was reconstructed from the intensity of Cu-Kα X-ray and normalized by the count of the backscattered protons.

3.6.2 Archaeological sample

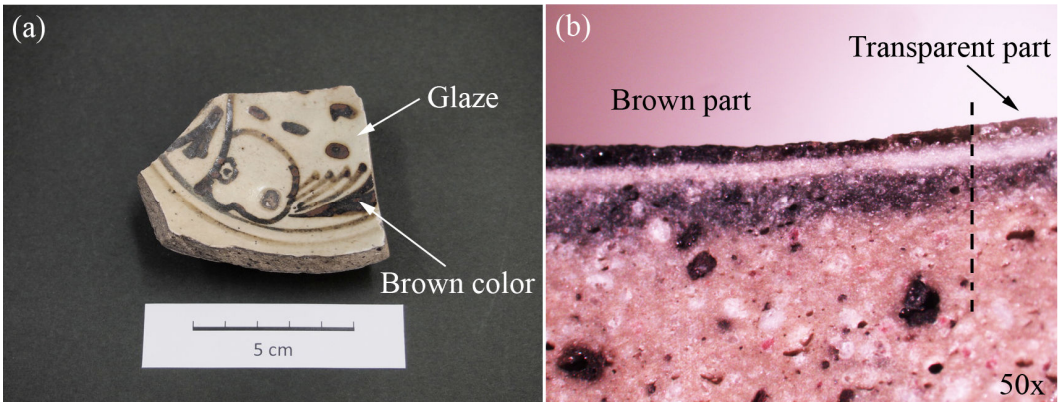

Fig. 3.10 (a) A piece of broken old Sangkhalok and (b) an image on cross section taken by optical microscope

To examine the feasibility of the tapered glass capillary as a compact beam-focusing device for actual micro-PIXE analysis, an archaeological sample was used in this research. This archaeological sample is a piece of "Sangkhalok" pottery, which has been unearthed in Sukhothai province of Thailand (Fig. 3.10). The surface of the sample has paint patterns with brown color on white foundation and transparent glaze coating. The cross section of the sample was carefully polished by fine sandpaper and cleaned by pure water in an ultrasonic bath. To observe the cross section near the pottery surface in more detail, magnified images of the cross section were taken by a CCD camera combined with an optical microscope. From the magnified image shown in Fig. 3.10b, the Sangkhalok pottery has three different layers: an outermost glaze layer, a white foundation layer, and a substrate layer. Moreover, the outermost layer consists of two parts with different colors; one is a brown part corresponding to the surface brown painting and the other is a transparent part where one can see the white foundation color from the surface. On the other hand, the substrate layer contains many coarse grains having various colors. In addition, the substrate includes some bubble structures, which may be caused in the production process based on the ancient ceramic technology. The thicknesses of the glaze and foundation layers were around 250 μm and 200 μm, respectively.

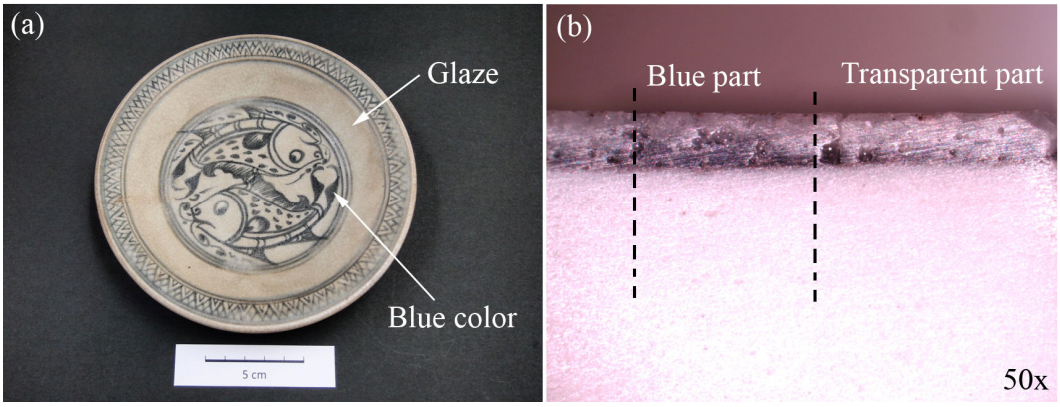

Fig. 3.11 (a) A modern Sangkhalok and (b) an image on cross section taken by optical microscope

In addition to the old Sangkhalok pottery, a “modern” Sangkhalok pottery (Fig. 3.11a), which was produced based on the present technology, was prepared in this research. The comparison between the old and present potteries might be useful to distinguish faked Sangkhalok potteries. Although this modern Sangkhalok pottery was produced at the same area (Sukhothai province) in Thailand, its production technology must be much more sophisticated than the old one used for the unearthed old Sangkhalok potteries, which results in differences in the appearance and texture of the pottery.

The sample for the measurement was cut out of the pottery by a diamond saw and prepared by the same procedure for the old one. The cross section of the sample observed by the optical microscope is shown in Fig. 3.11b. The pottery consists of a glaze layer and a substrate layer. The substrate layer seems smooth and uniform, which is much different from that of the old one.

3.6.3 Preliminary investigation of elemental composition and X-ray from glass tube

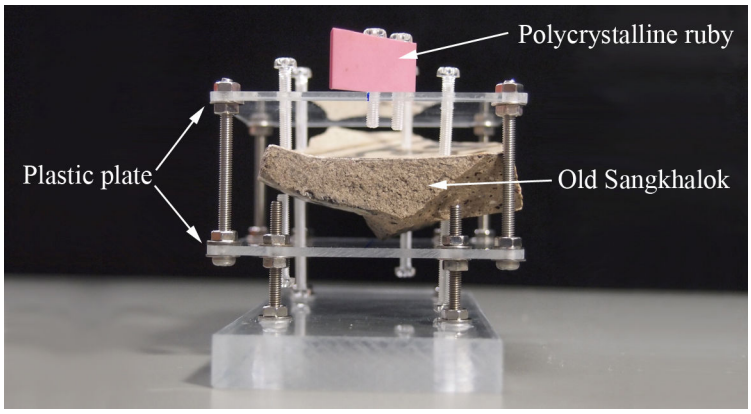

Fig. 3.12 Holder of old Sangkhalok sample

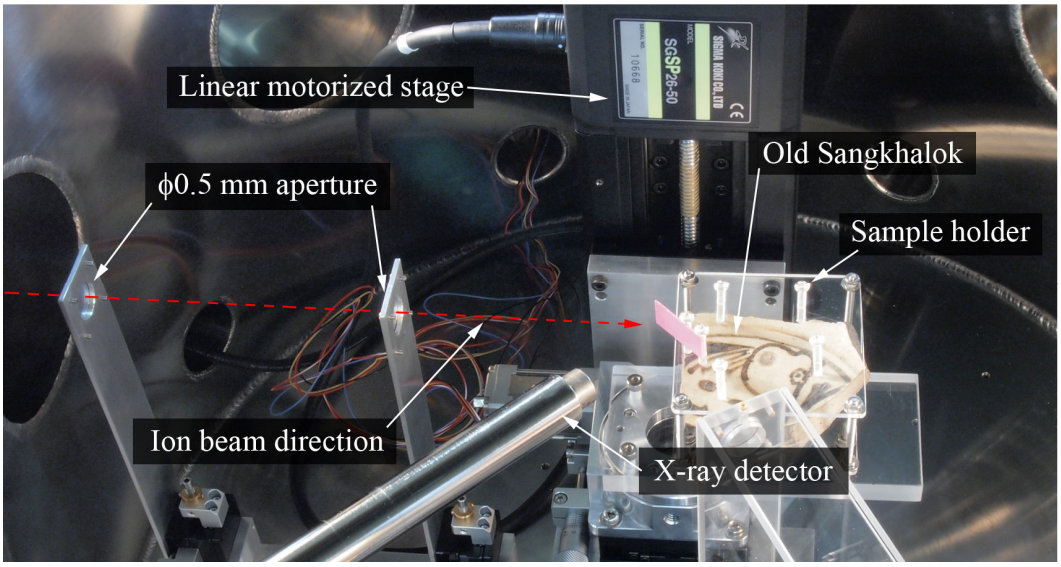

Fig. 3.13 Experimental setup for micro-PIXE analysis using two apertures

To roughly determine elemental composition of the old Sangkhalok, the experiment using a 500-μm-diameter beam was performed. Figure 3.12 shows the sample holder made of two acrylic plates. The pottery sample was sandwiched by the two plates and fixed by plastic screws. By adjusting these screws, the cross section plane of the sample was set perpendicularly to the beam axis. A polycrystalline ruby plate was also put on the top of the holder and installed at 45˚ with respect to the beam direction to observe the beam spot by a TV camera. Figure 3.13 shows the

experimental setup for micro-PIXE analysis. The sample holder was installed on the linear motorized stage, which moved the sample in vertical direction. Two apertures of 500-μm in diameter were installed 120 mm and 105 mm upstream of the sample, respectively. These two apertures limited the beam spot size on the sample to be around 0.5 mm. To detect X-rays emitted from the sample, a Si-PIN X-ray detector was installed at –135˚. X-ray spectra from the surface layer and the substrate layer can be measured independently by changing the sample position with linear motorize stage.

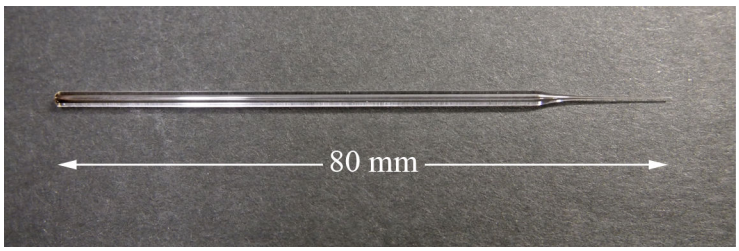

Fig. 3.14 Tapered glass capillary used in micro-PIXE analysis for archaeological sample

When we adopt the tapered glass capillary to the micro-PIXE analysis, there is a possibility that background X-rays emitted from the glass capillary itself interferes the observation of minor elements in the sample. Thus, we measured PIXE spectra of tapered glass capillaries made of three different glass materials as shown in Table 3.1. This measurement was performed based on the conventional PIXE technique, which is available at the ED-PIXE chamber of the tandem facility (Fig. 3.1). The borosilicate glass tube having an inlet diameter of 0.8 mm was selected for the fabrication of the tapered glass capillary for micro-PIXE analysis. A tapered glass capillary of 70 μm in outlet diameter and 7 cm long was fabricated as shown in Fig. 3.14.

3.6.4 Experimental setup for archaeological sample using tapered glass capillary

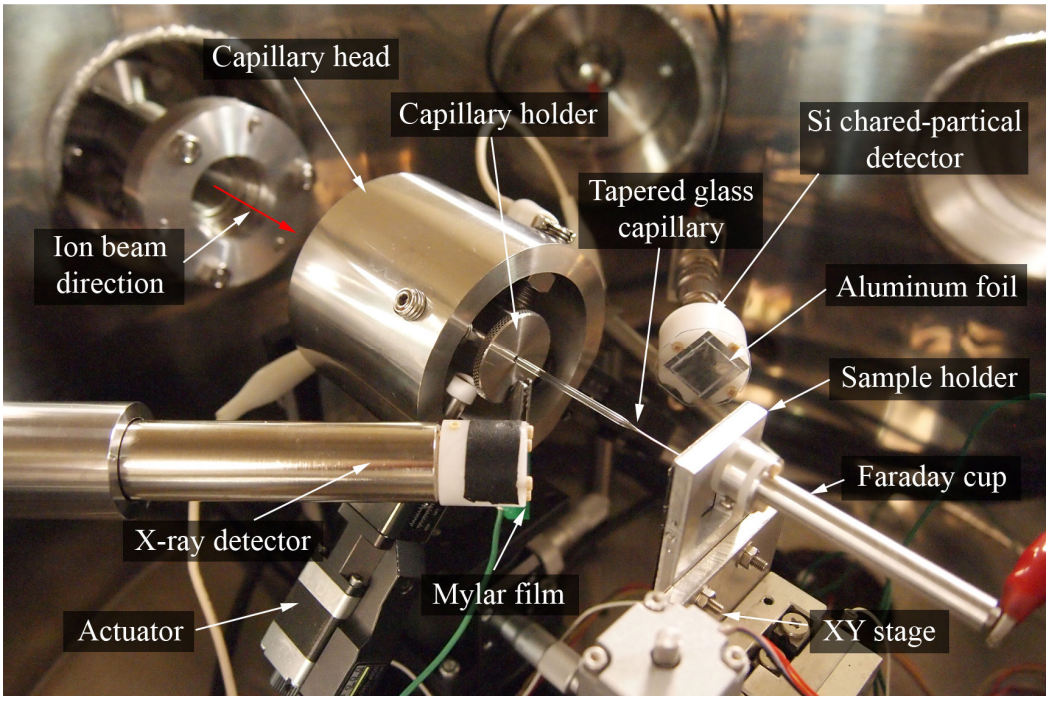

Fig. 3.15 The experimental setup for micro-PIXE analysis using tapered glass capillary

Figure 3.15 shows the experimental setup for micro-PIXE analysis using the ø70-μm tapered glass capillary. This experiment was performed in a large vacuum chamber with a pressure less than 10^{-4} Pa. The tapered capillary was mounted on the stainless steel holder and its tilt angles were controlled by two actuators. The capillary head was placed on a two-axis stage, which enables us to align the capillary inlet position with respect to the beam axis. To observe the beam spot before the capillary inlet, the SiO_2 beam viewer was installed just in front of the capillary head. The beam viewer was mounted with an angle of 45º with respect to the beam axis on a linear motorized stage, which could change the beam viewer position in the vertical direction. A TV camera observed the fluorescence from the SiO_2 viewer through a top acrylic flange of the chamber.

The holder for the archaeological sample was made of aluminum and connected to the two-axis motorized stage. To measure the beam current from the capillary outlet, the Faraday cup was also installed on the sample holder. The carbon sheet was put on the front surface of the sample holder to reduce background X-rays

emitted from the sample holder. A small piece of the archaeological sample (pottery) was fixed on the sample holder using carbon adhesive tape. The distance between the capillary tip and the sample was around 1 mm. A Si-PIN X-ray detector and a Si charged-particle detector were installed at ±135° to measure X-rays and backscattered protons, respectively.

The elemental distribution in the sample was determined by scanning the 70-μm proton beam from the surface layer to the substrate laryer. For the demonstration of two-dimensional element mapping, a cross-sectional area of 630 μm × 980 μm near the pottery surface was scanned by the microbeam with a step size of 70 μm and a measurement time of 5 minutes per step. The two-dimensional distribution of each element was reconstructed from X-ray intensities normalized by scattered proton counts and beam current at capillary holder.

Chapter IV
RESULTS AND DISCUSSION

Chapter IV consists of the results and discussion on the shape and axial symmetry of the tapered glass capillary, beam spot patterns recorded on imaging plates, energy spectra, and intensity distributions of focused proton beams. The beam transmission and focusing properties are discussed by introducing the MC simulation results on the protons focused by the tapered capillary and the conical capillary, and the dependences of the focusing ratio on the atomic number of capillary wall. The results and discussion on the glancing-angle-scattering of protons by flat glass targets having different surface roughness are described. Finally, the feasibility of the tapered glass capillary as a compact beam-focusing device for the micro-PIXE analysis of an archaeological sample is examined.

4.1 Shape and axial symmetry of the tapered glass capillary

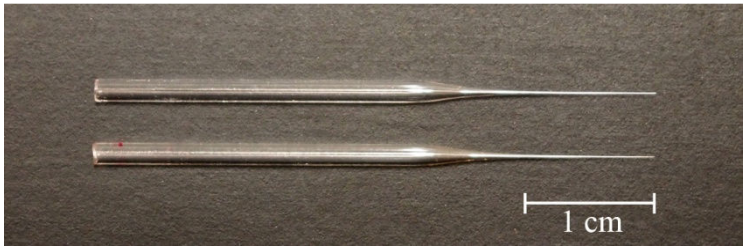

Fig. 4.1 A complete view of tapered glass capillaries made of borosilicate glass (upper) and lead glass (lower)

To reveal the effects of the capillary wall material on the beam-focusing ability, the tapered glass capillaries from borosilicate glass and lead glass tubes having the same nominal inner and outer diameter were fabricated. Because borosilicate glass and lead glass have different softening temperatures as shown in Table 3.1, the amount of heat and the pulling force was separately optimized for these two glass materials such that the tapered capillaries have the same inner wall shape. Fig. 4.1 shows the complete view of the tapered glass capillaries made of borosilicate glass

(upper) and lead glass (lower). The outlet diameter and the total length were approximately 30 μm and 4 cm, respectively. Magnified images of the capillary outlet taken by a scanning electron microscope (SEM) are also shown in Fig. 4.2a and b. The outlet diameters of the borosilicate-glass and the lead-glass capillaries were evaluated from these images to be 31.5 μm and 32.5 μm, respectively. Figure 4.3 shows the whole images of the capillary taper sections, which were reconstructed from the images recorded discretely by the developed device.

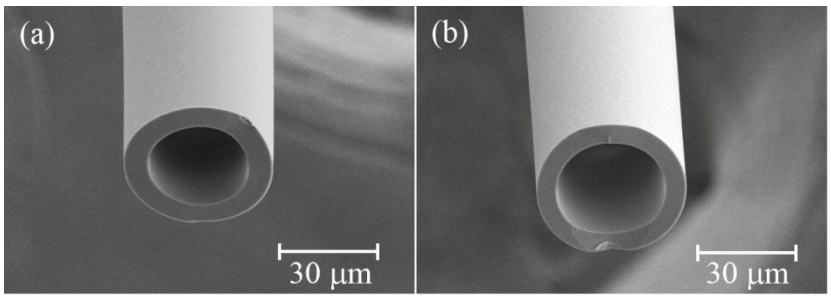

Fig. 4.2 SEM images of the capillary outlet of (a) borosilicate-glass and (b) lead-glass capillaries

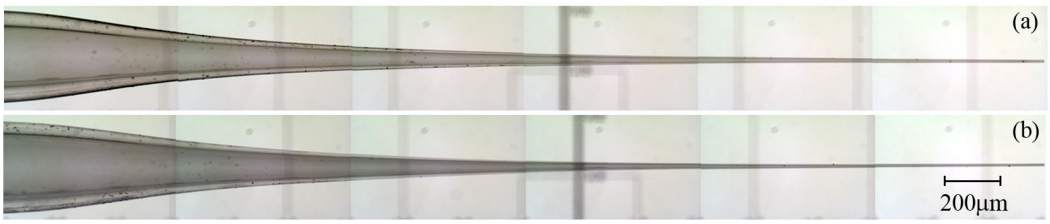

Fig. 4.3 Photograph of whole tapered (a) borosilicate-glass and (b) lead-glass capillary

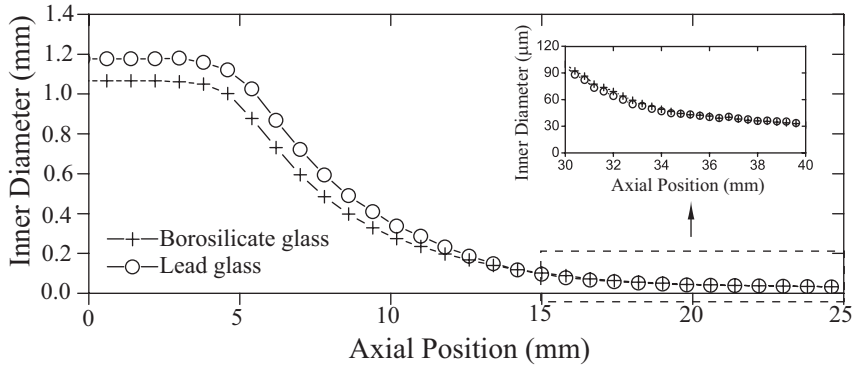

Fig. 4.4 Axial profiles of the inner diameter for borosilicate-glass and lead-glass capillaries

Figure 4.4 compares the inner wall shapes of the borosilicate-glass and the lead-glass capillaries. In this figure, the inner diameters at the inlet are not exactly the same, which is probably due to a manufacturing error of the original straight glass tube. On the other hand, the wall shapes around the tip are identical to each other, which is advantageous for the comparison between the beam-focusing abilities of these two capillaries because the inner wall near the tip is considered to be the main contributor to the beam transmission through the tapered capillary.

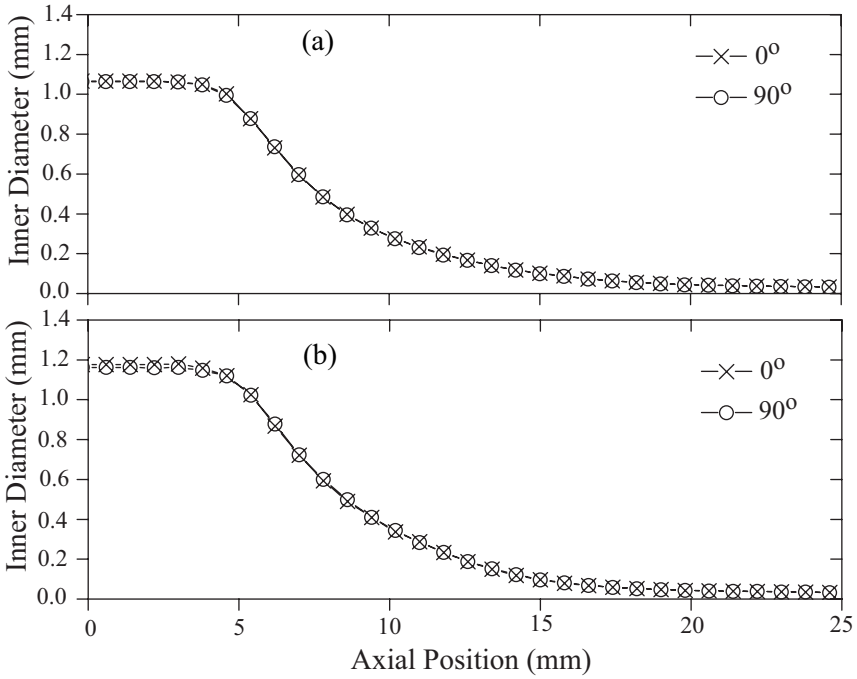

Fig 4.5 Comparisons of axial profiles of the inner diameter observed at 0° and 90° for (a) borosilicate-glass and (b) lead-glass capillaries

Figure 4.5a and b compare the inner-wall profiles measured at a rotation angle of 0° with those observed at 90° for the borosilicate-glass and the lead-glass capillaries. In these results, the profiles measured at both angles coincide well with each other and the axial symmetry is found to be very high. The outlet diameters measured by the optical microscope well reproduced those determined from the SEM images (Fig 4.2a and b), proving that the optical distortions due to the refraction of light are negligible in the measurement using the optical microscope.

4.2 Transport mechanism of MeV proton

4.2.1 Beam spot patterns recorded on imaging plates

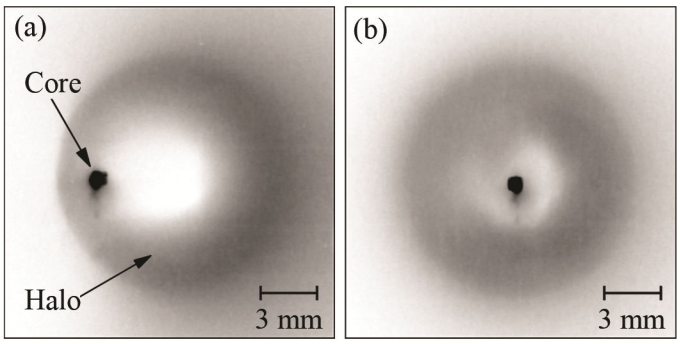

Fig. 4.6 Beam spot patterns recorded on imaging plates when the tapered capillary (lead glass) was (a) misaligned and (b) well aligned with respect to the incident beam axis. (Imaging plates were located 65 cm downstream from the capillary tip.)

Figure 4.6 shows the PSL intensity distributions on imaging plates irradiated by proton beams focused by the lead-glass capillary. As shown in the figure, the beam spot consists of an intense small spot called the “core” and a weak surrounding ring-shaped pattern called the “halo.” The core and the halo are composed of the protons traveling straight through the capillary and those scattered by the capillary inner wall, respectively. When the capillary axis is misaligned with respect to the beam axis, the core overlaps the halo ring and the halo ring pattern is asymmetric (Fig. 4.6a). After the optimization of the capillary tilt angle, the beam spot pattern becomes axially symmetric (Fig. 4.6b). However, even after the optimization, asymmetry is still

observed particularly in the halo ring. This is probably due to the in homogeneity of the incident beam profile.

4.2.2 Energy spectra of focused proton beams

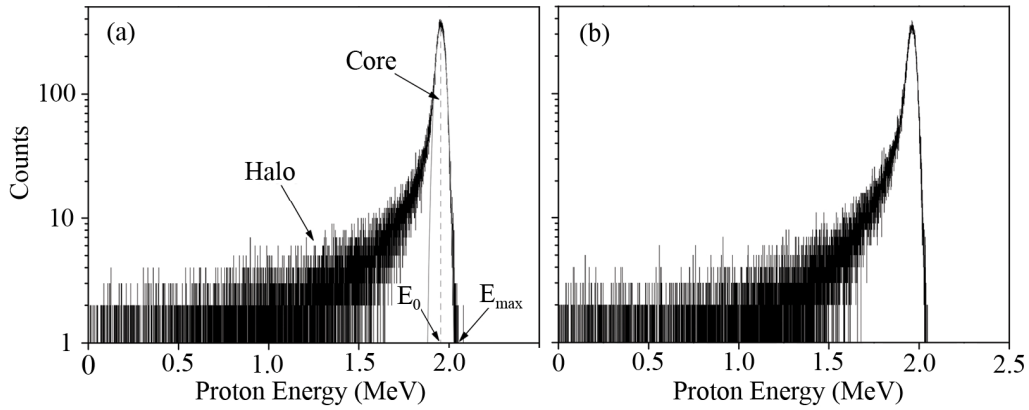

Fig. 4.7 Energy spectra of protons focused by (a) borosilicate-glass capillary and (b) lead-glass capillary. The gray solid and dashed lines in Fig. a show the core component and the proton incident energy, respectively.

Figure 4.7 shows the energy spectra of protons focused by (a) the borosilicate-glass capillary and (b) the lead-glass capillary. The spectra were measured by the SSD 5 mm downstream from the capillary outlet. There seems to be no considerable difference between these two spectra. Then, the numerical method was used for separation the total proton count into two parts corresponding to the core and the halo components, and the beam-focusing ratio from each energy spectrum were evaluated. By assuming that the protons in the core lost no energy in the capillary and considering the finite energy resolution of the SSD, the following formulae were used to estimate the total counts of the core N_{core} and the halo N_{halo}:

$$N_{\mathrm{core}} = 2\int_{E_0}^{E_{\max}} n(E)dE, \tag{4.1}$$

$$N_{\mathrm{halo}} = N_{\mathrm{total}} - N_{\mathrm{core}}. \tag{4.2}$$

Here, E_0 is the incident kinetic energy of the protons (2 MeV), $E_{\max}$ is the maximum energy of the protons in the spectrum, $n(E)dE$ is the count of protons having an

energy between E and $E+dE$, and N_{total} is the total count in the spectrum. The gray solid line in the figure shows the core component defined by Eq. (4.1). The beam-focusing ratio of the tapered capillary was evaluated from the following formula:

$$\eta = \frac{N_{\text{core}} + N_{\text{halo}}}{N_{\text{core}}} = 1 + \frac{N_{\text{halo}}}{N_{\text{core}}}. \tag{4.3}$$

From Fig. 4.7, the beam-focusing ratio of the borosilicate-glass and lead-glass capillary was obtained as shown in Table 4.1.

On the other hand, the effective atomic number for the Rutherford scattering process was calculated as follows:

$$Z_{\text{eff}} \equiv \left(\sum_i Z_i^2 f(i) \right)^{1/2}. \tag{4.4}$$

Here, Z_i and $f(i)$ are, respectively, the atomic number and the fraction of i-th element in the capillary wall. Although the effective atomic number of the lead glass is approximately thrice that of the borosilicate glass as listed in Table 4.1, the observed enhancement in the beam-focusing ratio was much lower than that expected from the dependence of the scattering cross section on the wall atomic number. This result implies that the scattering cross section was not a dominant factor determining the transmission and the focusing of MeV protons in the tapered capillary.

Table 4.1 Effective atomic number and beam-focusing ratio of the capillary glass.

Capillary glass	Effective atomic number	Beam-focusing ratio
Borosilicate glass (Premium corning 7056 Patch glass)	10.0	1.32
Lead glass (Premium corning 8161 Patch glass)	26.7	1.37

4.2.3 Intensity distributions of focused proton beams

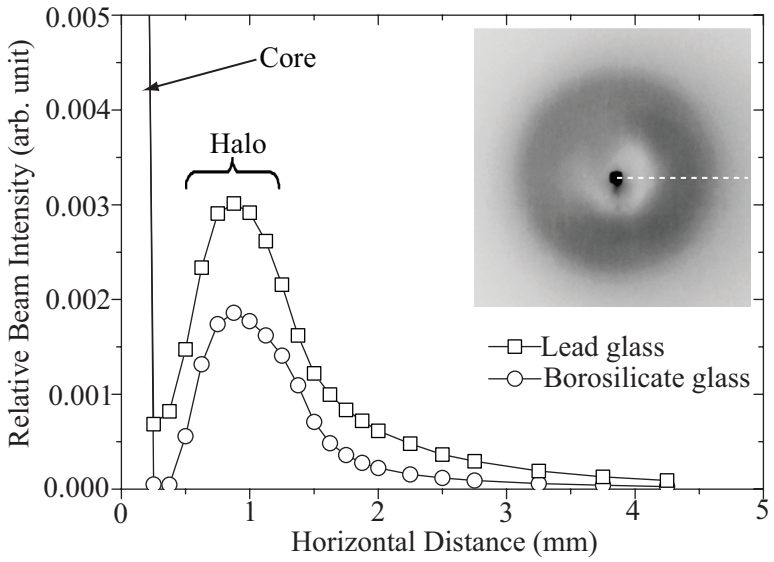

Fig. 4.8 Intensity distributions of the proton beams focused by borosilicate-glass and lead-glass capillaries. Beam intensities were evaluated along the dashed line in the beam spot image.

To discuss the effect of the wall atomic number on the beam-focusing process in greater detail, the core and the halo components were investigated separately. The intensity distribution of the proton beams, which were obtained by the spatially resolved energy spectrum measurement, are shown in Fig. 4.8 for the borosilicate-glass and the lead-glass capillaries. The intensity profiles were normalized by the respective intensities of the core components. As shown in the figure, the halo intensity peak for the lead-glass capillary is higher than that for the borosilicate-glass capillary. This result shows that the increase in the effective atomic number of the capillary wall actually leads to the increase in the scattered component intensity. However, according to the focusing ratios evaluated above, the increase in wall atomic number seems not to contribute to the total beam transmission so much.

4.2.4 The MC simulation results of protons focused by tapered capillary and conical capillary

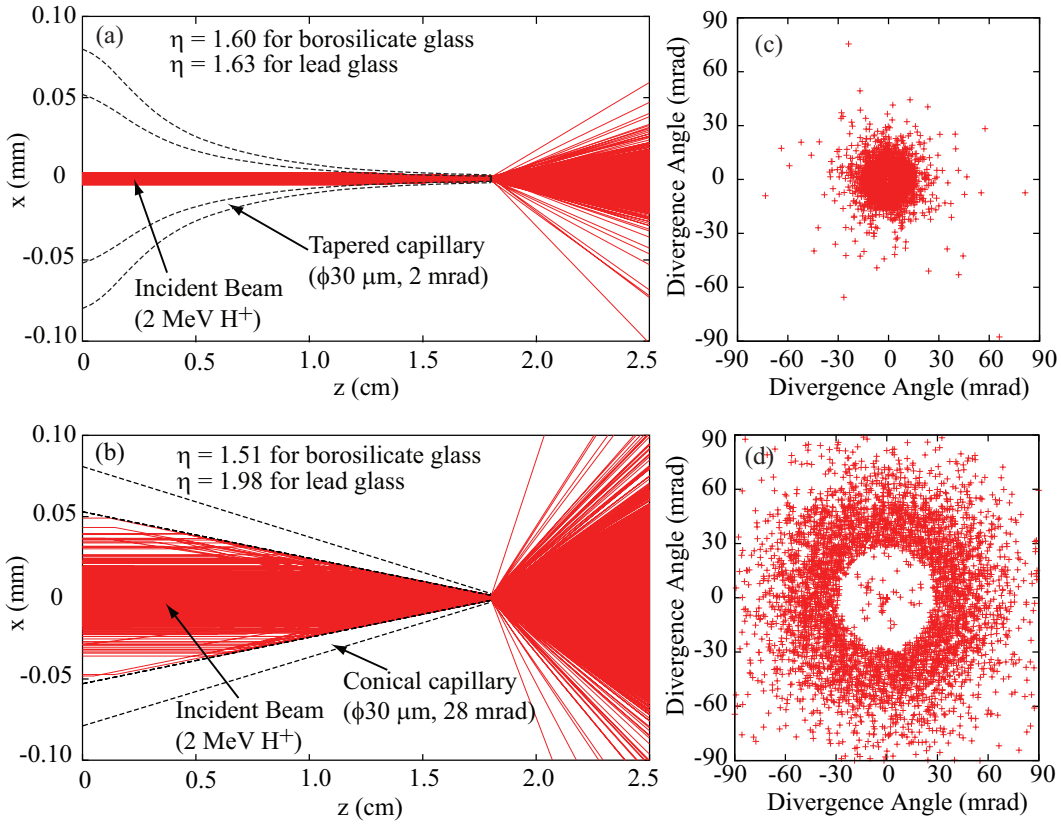

Fig. 4.9 Trajectories of protons focused by (a) a tapered capillary and (b) a conical capillary, and two-dimensional angular distribution of the protons on the detector of (c) a tapered capillary and (d) a conical capillary

Figure 4.9 shows the MC simulation results for proton trajectories in (a) the tapered capillary and (b) the conical capillary, and the angular distributions of protons focused by (c) the tapered capillary and (d) the conical capillary. Note that Fig. 4.9a and b show only the trajectories of the protons that finally exit from the outlet. As shown in Fig. 4.9a only the capillary inner wall near the outlet contributes to the beam focusing in the tapered glass capillary. This result justifies the use of the borosilicate-glass and the lead-glass capillaries having the same inner wall shape around the tip (see Fig. 4.4) in the experiment. The MC simulation result of the glass capillaries are summarized in Table 4.2. From the values of N_{core} and N_{halo} obtained in the MC simulation the focusing ratios were evaluated by Eq. (4.3) to be 1.60 and 1.63 for the borosilicate-glass and the lead glass capillaries, respectively. These values are

somewhat larger than those obtained from the experiment. This might be because the experimental focusing ratio was reduced by the inhomogeneity of the incident beam.

Table 4.2 MC simulation result of beam-focusing ratio

Capillary shape	Capillary glass	Effective atomic number	Beam-focusing ratio
Tapered capillary	Borosilicate glass	10.0	1.60
	Lead glass	26.7	1.63
Conical capillary	Borosilicate glass	10.0	1.51
	Lead glass	26.7	1.98

On the other hand, in the case of the conical capillary, almost all areas of the inner wall contribute to the beam focusing as shown in Fig. 4.9b. Particularly, when the wall material is lead glass, the effective use of the capillary inner wall results in the focusing ratio for the conical capillary (η = 1.98) being higher than that for the tapered capillary (η = 1.63). However, as shown in Fig. 4.9d, the use of the conical capillary evidently makes the distribution of the halo component more diffusive because of its larger angle (~28 mrad). Because the taper angle determines the minimum divergence angle of the halo particles, there is a trade-off between the beam-focusing ratio and the beam quality.

4.2.5 The dependences of the focusing ratio on the atomic number of capillary wall

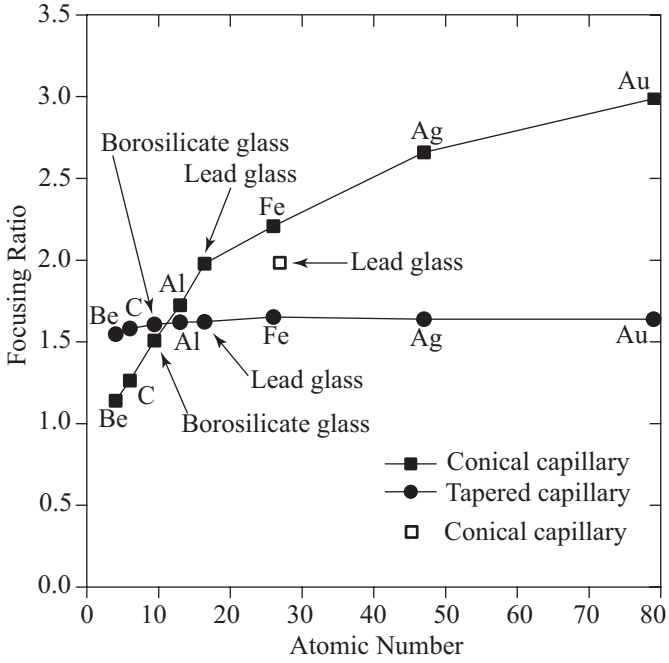

Fig. 4.10 Dependences of the focusing ratio on the atomic number of capillary wall materials calculated for a tapered and a conical capillary

Fig. 4.10 plots the beam-focusing ratios obtained from the MC simulation as a function of the wall atomic number. When the wall atomic number is relatively low (Be and C), the focusing ratios for the conical capillary are smaller than those for the tapered capillary. This is probably because the cross section is very small for MeV proton scattering by such light atoms with a relatively larger scattering angle (>28 mrad). With increasing wall atomic number, the focusing ratio for the conical capillary increases gradually and reaches a value approximately twice that for the tapered capillary when the wall material is gold. In addition, the focusing ratio for the tapered capillary seems to be almost independent of the wall atomic number. To understand these trends, we need to consider the fact that most scattering events occur not on the surface of the capillary inner wall but in the body of the wall. After being scattered by an atom inside the glass wall, the proton needs to escape from the wall to finally exit from the capillary outlet. Here, the distance that the scattered proton travels in the glass body after the scattering was defined as the “escape distance” (*a*

and *b* in the schematic illustration in Fig. 4.11). As for the tapered capillary, because the escape distance is relatively large because of its convex shape of the inner wall, most scattered protons are stopped inside the capillary wall and are unable to escape from it. This is consistent with the results in Fig. 4.9a, which indicate that the beam focusing occurs only at the capillary wall near the outlet where the escape distance is relatively small. The escape distance for the conical capillary is, on average, shorter than that for the tapered capillary, which results in the effective use of the capillary inner wall for beam transmission and relatively high focusing ratios.

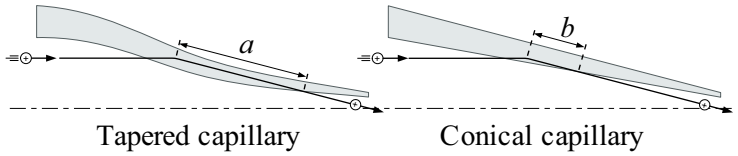

Fig. 4.11 Schematic of the escape distance for the tapered capillary (*a*) and the conical capillary (*b*)

Even for the conical capillary, the dependence of the focusing ratio on the wall atomic number (Fig. 4.10) is much weaker than that expected from the Rutherford scattering cross section. This result also supports the idea that the probability of the scattered proton escaping from the capillary wall predominantly determines the total transmission of MeV protons in the capillary. Because a heavier material has a higher stopping power for projectiles, the escape probability decreased with increasing wall atomic number even though the escape distance is constant. This effect probably reduces the contribution of the scattering cross section to the beam transmission and leads to the saturation of the focusing ratio for heavy-wall materials, as shown in Fig. 4.10. Note that the focusing ratios calculated for the borosilicate glass and the lead glass fit well on the curves predicted from the ratios for the single element materials when they are plotted with respect not to the effective atomic numbers Z_{eff} defined in Eq. (4.4) but to the averaged atomic numbers of the glass materials Z_{ave}, which is calculated simply by

$$Z_{\mathrm{ave}} \equiv \sum_i Z_i f(i). \tag{4.5}$$

A data point expressed by an open square in Fig. 4.10 shows the case when the focusing ratio of the lead-glass conical capillary is plotted with respect to the effective atomic number of the lead glass. Clearly, it deviates from the curve predicted by the single elements showing that the use of the effective atomic number is not so adequate. Since the stopping power is known to be almost proportional to the atomic number of the stopping medium, this result dose not contradict the hypothesis that the beam transmission through the capillary depends much more on the stopping power of the capillary wall for the projectile.

4.3. Glancing-angle-scattering of MeV protons by flat glass having different surface roughnesses

4.3.1 Normalization of scattered proton count

To normalize the measured count of protons scattered from the flat glass target, we monitored the following two physical quantities during the measurement: 1) the intensity of X-rays emitted from the target and 2) the number of protons backscattered by a beam chopper.

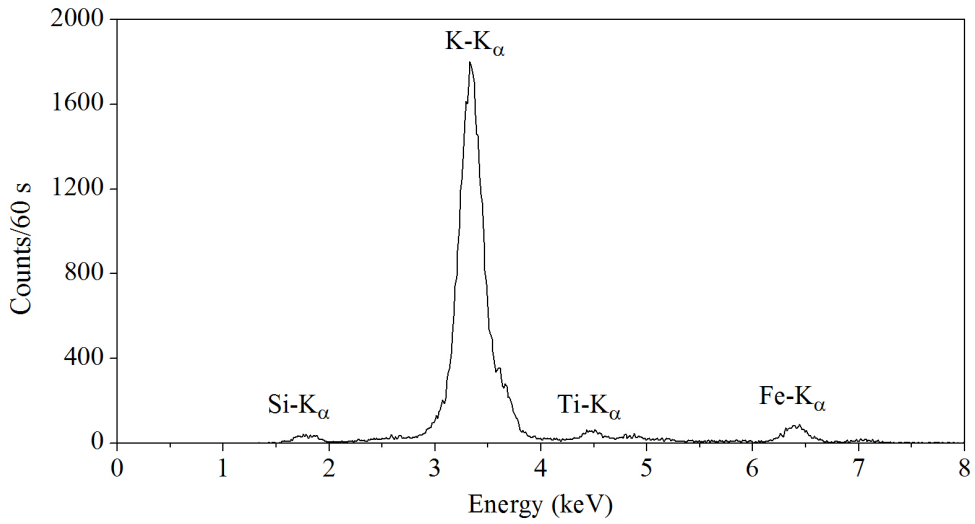

Fig. 4.12 X-ray spectrum of flat glass target

Figure 4.12 shows a typical energy spectrum of the X-rays emitted from the flat glass target during beam irradiation. Characteristic X-rays from the elements, particularly potassium, contained in the BK7 glass were clearly observed. Because the

X-ray intensity is proportional to the incident proton dose, the total count of the potassium K X-ray is considered useful for the normalization of the measured data.

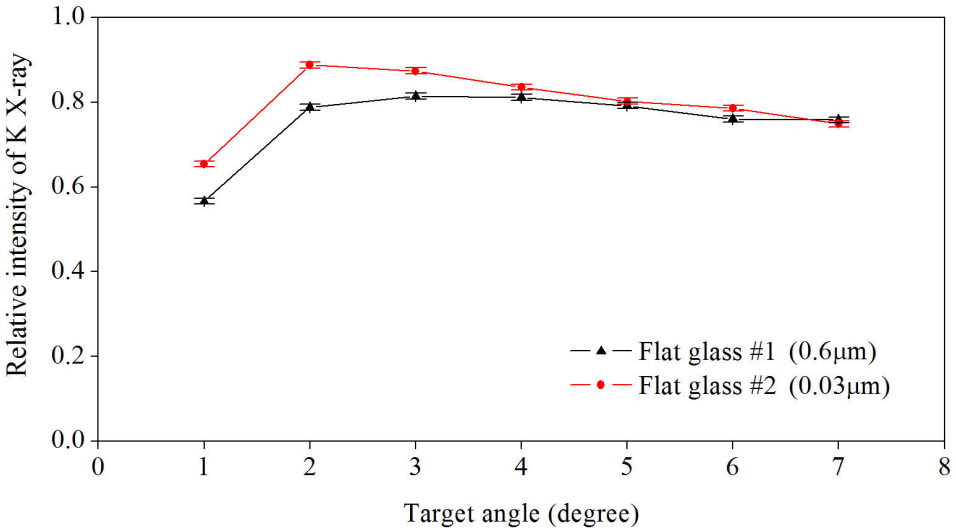

Fig. 4.13 Dependence of potassium K X-ray intensities from of flat glass targets on target angle

To confirm the applicability of the X-ray emission yield from the glass target to the data normalization, the X-ray spectra from the flat glass target were measured with changing the target angle. Then, the potassium K X-ray counts were normalized by the incident beam currents measured by a Faraday cup before and after the beam irradiation to the target. Figure 4.13 plots the intensity of potassium K X-rays as a function of the target angle. The measurement was performed for two types of glass targets having different surface roughnesses. The figure shows that the X-ray intensity slightly changes depending on the target angle. Moreover, the discrepancy in the X-ray intensity between two types of the targets becomes considerable at small target angles. Therefore, the X-ray yield from flat glass target was found not to be so suitable for the data normalization of this scattering experiment.

Another normalization method based on the Rutherford backscattering (RBS) measurement was tested by introducing a novel beam-sampling system using a rotating beam chopper. Figure 4.14 shows the energy spectra of the scattered protons from thin gold foils fixed on the rotating beam chopper plate (see Section 3.5.3). Each figure contains the results when 1) the chopper plate was fixed on the beam axis

without rotation (black), 2) the chopper was normally rotated (red), and 3) the chopper plate was fixed off the beam axis without rotation (green). The RBS spectra in the cases 1 and 2, one can see the rectangular peak corresponding to the protons backscattered by the gold foils. The ratio of the peak area in the case 2 to that in the case 1 was about 3.3%. This value is almost equal to the designed beam-chopping ratio (~4%), meaning that the beam-sampling system worked properly.

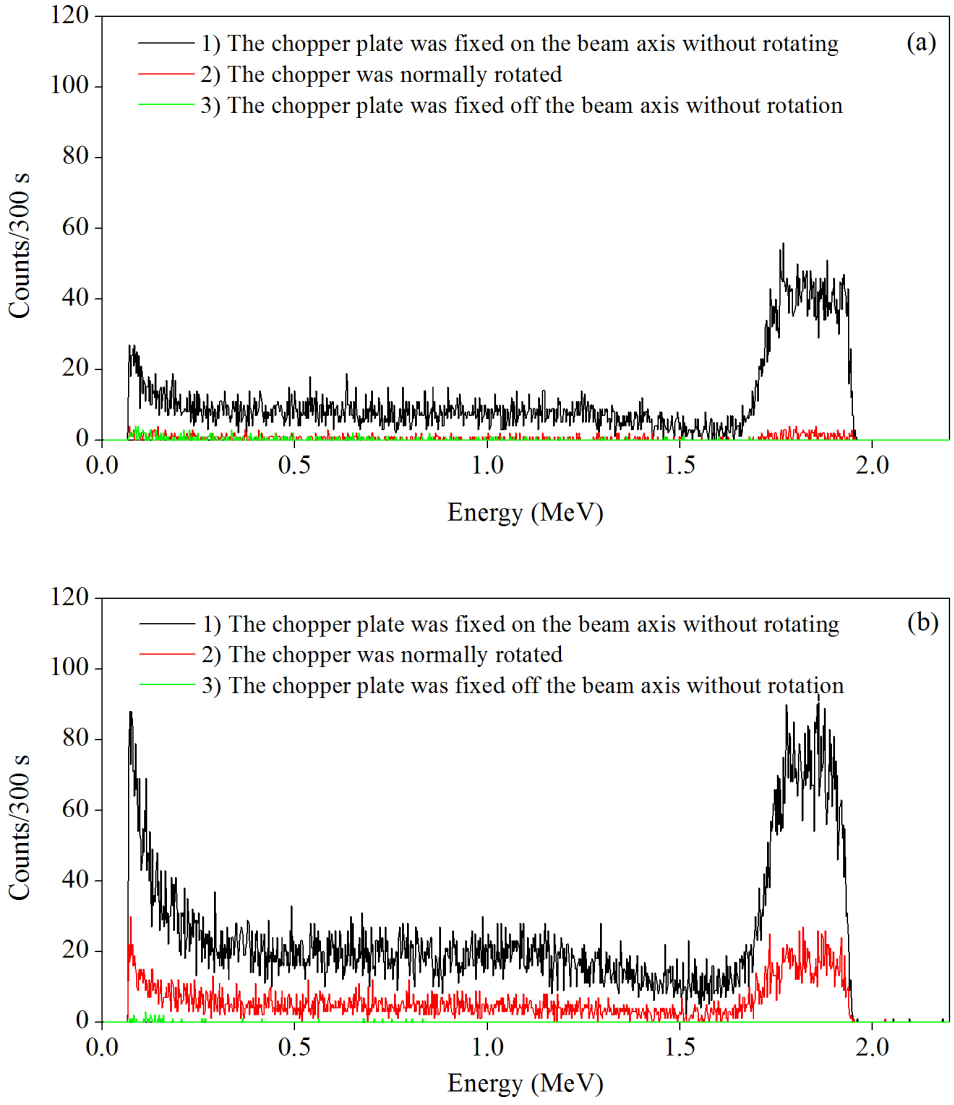

Fig. 4.14 Spectra of scattered proton from a rotating beam chopper at (a) 4% and (b) 25% of the incident beam was chopped

When the beam chopper was operated, the count rate of the gold peak in the case of 4% beam-chopping ratio was only around 30 count/min, which was not enough to achieve adequate statistical accuracy within typical beam irradiation time (~5 min). Thus, to increase the RBS count rate, the beam-chopping ratio was increased up to 25% by increasing the area of the gold foils (Fig. 4.14b). An RBS count rate of about 400 count/min was obtained.

From the energy spectra in the case 3, the counts due to the protons backscattered by the other components in the chamber were negligible. This result ensures that the RBS count is proportional to the amount of protons incident to the target.

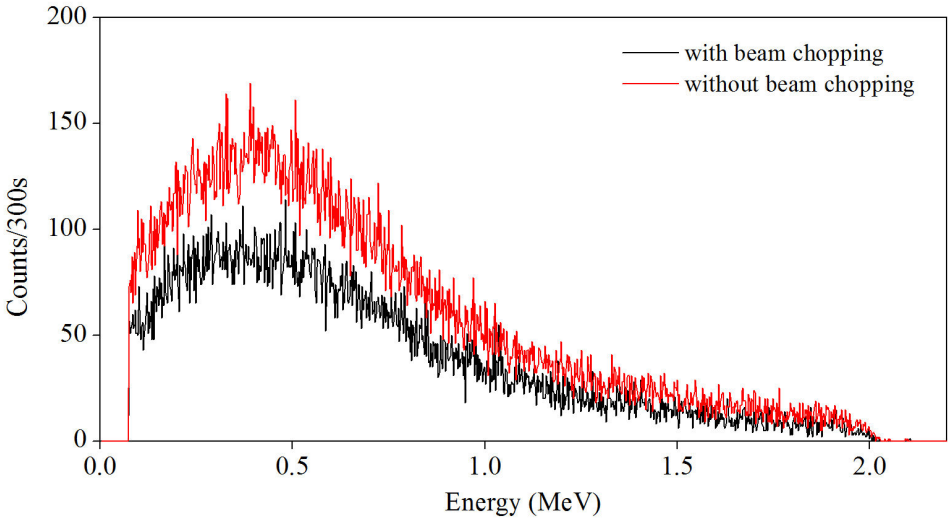

Fig. 4.15 Comparison of energy spectra of forward-scattered protons measured with and without beam chopping

To check the unwanted effect of the beam chopping on the measurement of protons that are forward-scattered by the flat glass target, proton energy spectra were measured with and without beam chopping and compared in Fig 4.15. Although the total count of the scattered proton was decreased by 33% owing to the beam chopping, the spectrum shape well coincide each other, which supports that the developed beam-sampling system caused no unwanted effect on the proton scattering by the flat glass target located downstream.

From the above results, we concluded that the normalization based on the RBS measurement would be the most reliable, and applied it to the data processing of the results given below.

4.3.2 Effect of surface roughness on the beam transport

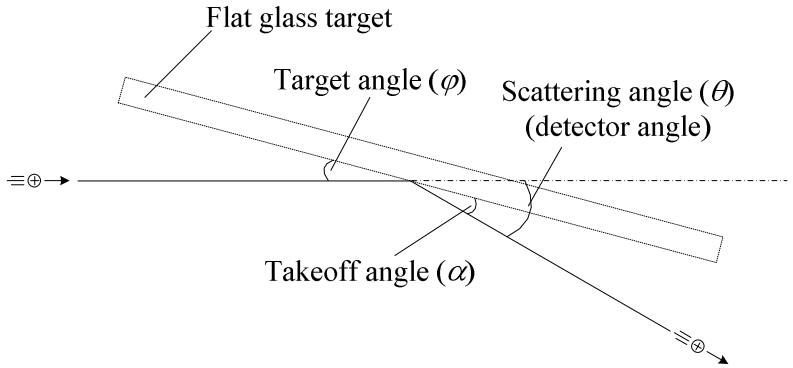

Fig. 4.16 Schematic shows the definition of the angle

To examine the effect of wall surface roughness on the beam transport through the tapered capillary, energy spectra of protons scattered by flat glass targets having different surface roughnesses were examined based on the geometry illustrated in Fig. 4.16. Figure 4.17 shows the energy spectra of protons scattered by the flat glass #1 that has a maximum peak to valley deviation of 0.6 μm. In this measurement, the target angle was varied from 1 to 3 degrees. At each target angle, the energy spectra were measured by changing the detector angle, which is equal to the scattering angle, as shown in the figures. Figure 4.18 shows the energy spectra of protons scattered by the flat glass #2 (0.03 μm), which were measured with the same setup as for the flat glass #1. The energy spectra were normalized by the count of backscattered protons measured by the beam-sampling system.

The results in Fig. 4.17(a) show that the total amount of the scattered protons decreases with increasing the scattering angle, which is due to the rapid decrease in the scattering cross section with increasing scattering angle. On the other hand, the peak of the energy spectrum shifts towards low-energy side with increasing scattering angle. The reason why the spectrum has a peak is probably explained as follows. The final energies of the detected protons are predominantly determined by the electronic energy loss of the protons in the target (the nuclear energy loss is negligibly small for glancing angle scattering). Because the scattering cross section increases with

decreasing projectile energy (see. Eq. 2.2), the spectral intensity is predicted to increase monotonically with decreasing proton energy if we assume that the proton incident to the target experience only single scattering event. However, the multiple scattering becomes more probable as the proton travels longer distance and suffers larger energy loss in the target, which deflects the flight direction of the scattered proton and prevents it from being detected. This effect probably reduces the spectral intensity in the low-energy side, forming a peak in the spectrum. When the scattering angle increases, the proton path length after the first scattering decreases, which makes the effect of the multiple scattering relatively small. Thus, the peak in the spectrum shifts towards low-energy side with scattering angle.

To examine the effect of the target surface roughness on the beam transport based on scattering phenomena, the proton energy spectra measured for two different surface roughnesses were compared in Fig. 4.19 for target angles from 1º to 3º. The figures show that the amount of scattered protons by the flat glass #2 was slightly larger than that by the flat glass #1 in every case, indicating that the surface roughness might reduce the probability of proton scattering by the glass target.

Figure 4.20 compares the energy spectra for scattering angles of 1-3º with a fixed target angle of 1º. In these figures, the amount intensity of scattered proton by flat glass #2 was also slightly larger than that for the flat glass #1. These results indicate that the intensity of scattered protons increases with increasing the smoothness of the surface.

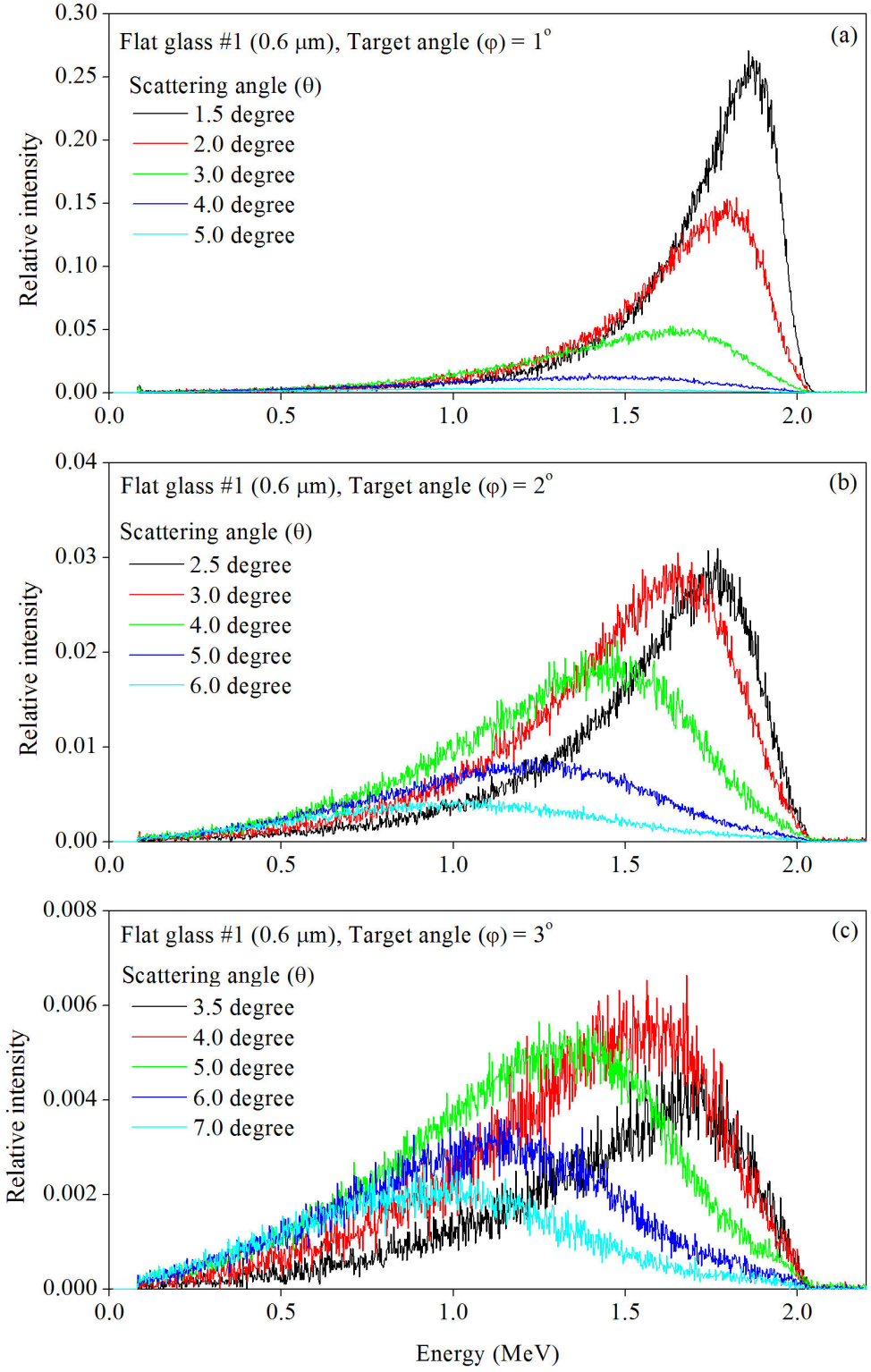

Fig. 4.17 Energy spectra of protons scattered by flat glass #1 with target angles of (a) 1°, (b) 2°, and (c) 3°.

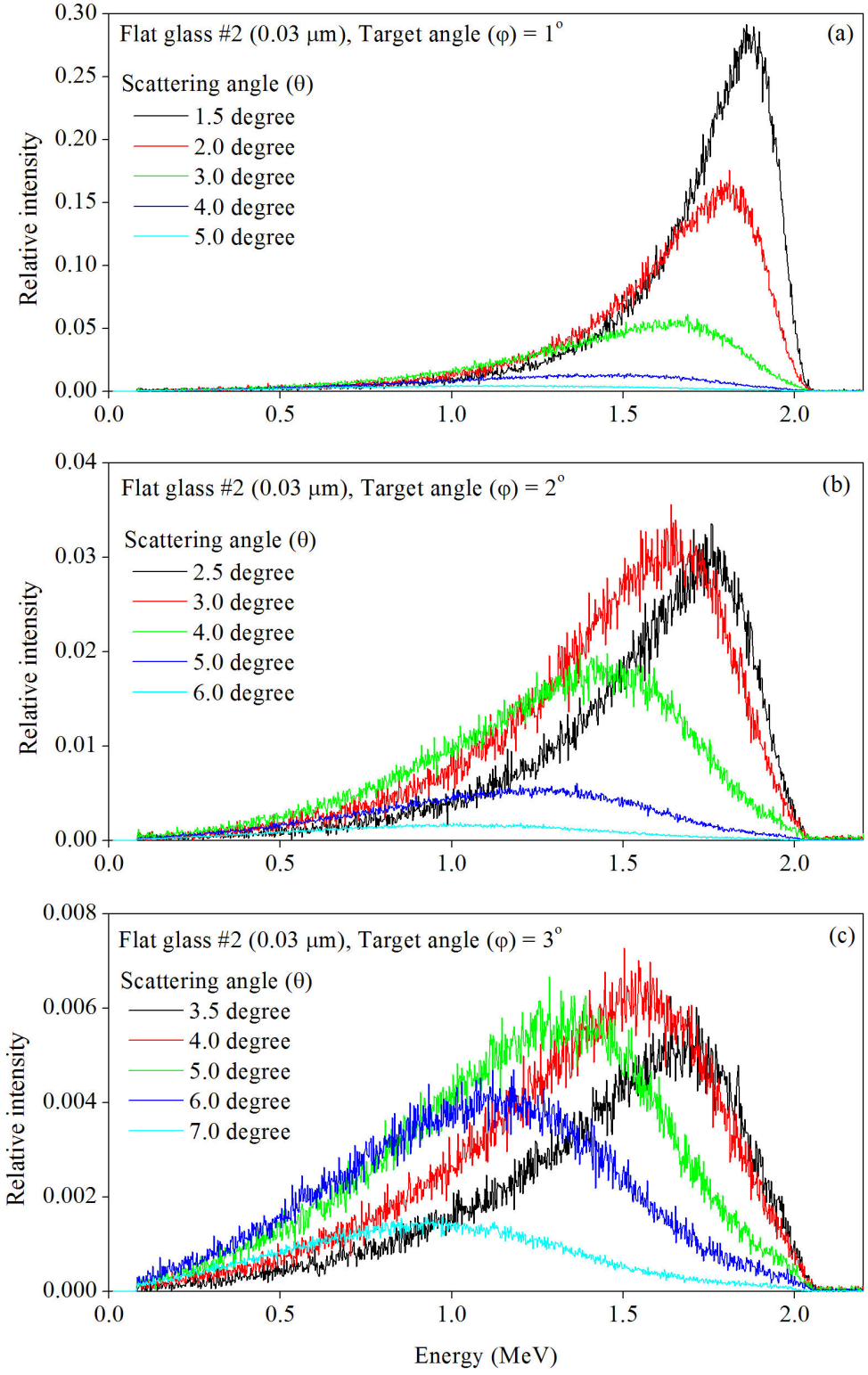

Fig. 4.18 Energy spectra of protons scattered by flat glass #2 with target angles of (a) 1°, (b) 2°, and (c) 3°.

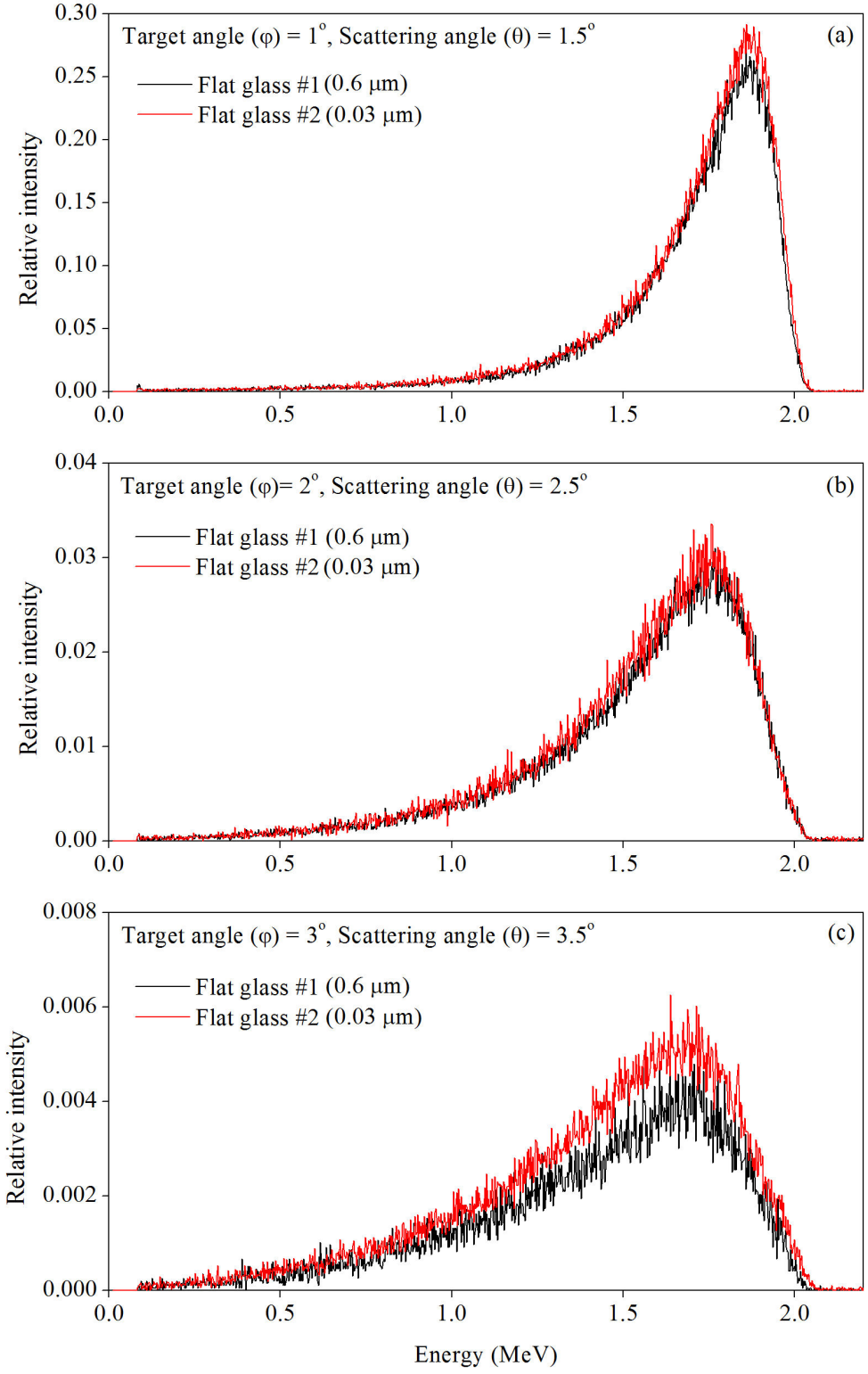

Fig. 4.19 Comparison of energy spectra between protons scattered by flat glass target #1 and those by flat glass target #2. Target angles are (a) 1°, (b) 2°, and (d) 3°. Takeoff angle is fixed to be 0.5°.

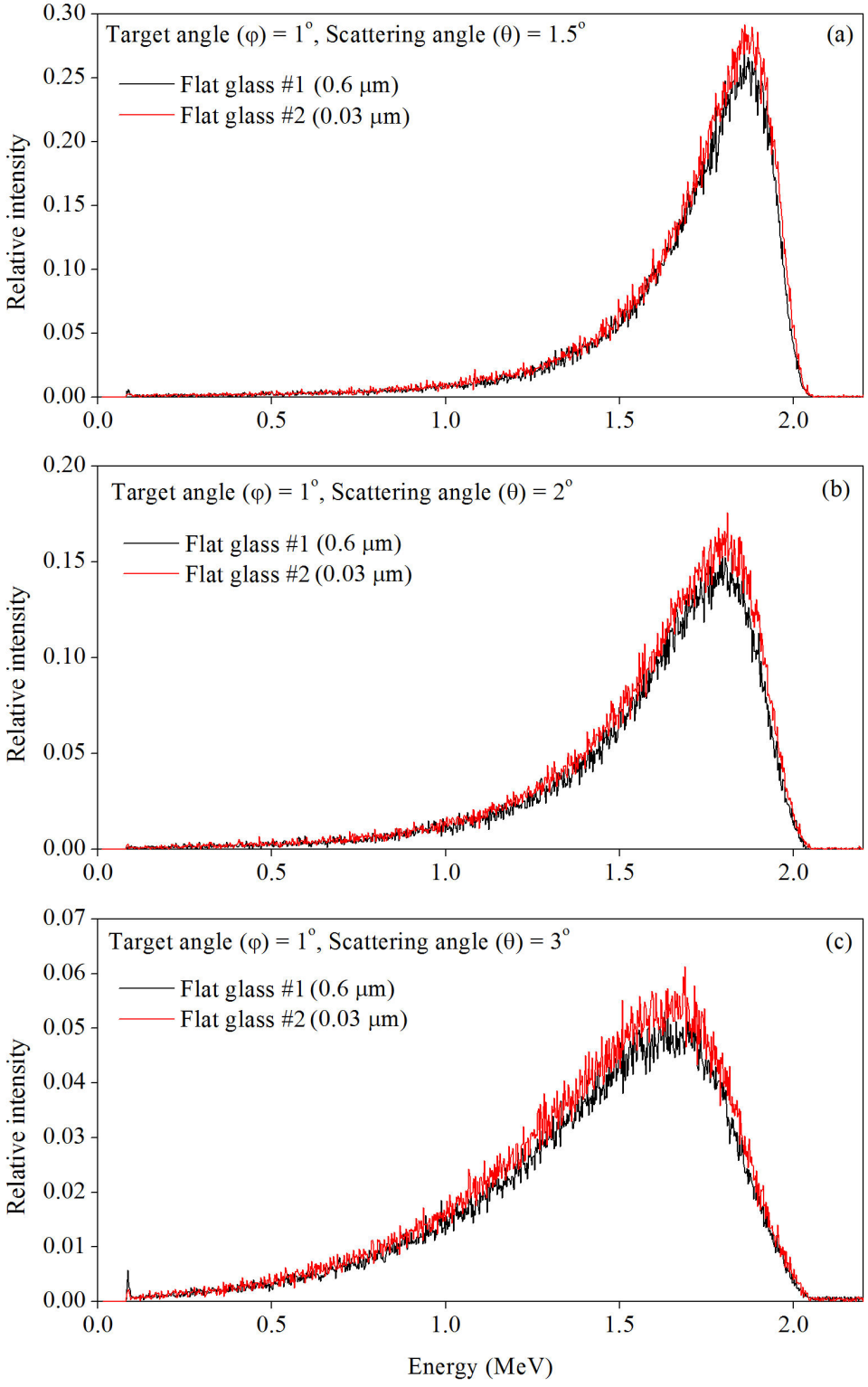

Fig. 4.20 Comparison the energy spectra of protons scattered by target #1 and those by target #2 with scattering angles of (a) 1.5º, (b) 2º, and (c) 3º. Target angle is fixed to be 1º.

4.4. micro-PIXE analysis of archaeological samples

4.4.1 Performance of the micro-PIXE system

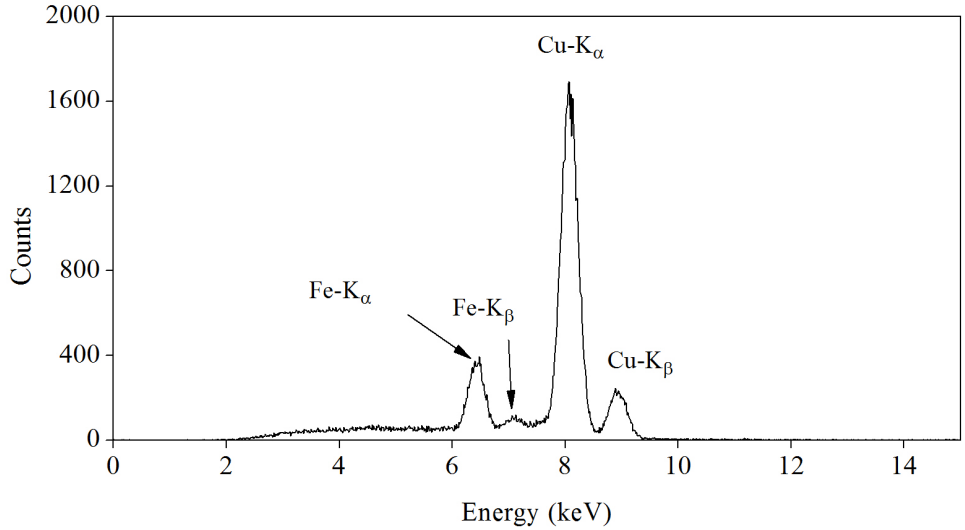

Fig. 4.21 A typical X-ray spectrum measured for a copper plate target

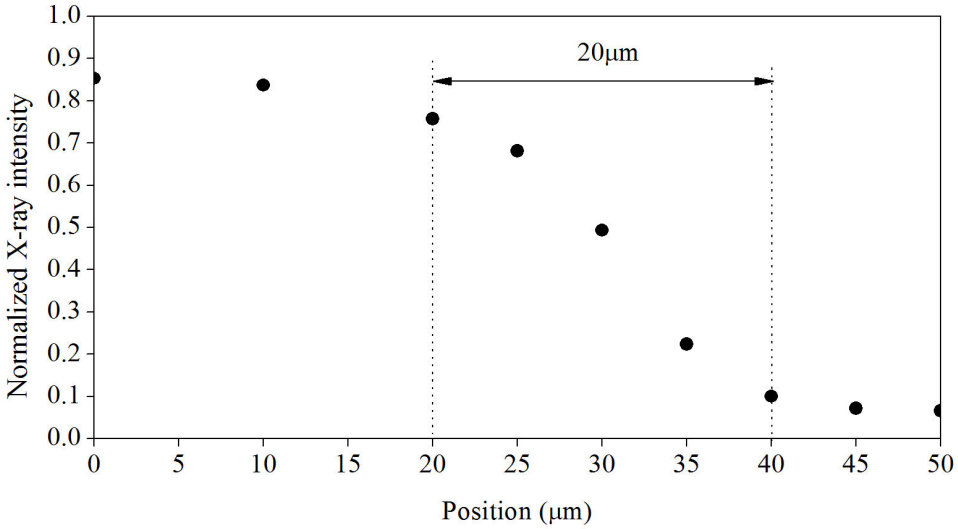

Fig. 4.22 A Cu-K X-ray intensity profile measured at the edge of the copper plate

A typical X-ray spectrum obtained in the copper plate measurement is shown in Fig. 4.21. We found not only Cu peaks but also Fe peaks, which probably come from the stainless steel of the chamber wall bombarded by backscattered protons. In Fig. 4.22, the count of Cu-K_α and Cu-K_β lines are plotted as a function of the beam position. These X-ray counts were normalized by the total RBS count measured by

the silicon detector. This result shows that the effective beam diameter roughly evaluated from the highest and the lowest X-ray intensities was around 20 μm. This result indicates that the halo component, which has relatively large divergence angle, probably degrades the spatial resolution of the measurement.

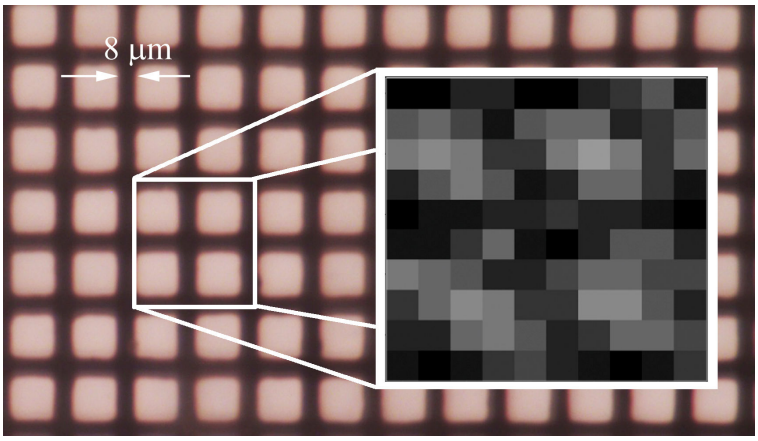

Fig. 4.23 A magnified photograph of copper fine mesh and a copper distribution reconstructed from the Cu-K X-ray intensities

Figure 4.23 shows a magnified photograph of the copper fine mesh and a two-dimensional distribution of cupper reconstructed from the observed Cu-K X-ray intensities. In the element mapping, the beam current from the capillary was around 0.1 nA and the measurement time was 30 s for each beam position. By using a step size (5 μm) smaller than the beam spot size, thin copper wires (~8 μm) were resolved in the reconstructed image even though the effective beam spot size (~20 μm) is much larger than the wire width.

4.4.2 Elemental composition of the archaeological sample measured using a 500-μm-diameter beam

For the energy calibration of the measurement system, a small stainless steel plate was put on the sample holder and irradiated by 2-MeV protons. The measured PIXE spectrum is shown in Fig 4.24. From this result, we found the X-ray peaks of Cr-K_α, Cr-K_β, Fe-K_α, Fe-K_β, Ni-K_α, and Ni-K_β, whose energies are 5.411keV, 5.946keV, 6.398keV, 7.057keV, 7.847keV, and 8.263keV, respectively. These data were used for the energy calibration of the system.

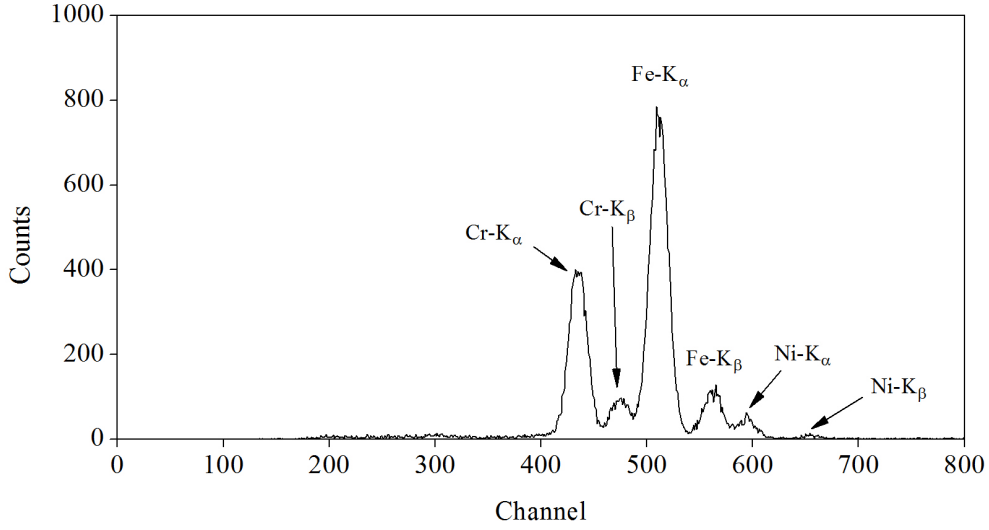

Fig. 4.24 PIXE spectrum of the stainless steel sample for calibration

After the calibration, the sample holder was moved in the vertical direction so that the beam could hit the pottery sample. Then, the cross section of the sample was irradiated at the surface layer and the substrate. Figure 4.25 shows the measured PIXE spectra of (a) the surface layer and (b) the substrate, which were obtained using a 500-μm-diameter beam prepared simply by apertures. We see that the both regions contain Si, K, Ca, Ti, Mn, and Fe. Howerver, the ratios of X-ray intensities for these elements are different between the surface layer and the substrate. The highest X-ray peak appears at Ca-K_α for the surface layer and K-K_α for the substrate. Then, the cross section of the pottery sample was scanned with a 500-μm step from the surface layer to the substrate. The intensity of Ca-K_α changed drastically with the beam position as shown in Fig. 4.25. These results indicate that the surface layer contains a large amount of Ca. In this measurement, the spatial resolution was not high enough to separately measure the elemental compositions of the sub-layers of the surface layer, such as the glaze and the paint layers, whose typical thickness is around 200 μm. The spatial distributions of the elements in these layers should be examined in detail by a microbeam with a diameter much less than the thickness of each layer.

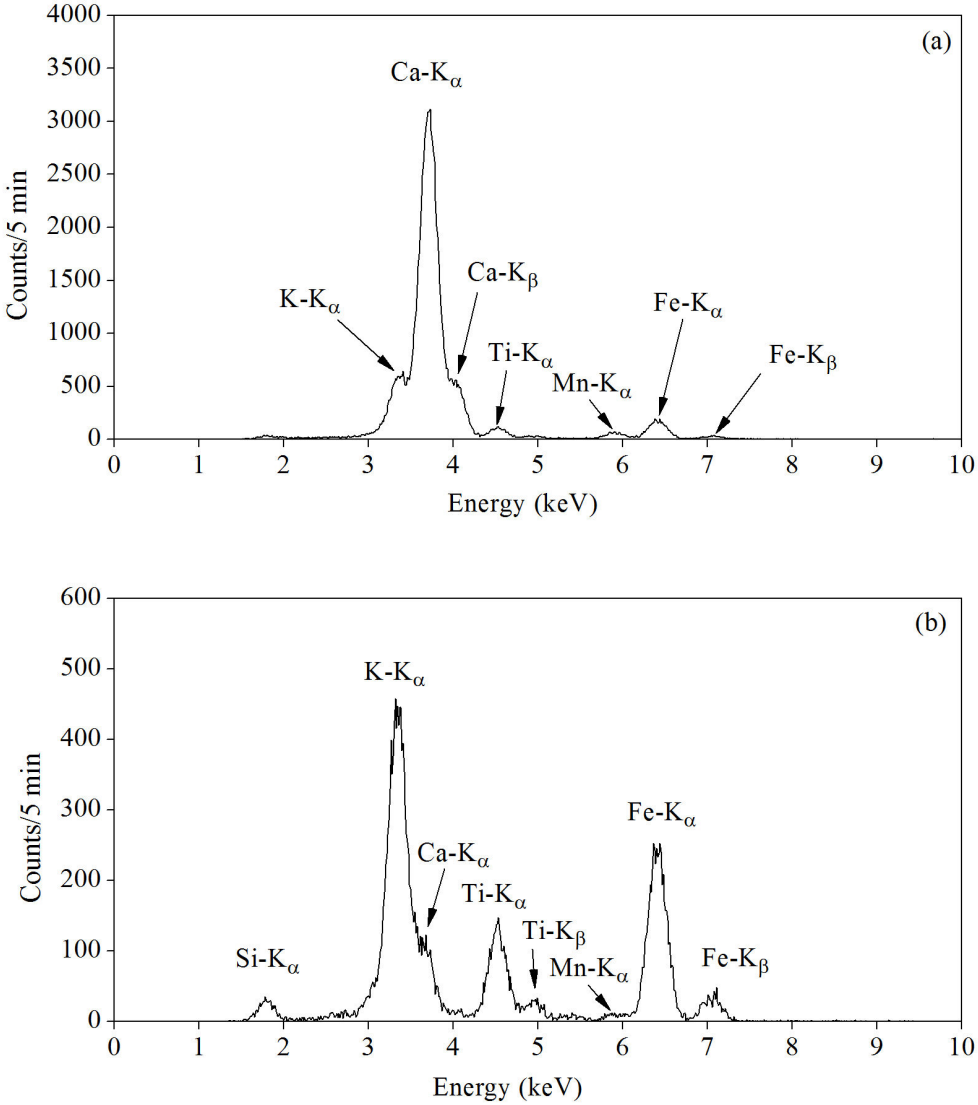

Fig. 4.25 PIXE spectrum of (a) the surface and (b) the substrate of the old Sangkhalok irradiated by 500-μm-diameter beam

4.4.3 PIXE analysis of glass tubes

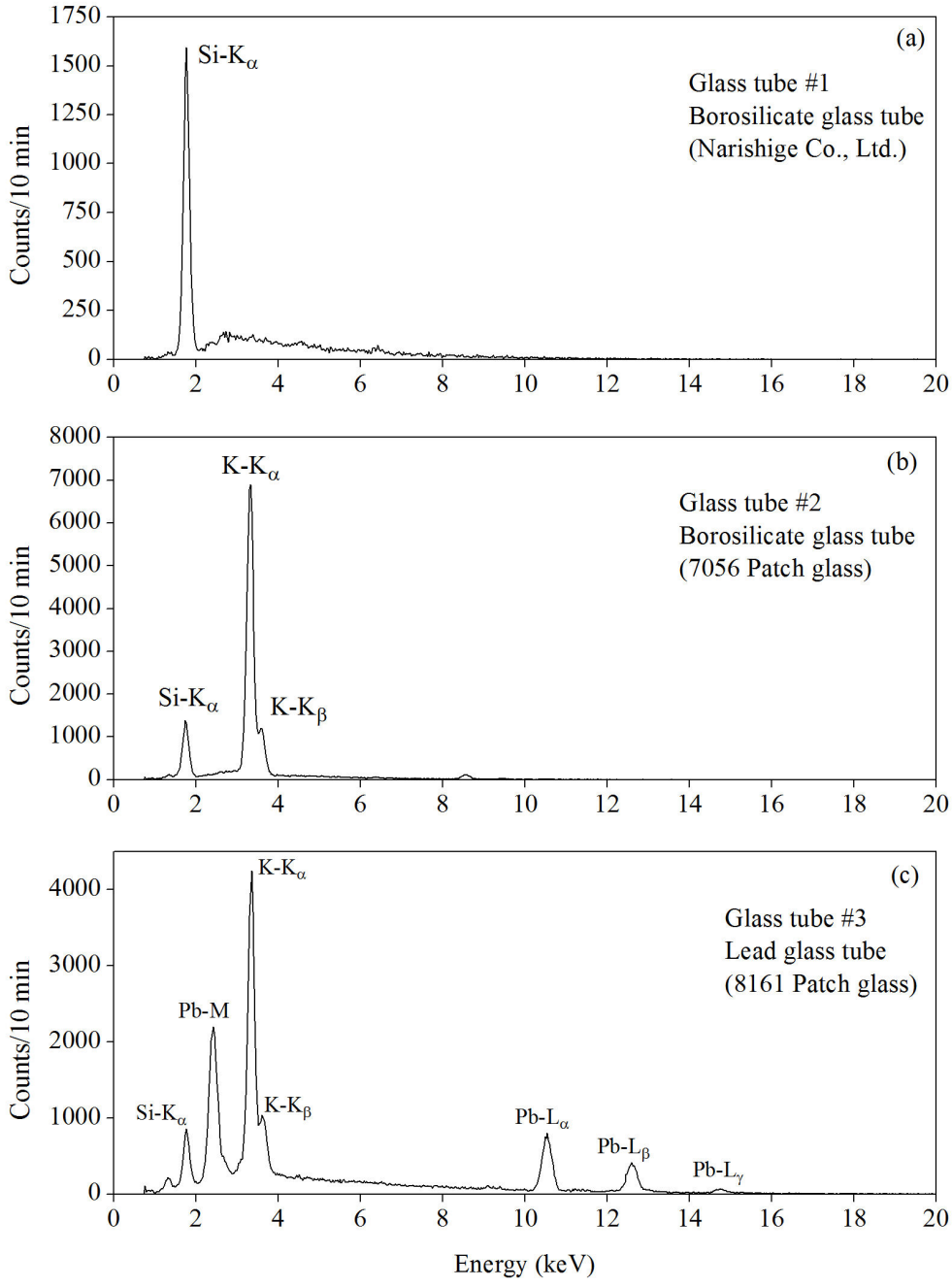

Fig. 4.26 PIXE spectra of (a) borosilicate glass (Narishige Co., Ltd.), (b) borosilicate glass (7056 Patch glass), and (c) lead glass (8161 Patch glass)

Figure 4.26 shows PIXE spectra measured for three different glass tubes listed in Table 3.1. For the glass tube #1 (borosilicate glass), we see only a large peak of Si-K_α. The other elements were not detected by this system because they are light ($Z < 13$) elements for which the sensitivity of PIXE analysis is low. Figure 4.26b shows the PIXE spectrum of the glass tube #2. The material is also borosilicate glass as in the case of the glass tube #1, but has a different chemical composition. It contains K, so that we see the peaks of K-K_α and K-K_β in addition to Si-K_α. The PIXE spectrum of glass tube #3 is shown in Fig 4.26c. This spectrum contains the peaks of Si-K_α, K-K_α, K-K_β, Pb-L_α, Pb-L_β, Pb-L_γ and Pb-M. The L-series and M-series of Pb X-ray were found because the material of this tube is lead glass.

According to the PIXE spectra for three types of glass tubes, the suitable glass tube for micro-PIXE analysis is the borosilicate glass tube #1 because the X-ray spectrum of this glass tube contains only Si-K_α peak and the background X-ray from this glass tube can be lower than that from the other glass tubes containing K and Pb. Note that when the range of protons in the borosilicate glass is smaller than the wall thickness of the tapered capillary near the tip, the protons cannot pass through the capillary wall and the Si X-ray produced inside the capillary wall can be attenuated by the borosilicate glass itself.

4.4.4 micro-PIXE spectrum of the old Sangkhalok

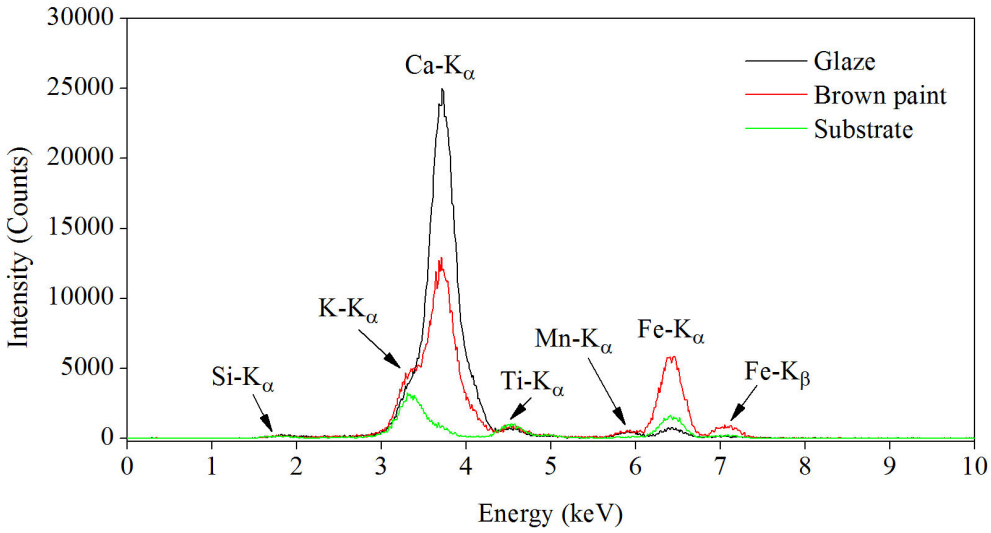

Fig. 4.27 PIXE spectra from the cross section of the old Sangkhalok at glaze, brown paint, and substrate

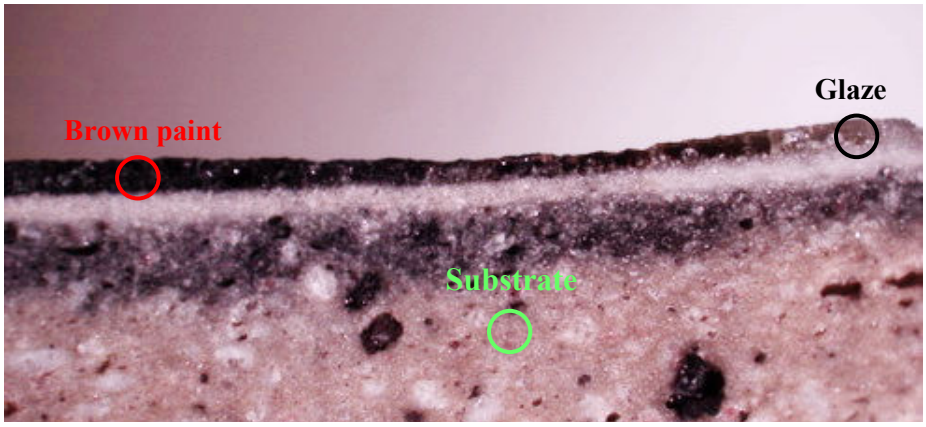

Fig. 4.28 Beam positions on the cross section of the old Sangkhalok. Circles indicate the beam sizes

Typical X-ray spectra obtained from the cross section of the old Sangkhalok sample are shown in Fig. 4.27. A 2-MeV proton beam was used and the outlet diameter of the tapered glass capillary was 70 μm. The beam current at the capillary outlet was around 0.3 nA. The X-ray counts were normalized by the scattered proton counts measured by a Si charged-particle detector. The cross section was irradiated at three different positions of the beam spot, on the brown paint layer, the glaze layer,

and the substrate, as shown in Fig. 4.28. The measured spectra show that the intensity of Ca-K_α for the glaze layer was roughly two times larger than that for the brown layer. On the other hand, the intensity of Fe-K_α for the brown layer is much higher than that for the glaze layer, whereas that for the substrate is a bit higher than that for the glaze layer. These results indicate that the glaze layer contains a large amount of Ca compounds and the brown layer also contains less amount of it. Thus, the brown layer can be regarded to be a mixture of brown paint and glaze. Moreover, we see that the brown layer contains a lot of Fe, which is consistent with the fact that the brown color is made of rust.

4.4.5 Depth profile of the elemental distribution on cross section of the old Sangkhalok

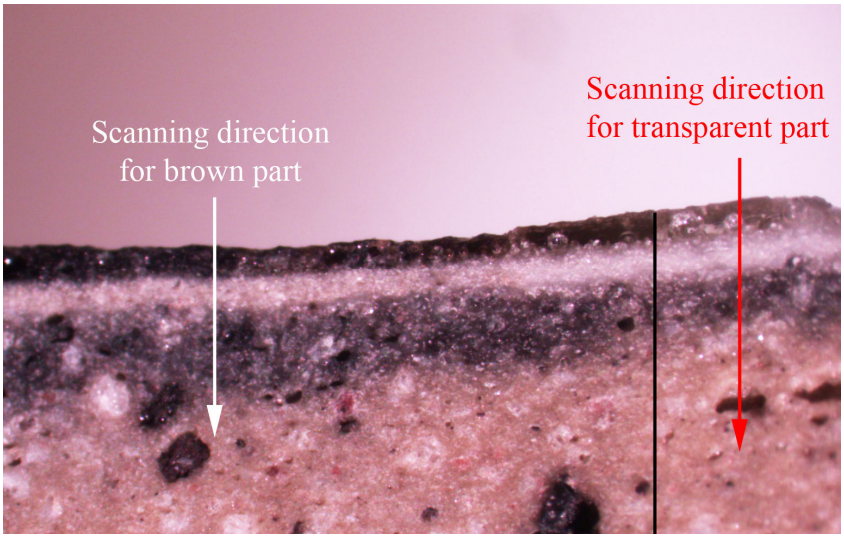

Fig. 4.29 The scanning direction on the cross section of the old Sangkhalok

To investigate the elemental distribution in the old Sangkhalok sample, the cross section was irradiated by 2-MeV protons focused by the tapered glass capillary. The sample was scanned from the surface to the substrate with a 70-μm step. The beam current at the capillary outlet was around 0.3 nA and the measurement time was 5 minutes for each position. Depth profiles of the brown part and the transparent part were investigated. The scanning directions are shown by arrows in Fig. 4.29.

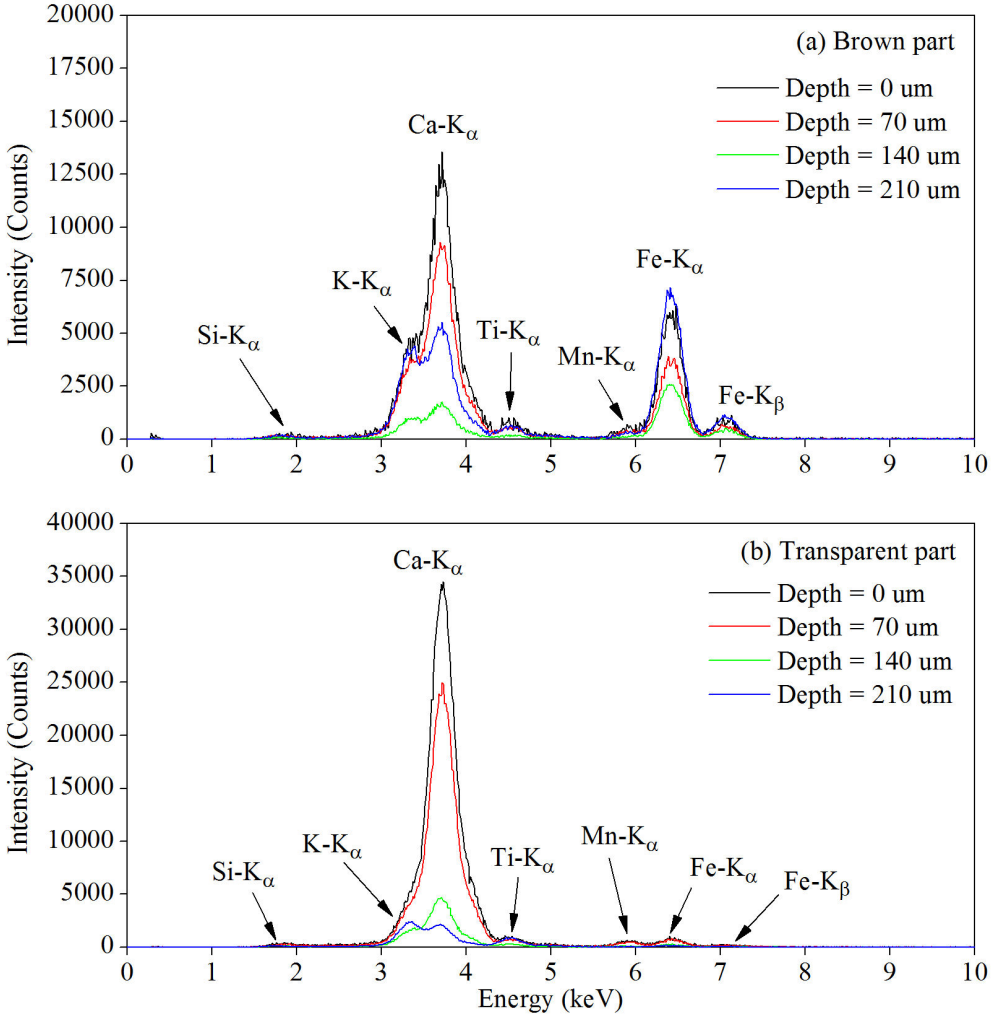

Fig. 4.30 PIXE spectra of the old Sangkhalok at (a) the brown part and (b) the transparent part

Typical spectra for the brown section and the glaze section with different scanning positions are given in Fig. 4.30. By using the step size smaller than the thickness of each layer, the elemental distribution on the cross section near the surface could be investigated. The spectra for the brown section (Fig. 4.30a) show that the X-ray intensities of some elements such as Ca and Fe largely change with depth. However, the dependence of the Ca concentration on the depth was not simple. For example, the Ca concentration at a depth of 210 µm was higher than that at 140-µm. This result is due to the fact that the concentration of elements was not homogeneous and the measurement was performed by only one-line scanning. Figure 4.30b shows the PIXE spectra on the transparent part. From these results, we found that the

intensity of Ca-K_α changes with depth similarly as in the case of the brown part, whereas the intensity of Fe-K_α does not change clearly, and is lower than that of the brown part. These results confirm that the glaze layer contains a large amount of Ca and the brown layer is a mixture of the brown paint and the glaze.

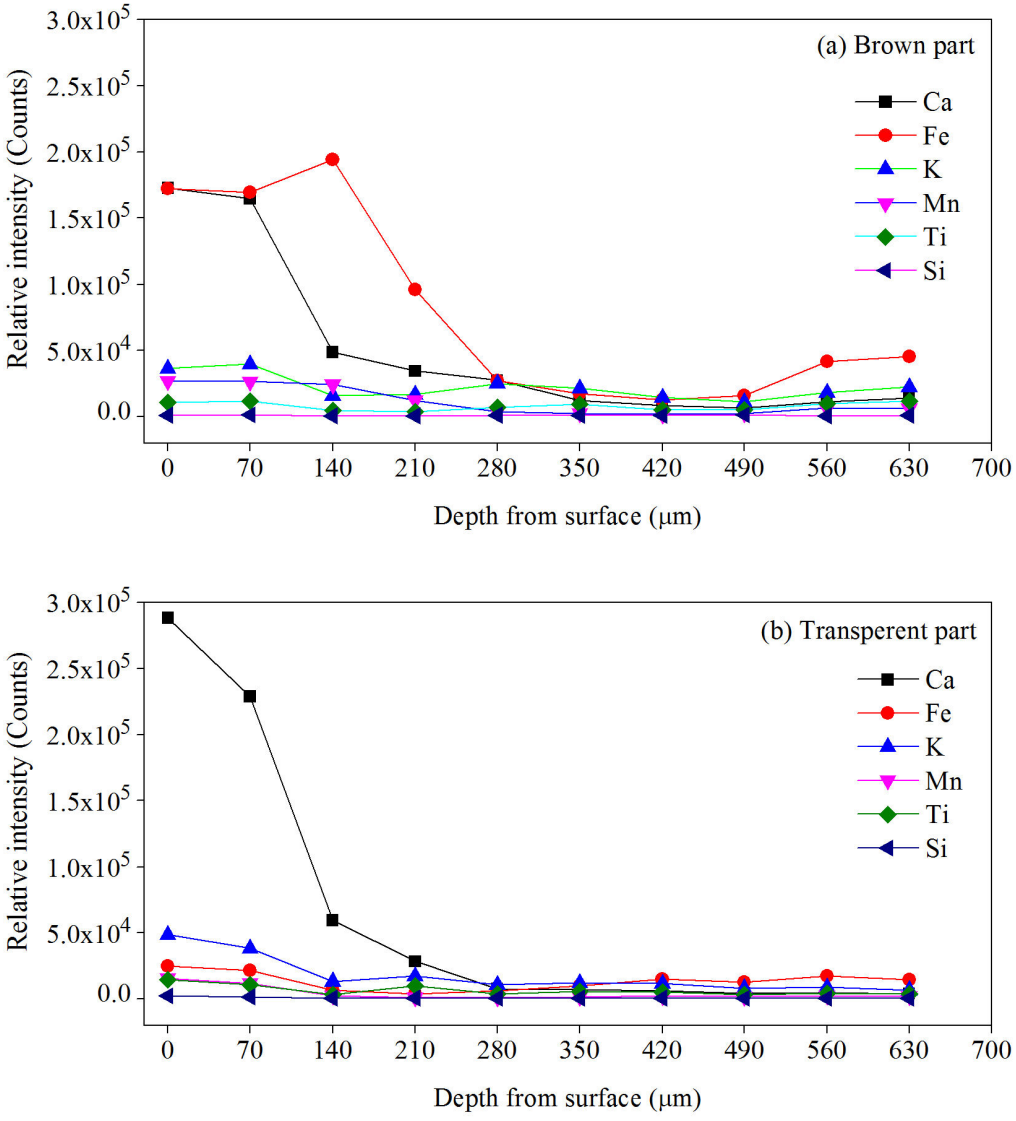

Fig. 4.31 Intensity distributions of elements as a function of depth on the cross section of (a) the brown part and (b) the transparent part of the old Sangkhalok

To improve the measurement of the elemental distribution, X-ray intensity distributions along the other scanning lines were measured and the X-ray intensity at each depth was evaluated by averaging the intensities measured at the same depth. Because the X-ray production cross section by proton bombardment is different for different elements and the X-ray detection efficiency depends on the X-ray energy, the X-ray intensity for each element was normalized by the X-ray production cross sections for 2 MeV protons and the detector efficiency data before comparing the elemental concentration. Figure 4.31 shows the distribution of each element on the cross section of the brown part and the transparent part. For the brown part, the intensity of Ca is high on the surface layer and rapidly decreases at a depth of around 100 μm. On the other hand, the intensity of Fe increased at a depth of 140 μm. After that, the intensity of Fe decreased from a depth of 140 μm to 280 μm. This result indicates that the Fe compounds diffused from the brown paint layer to the glaze on the surface. The diffusion process probably occurred during the thermal process of the pottery production. For the transparent part, the concentration of Ca was larger than that in the brown part almost by a factor of two because this part was not diluted by the brown paint.

4.4.6 Two-dimensional element distribution of the old Sangkhalok

To demonstrate the two-dimensional element mapping, the cross section of the old Sangkhalok sample having a brown layer on the surface was scanned by a capillary-focused microbeam. The step size was 70 μm and the scanned area was 630 μm × 930 μm. The beam current at the capillary outlet was around 0.3 nA and the measurement time was 5 min for each position. From the intensity of K X-ray of each element at each position, the elemental distributions were reconstructed as shown in Fig. 4.32. Figure 4.32a shows the two-dimensional distribution of Ca on the cross section. This result shows that the glaze layer contains a large amount of calcium. Fig. 4.32b, we see that this sample contains a large amount of Fe near the surface layer and the Fe concentration gradually decreases to the surface coated with glaze. This result indicates that the Fe compounds diffused from the paint layer to the glaze layer. The intensity of Fe-K_α gradually increased again in the substrate. This Fe can be attributed to the Fe that originally exists in the body of the sample because Fe is known as one of the major elements contained in clay. Figures 4.32c, d, e, and f show

the distributions of K, Mn, Ti, and Si, respectively. Although two-dimensional images of these elements have no specific clear distribution pattern, these images indicate that the layer near the surface contains K and Mn compounds. Also Ti-rich and Si-rich particles are found everywhere on the cross section.

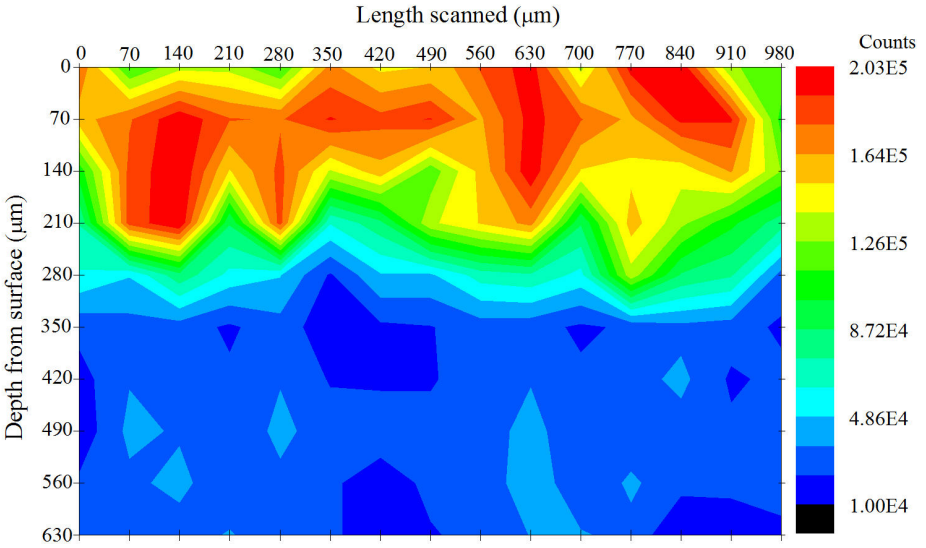

(a) Ca

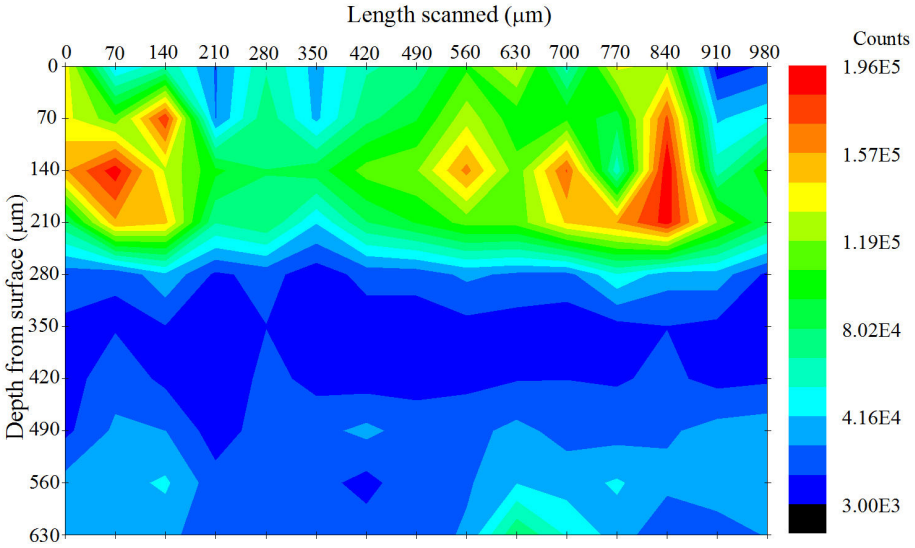

(b) Fe

Fig. 4.32 Two-dimensional element distributions of (a) Ca, (b) Fe, (c) K, (d) Mn, (e) Ti, and (f) Si on the cross section of the old Sangkhalok

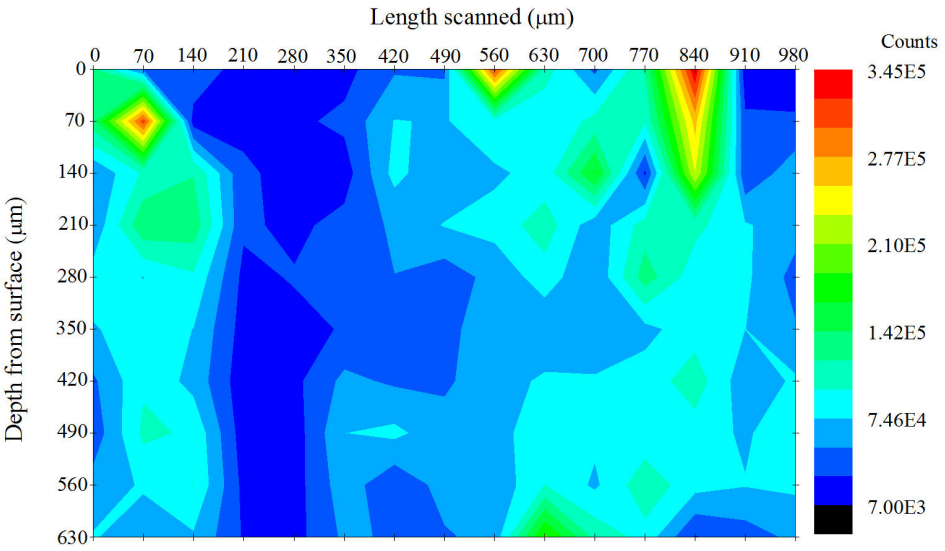

(c) K

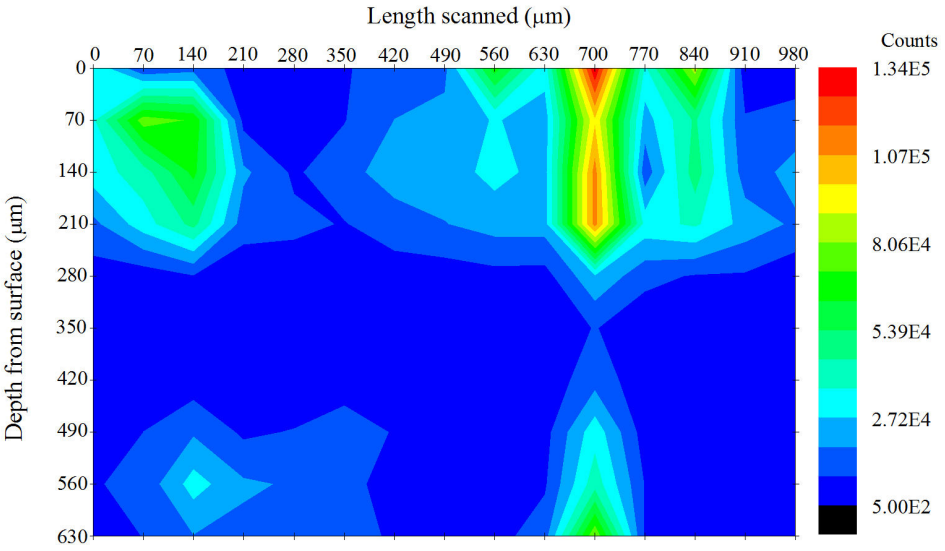

(d) Mn

Fig. 4.32 (continued)

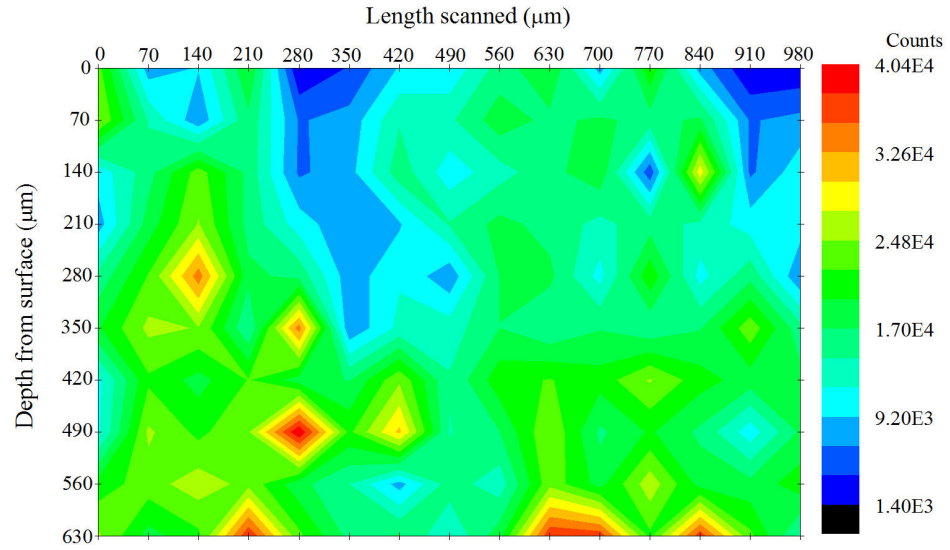

(e) Ti

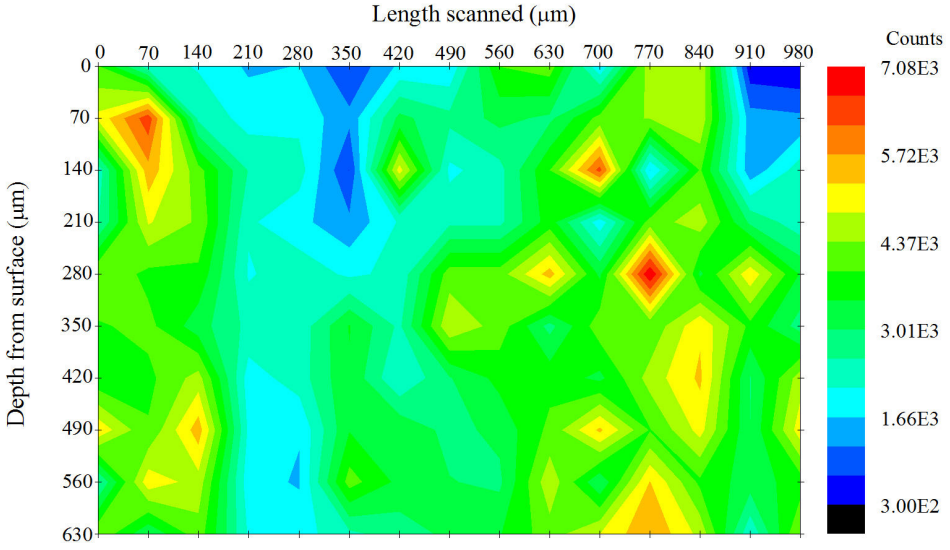

(f) Si

Fig. 4.32 (continued)

4.4.7 Comparison between the old and present pottery

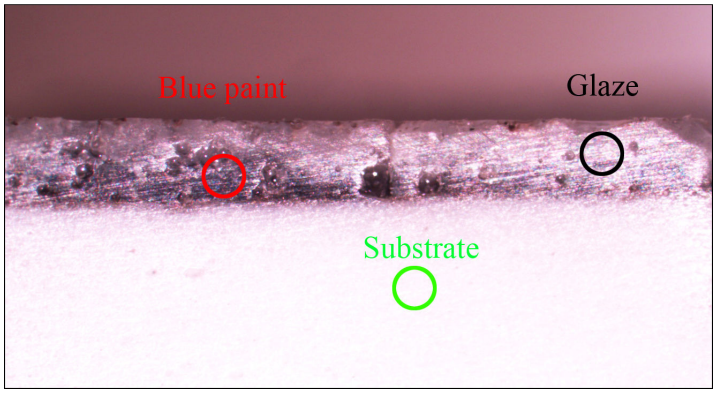

Fig. 4.33 Cross sectional photograph of the modern Sangkhalok with position where PIXE spectra were measured

The micro-PIXE spectrum on the cross section of the modern Sangkhalok sample was measured by the same system used for the old one. The cross section was irradiated at three different positions of beam spot (blue layer, glaze layer, and substrate) shown in Fig. 4.33. The measured PIXE spectra are shown in Fig. 4.34. In the case of the blue layer, Cr-K_α and Zn-K_α were found. Also for the glaze layer, Zn-K_α was found. However, Cr and Zn were not detected on the substrate.

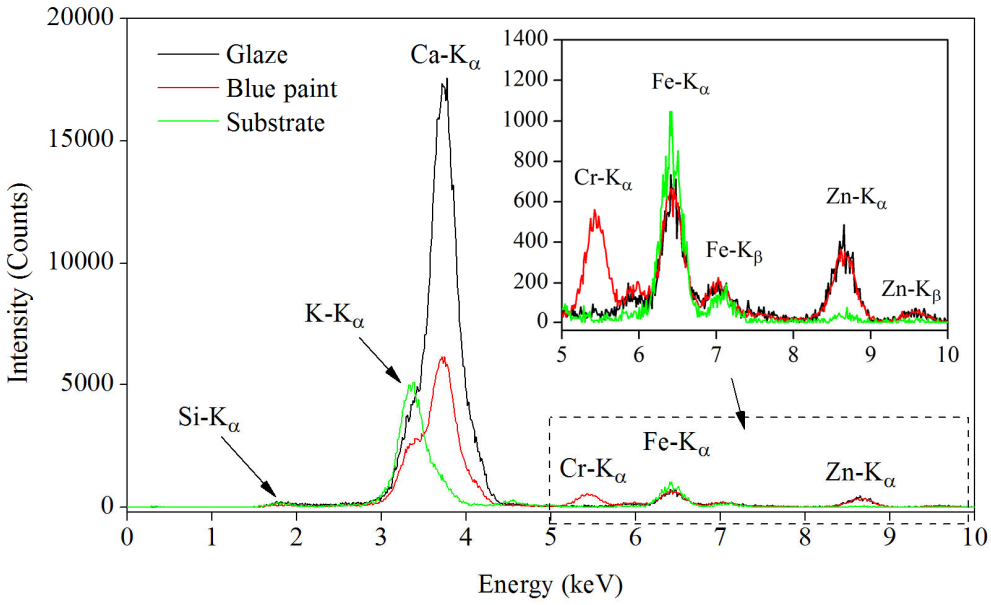

Fig. 4.34 PIXE spectra on the cross section of the modern Sangkhalok

To investigate the distribution of Cr, the cross section of the blue part was scanned from the surface to the substrate. The intensity of Cr-K_α as a function of depth is shown in Fig. 4.35. This result indicates that the blue paint with high concentration of Cr exists between the glaze layer and the substrate.

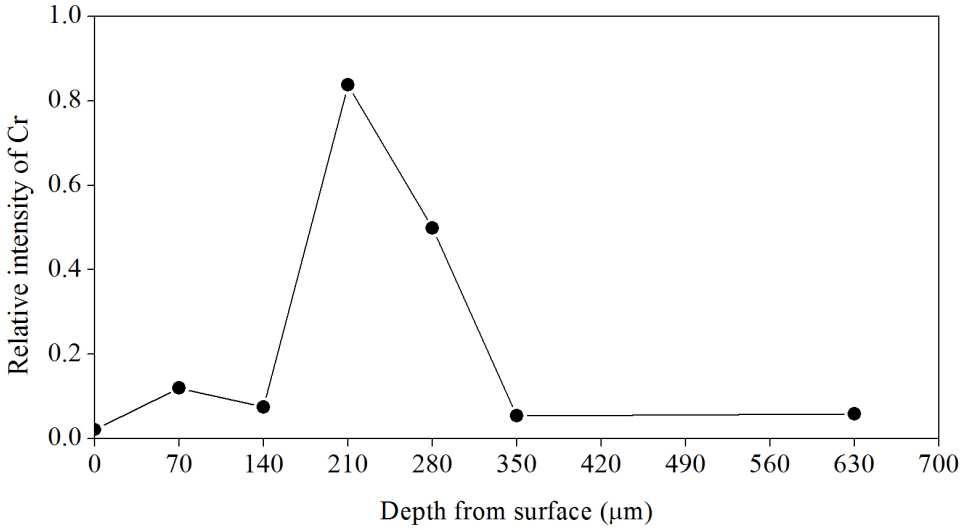

Fig. 4.35 The intensity distribution of Cr as a function of depth on the cross section of the modern Sangkhalok

From the result on the old and modern Sangkhalok, differences between these two samples can be summarized as follows. The glaze materials of both potteries contain a large amount of Ca, but Zn was found only in the modern one. As for the paint material, the brown layer of the old Sangkhalok contains Fe, but the blue layer of the modern one was rich in Cr. In the substrate, the main element was K for both samples. The structure of the surface layer was also different between the old and the modern potteries. On the surface layer of the old Sangkhalok, a mixing between the brown paint and the glaze was found, which is due probably to the diffusion of Fe from the brown paint to the glaze during the firing. On the other hand, in the modern Sangkhalok sample, the boundary between the blue paint and the glaze was clear. Thus, this finding might be useful to distinguish fake Sangkhalok potteries because the production technology for those fake potteries must be different from that for the old “real” Sangkhalok.

4.4.8 X-ray spectra of the potteries irradiated by proton and electron beam

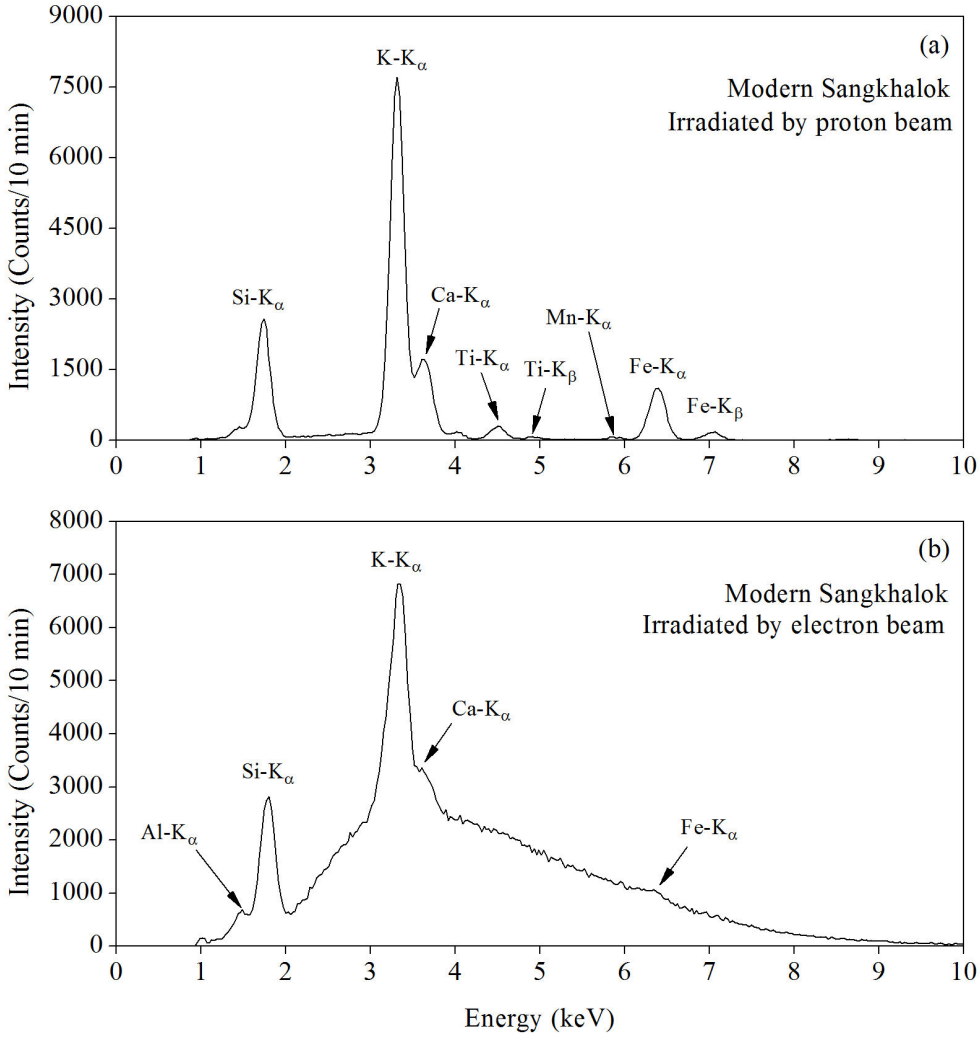

Fig. 4.36 X-ray spectra on the cross section of the modern Sangkhalok measured with (a) 2 MeV proton and (b) 15 keV electron microprobe

To emphasize the advantage of PIXE technique, the X-ray spectra were measured for the pottery irradiated by protons and electrons beam. This experiment was performed at the ED-PIXE chamber where an electron gun was attached (see Fig. 3.1). The X-ray spectrum from the sample could be measured by using the same detector by rotating the target by 90˚. In the case of proton beam, the proton energy was 2 MeV and the beam current at the target was around 1 nA. For the electron beam, the incident energy was 15 keV and the beam current was around 100 nA.

Figure 4.36 shows the X-ray spectra of the modern Sangkhalok irradiated by (a) the proton beam and (b) the electron beam. In this setup, the diameter of the electron beam was smaller than that for the proton beam, but the beam spot size could not be observed by using the polycrystalline-ruby beam-viewer. For this reason, we measured only the modern Sangkhalok sample, which has more homogeneous and fine grain structure. The X-ray spectrum obtained by electrons has high background noises, which come from the continuous X-ray (Bremsstrahlung) produced by the electrons. In Fig. 4.36b, we see that the sensitivity by the electron beam for high-Z element is much less than that for PIXE. The peaks of Ti and Mn K-Xrays could not be found on the X-ray spectrum irradiated by the electron beam not only because of the low intensities of these peaks but also of the strong background X-ray from Bremsstrahlung.

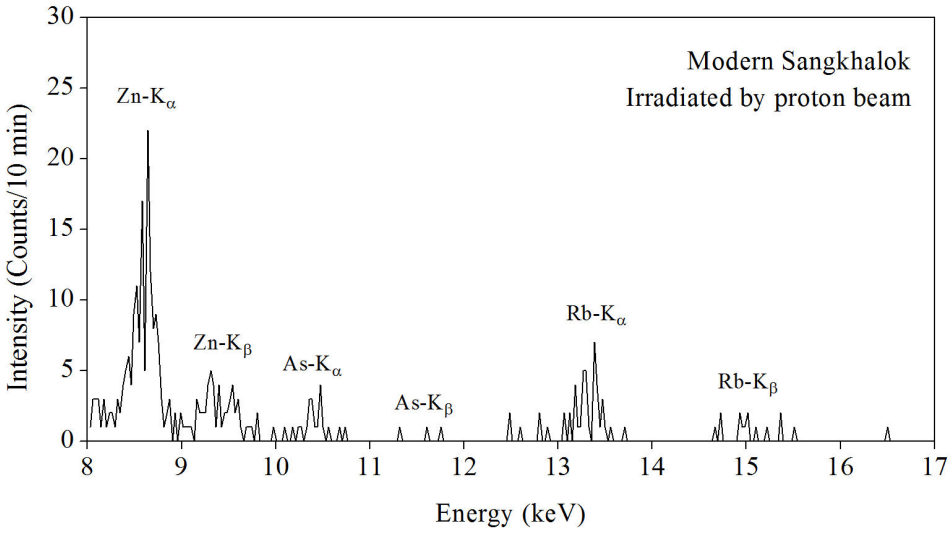

Fig. 4.37 Minor elements found on the cross section of the modern Sangkhalok

On the other hand, by using the PIXE analysis technique, even the minor elements in the modern Sangkhalok could be detected as shown in Fig. 4.37. The minor elements found in this sample are Zn, As, and Rb which are usually found in the earth crust. The above results indicate that the detection limit of the PIXE technique was much lower than that of the electron probe. This is the advantage of PIXE technique on the archaeology in which the identification of provenance of the samples is very important.

From these two spectra in Fig. 4.36, we found that the intensity of Si-K_α peak was higher than that obtained from the micro-PIXE system because the detector efficiency at low photon energy of the liquid-nitrogen cooled Si(Li) detector used in this measurement was higher than that of the Si-PIN detector used in the micro-PIXE system.

Chapter V
SUMMARY AND CONCLUSIONS

Chapter V describes the conclusions of this research, suggestion, and future studies. A list of publications and presentations related to this research is also given.

5.1 Conclusions

5.1.1 A technique to fabricate tapered borosilicate-glass and lead-glass capillaries having the same taper shape has been developed. The inner diameters of these capillaries were precisely measured and the axial symmetry of the capillary was checked by using a newly developed device dedicated to this purpose. The wall shapes and axial symmetries around the capillary tip were identical to each other, which was advantageous for the comparison between the beam-focusing abilities of these two capillaries.

5.1.2 The photostimulated luminescence (PSL) intensity distributions on imaging plates irradiated by proton beams focused by the tapered glass capillaries were investigated. The beam spot was found to consist of the core and halo components that are composed of the protons traveling straight through the capillary and those scattered by the capillary inner wall, respectively.

5.1.3 The energy spectra and the intensity distributions of protons focused by for borosilicate-glass and lead-glass capillaries were measured. Although the effective atomic number of the lead glass is approximately three times larger than that of the borosilicate glass, the observed enhancement in the beam-focusing ratio was much lower than expected from the dependence of the scattering cross section on the wall atomic number. This result suggests that the scattering cross section is not a dominant factor determining the transmission and the focusing of MeV protons in the tapered capillary.

5.1.4 The transmission of 2-MeV proton in the tapered capillary was numerically simulated by using an originally developed Monte Carlo (MC) code. In the case of the tapered capillary, the focusing ratios were evaluated to be 1.60 and 1.63 for the borosilicate-glass and the lead-glass capillary, respectively. On the other

hand, in the case of the conical capillary, the effective use of the capillary inner wall results in the focusing ratio being higher than that for the tapered capillary. However, the use of the conical capillary evidently makes the distribution of the halo component more diffusive because of its large taper angle. It was found that there is a trade-off between the beam-focusing ratio and the beam quality.

5.1.5 The MC simulation indicated that the escape distance plays an important role in the beam transmission through the capillary. Particularly, for the tapered glass capillary having a convex inner wall, the escape distance is relatively large and the probability of the scattered proton escaping from the wall reduces. The MC simulation predicted that when gold is used as the wall material, the use of the conical capillary improves the focusing ability by a factor of approximately 2. However, we must note that there is a trade-off between the focusing ratio and the beam quality. Therefore, to realize actual applications of the tapered capillary, the capillary wall shape should be carefully designed by taking this trade-off into account.

5.1.6 A novel beam-sampling system using a rotating beam chopper has been developed for the low-angle scattering experiments on the flat glass target. This device enabled us to monitor the incident proton current during the measurement. The beam-chopping ratio was increased to be 25% by increasing the area of the gold foils on the beam chopper to achieve adequate statistical accuracy within typical beam irradiation time. The energy spectra of protons scattered by the flat glass target were measured with and without beam chopping. Although the total count of the scattered proton was decreased by 33% owing to the beam chopping, the spectrum shape well coincide each other, showing that the developed beam-sampling system caused no unwanted effect on the proton scattering by the flat glass target.

5.1.7 The effect of inner wall surface roughness on the beam transport through the tapered capillary was examined by conducting beam-scattering experiments with flat glass targets having different surface roughness. The intensity of scattered protons increased with increasing the smoothness of the surface.

5.1.8 A compact micro-PIXE system using a tapered glass capillary for beam focusing has been developed. The performance of the system was examined experimentally and a two-dimensional element mapping was successfully demonstrated. When a target 1 mm downstream from the capillary outlet is irradiated

a proton micro beam from a ϕ10-μm capillary, its effective spot size was about 20 μm on the target. This is probably attributed to the halo particles having larger divergence angles.

5.1.9 The elemental composition of the old Sangkhalok was roughly determined by scanning the cross section of the pottery. The surface layer and the substrate were irradiated separately by a ϕ500-μm proton beam collimated by thin stainless steel apertures. The both regions contained Si, K, Ca, Ti, Mn, and Fe, but the X-ray intensities for these elements were different between the surface layer and the substrate. In this measurement, the spatial resolution was not high enough to separately examine the elemental compositions of sub-layers composing the surface layer.

5.1.10 The PIXE spectra of tapered glass capillaries made of three different glass materials were measured to examine the effect of X-rays emitted from the capillary itself on the micro-PIXE measurement. The borosilicate glass tube (#1 in Table 3.1) was found most suitable for PIXE analysis because the X-ray energy spectrum from this glass contains only a Si-K peak and the effect of this background X-ray on the PIXE spectrum is the lowest among the glass tubes examined.

5.1.11 The PIXE spectra of the old Sangkhalok were successfully obtained at three different positions (glaze, brown paint and substrate) on the cross section of the pottery by using ϕ70-μm capillary-focused proton beams. We found that the glaze layer contains a large amount of Ca. The brown paint layer contains Ca and Fe, which indicates a mixture of brown paint and glaze. The Fe compounds in the brown paint are consistent with the fact that the brown color is made of rust.

5.1.12 The elemental distributions of the old Sangkhalok sample were investigated by scanning the cross section from surface to substrate by a capillary-focused microbeam with a 70-μm step size. The result indicated that Fe diffused from the brown paint to the glaze. The diffusion process probably occurred during thermal process on the production. In the transparent part, the concentration of Ca was larger than that in the brown part almost by a factor of two, probably because this part was not diluted by the brown paint.

5.1.13 Two-dimensional distribution of elements on the cross section of the old Sangkhalok was successfully obtained. It should be noted that this is the world's first successful demonstration of the two-dimensional element mapping of archaeological samples by using a glass-capillary-focused proton microbeam. The 2-dimensional distribution images showed that the glaze layer contains a large amount of Ca and Fe that was probably diffused from the paint layer. The Fe concentration is remarkable also in the substrate. This Fe can be attributed to the Fe compounds that originally exist in the substrate because Fe is known as one of the major elements contained in clay. Although two-dimensional maps of K, Mn, Ti, and Si have no clear distribution pattern, they indicated that the layer near the surface contains K and Mn, and Ti-rich and Si-rich particles are found everywhere on the cross section.

5.1.14 The micro-PIXE analysis was conducted also for the cross section of the modern Sangkhalok by using the same system used for the old one. The glaze layer contained Zn and the blue paint layer contained Cr and Zn, which could not be found in the old Sangkhalok. The observed distribution of Cr on the cross section showed that Cr exist with a high concentration inside the blue layer near the boundary to the substrate. We found that the surface layer structure of the modern pottery was different from that of the old pottery. The old Sangkhalok has the diffusion of Fe from the paint layer into the glaze layer. On the other hand, the modern Sangkhalok has a clear boundary between the paint and the glaze layers. This difference might be useful to distinguish the fake Sangkhalok potteries because it was caused by the difference between the production technologies of the old and modern ages.

5.1.15 The X-ray spectra from the potteries irradiated by protons and electrons were measured to emphasize the advantage of the PIXE technique. The X-ray spectrum obtained by the electron beam irradiation had high background noise levels, which is attributed to the continuous X-rays produced by bremsshrahlung. On the other hand, by using the PIXE analysis technique, even the minor elements from the modern Sangkhalok could be detected. The detection limit of the PIXE technique was much lower than that obtained by the electron probe. This becomes the advantage of PIXE technique when it is applied to archaeological samples.

5.2 Suggestion and future studies

5.2.1 The effect of wall material on the beam transport should be examined in more detail by comparing the result obtained by scattering experiments with a glass (amorphous) target, a silicon crystal target, and other metallic targets. The wall material probably plays a much more important role in the beam transport of MeV ions in the tapered capillary having a minimum taper angle less than several milliradians.

5.2.3 To understand the scattering phenomenon of MeV protons in the flat glass target and the effect of surface roughness on the beam transport in greater detail, Monte Carlo simulations should be performed also for this experimental configuration.

5.2.4 Because the beam heat load on the capillary glass wall limits the allowable incident beam current, a method to cool the capillary glass should be developed. Moreover, a computer program that automatically controls sample position and data acquisition, and reconstructs the element map of the sample should be developed.

5.2.5 The absolute concentrations of the elements in the archaeological samples should be determined by using standard samples.

5.3 List of publications

5.3.1 Jaiyen, S., Chankow, N., Hasegawa, J., Oguri, Y. “Effect of wall material and shape on MeV ion focusing ability of tapered capillary optics” Nuclear Instruments and Methods in Physics Research B, Volume 271, October 2011, Pages 13-18.

5.3.2 Hasegawa, J., Jaiyen, S., Polee, C., Chankow, N., Oguri, Y. “Transport mechanism of MeV protons in tapered glass capillaries” Journal of Applied Physics, Volume 110, August 2011, Pages 044913-1-9.

5.3.3 Hasegawa, J., Jaiyen, S., Polee, C., Oguri, Y., “Development of a micro-PIXE system using tapered glass capillary optics” Nuclear Instruments and Methods in Physics Research B, Volume 269, April 2011, Pages 3087-3090.

5.4 List of presentations

5.4.1 Jaiyen, S., Hasegawa, J., Oguri, Y., Chankow, N., Wangchareontrakul, S. "Glass-capillary-based micro-PIXE analysis of old Thai pottery Sangkhalok" 2012 Annual Meeting of the Atomic Energy Society of Japan, P12, March 19 – 21, 2012, Fukui, Japan.

5.4.2 Hasegawa, J., Jaiyen, S., Oguri, Y, "Monte-Carlo Simulations of Ion Beam Focusing Using Glancing-Angle Scattering" 18th International Symposium on Heavy Ion Inertial Fusion (HIF2010), August 30 – September 3, 2010, Darmstadt, Germany.

5.4.3 Hasegawa, J., Jaiyen, S., Polee, C., Oguri, Y. "Development of a μ-PIXE System Using Tapered Glass Capillary Optics" 10th European Conference on Accelerators in applied Research and Technology (ECAART10), September 13–17, 2010, Athens, Greece.

5.4.4 Hasegawa, J., Jaiyen, S., Oguri, Y. "Dependence of Ion Transport through Glass Capillaries on Projectile and Target Atomic Numbers" The Spring Meeting of the Physical Society of Japan, 20aTC-7, March 20–23, 2010, Okayama, Japan.

5.4.5 Hasegawa, J., Jaiyen, S., Oguri, Y. "Quality Evaluation of Ion Beams Focused by Tapered Glass Capillaries" The Autumn Meeting of the Physical Society of Japan, 26aRH-10, September 23–26, 2010, Osaka, Japan.

REFERENCES

[1] Nebiki, T.,Yamamoto, T., Narusawa, T., Breese, M., B.H., Teo, E., J. and Watt, F. Focusing of MeV ion beam by means of tapered glass capillary optics. Journal of Vacuum Science and Technology A 21 (2003) : 1671-1674.

[2] Nebiki, T., Kabir, M., H. and Narusawa, T. In-air PIXE analysis by means of glass capillary optics. Nuclear Instruments and Methods in Physics Research B 249 (2006) : 226-229.

[3] Sekiba, D., et al. Development of micro-beam NRA for 3D-mapping of hydrogen distribution in solids: Application of tapered glass capillary to 6 MeV ^{15}N ion. Nuclear Instruments and Methods in Physics Research B 266 (2008) : 4027-4036.

[4] Hasegawa, J., Shiba, S., Fukuda, H. and Oguri, Y. A compact micro-beam system using a tapered glass capillary for proton-induced X-ray radiography. Nuclear Instruments and Methods in Physics Research B 266 (2008) : 2125-2129.

[5] Iwai, Y., et al. Ion irradiation in liquid of μm^3 region for cell surgery. Applied Physics Letters 92 (2008) : 023509-1-3.

[6] Fujita, N., Ishii, K. and Ogawa, H. Development of two-dimensional mapping technique by in-air-PIXE with metal capillary. Nuclear Instruments and Methods in Physics Research B 269 (2011) : 1023-1025.

[7] Ishii, K., Fujita, N. and Ogawa, H. Development of an in-air RBS technique using a metal capillary. Nuclear Instruments and Methods in Physics Research B 269 (2011) : 1026-1028.

[8] Simon, M., J., Döbeli, M., Müller, A., M. and Synal, H., -A. In-air STIM with a capillary microprobe. Nuclear Instruments and Methods in Physics Research B 273 (2001) : 237-240.

[9] Nebiki, T., et al. Taper angle dependence of the focusing effect of high energy heavy ion beams by glass capillaries. Nuclear Instruments and Methods in Physics Research B 266 (2008) : 1324-1327.

[10] Johansson, S., A.E., Campbell, J., L. and Malmqvist, K., G. Partical-Induced X-Ray Emission Spectrometry (PIXE). New York: John Wiley & Sons, 1995.

[11] Ishii, K., et al. Elemental analysis of cellular samples by in-air micro-PIXE. Nuclear Instruments and Methods in Physics Research B 181 (2001) : 448-453.

[12] Cvitanich, C., et al. Micro-PIXE investigation of bean seeds to assist micronutrient biofortification. Nuclear Instruments and Methods in Physics Research B 269 (2011) : 2297-2302.

[13] Kanngießer, B., et al. 3D Micro-PIXE at atmospheric pressure: A new tool for the investigation of art and archaeological objects. Nuclear Instruments and Methods in Physics Research B 264 (2007) : 383-388.

[14] Abdelouahed, H., B., et al. PIXE analysis of medieval silver coins. Materials Characterization 61 (2010) : 59-64.

[15] Zhang, B., et al. PIXE study on ancient pottery from Chinese Sanxia area. Nuclear Instruments and Methods in Physics Research B 219-220 (2004) : 26-29.

[16] Takai, M., Matsunaga, K., Inoue, K., Izumi, M., Gamo, K., Sato, M. and Namba, S. Microanalysis by focused MeV helium ion beam. Japanese Journal of Applied Physics 26 (1987) : L550-L553.

[17] Hellhammer, R., et al. Interaction of slow highly charged ion with the inner surface of nanocapillaries. Nuclear Instruments and Methods in Physics Research B 232 (2005) : 235-243.

[18] Ikeda, T., et al. Production of a microbeam of slow highly charged ion with a tapered glass capillary. Applied Physics Letters 89 (2006) : 163502-1-3.

[19] Gong, Z., Yan, S., Ma, H., Nie, R., Xue, J. and Wang, Y. Study of tapered glass capillary focusing MeV ion beam. Nuclear Instruments and Methods in Physics Research B 272 (2012) : 370-373.

[20] Kobayashi, T., Miyamoto, S., Ikeda, T., Kojima, T., M., Ogiwara, K. and Yamazaki, Y. Surface modification of polymers by ion irradiation at the solid-liquid interface. Nuclear Instruments and Methods in Physics Research B 272 (2012) : 405-408.

[21] Chu, W., Mayer, J., W. and Nicolet, M. Backscattering Spectrometry. New York: Academic press, 1978.

[22] Kojima, T., M., Tomono, D., Ikeda, T., Ishida, K., Iwai, Y., Iwasaki, M., Matsuda, Y., Matsuzaki, T. and Yamazaki, Y. Density enhancement of muon beams with tapered glass tubes. Journal of the Physical Society of Japan 76 (2007) : 093501-1-3.

[23] Schiessl, K., et al. Simulation of guiding of multiply charged projectiles through insulating capillaries. Physical Review A 72 (2005) : 062902-1-8.

[24] Hasegawa, J., Jaiyen, S., Polee, C., Chankow, N. and Oguri, Y. Transport mechanism of MeV protons in tapered glass capillaries. Journal of Applied Physics 110 (2011) : 044913-1-9.

[25] Low, C. Sawankoloke-Sukhothai Wares from the Empress Place Site, Singapore. The Heritage Journal 1 (2004) : 21-37.

[26] Ziegler, J., F. Computer Code SRIM-2010 [Online]. 2010. Available from : http://www.srim.org [2011, July 9]

Biography

Mr. Sarawut Jaiyen was born on April 9, 1977 at Lampang province. He graduated from Department of Physics, Faculty of Science, Srinakharinwirot University in 1999 with a Bachelor of Science degree in Physics. Later, he joined Department of Nuclear Engineering, Faculty of Engineering, Chulalongkorn University and received Master of Science degree in Nuclear Technology in 2002. He continued in the same department as an assistant researcher under the Applied Nuclear Technology in Industrial project for 1 year. In 2004, he started his work as a lecturer at Department of Physics, Faculty of Science and Technology, Rajamangala University of Technology Thanyaburi. In 2008, he was awarded a fellowship by the Office of the Higher Education Commission, Thailand under the program CHE Ph.D. Scholarship and he joined for a doctoral degree in nuclear engineering at Department of Nuclear Engineering, Chulalongkorn University. In 2009, he was awarded a fellowship by Ministry of Education, Science and Technology (MEXT), Government of Japan to research at Research Laboratory for Nuclear Reactors (RLNR), Tokyo Institute of Technology, Japan, for 1 year. In 2011, he continued his research for the doctoral degree in RLNR. He presented his research papers at the 2012 Annual Meeting of the Atomic Energy Society of Japan at Fukui, Japan in March 2012. These studies have resulted to three publications in Nuclear Instruments and Methods in Physics Research B and Journal of Applied Physics.